Quantum Reflection of Bose-Einstein Condensates

by

Thomas A. Pasquini

B.A. Physics
Dartmouth College, 2000

Submitted to the Department of Physics
in partial fulfillment of the requirements for the degree of

Doctor of Philosophy in Physics

at the

MASSACHUSETTS INSTITUTE OF TECHNOLOGY

SEPTEMBER 2007

Author . . . .
Department of Physics
August 21, 2007

Certified by . . . .
Wolfgang Ketterle
John D. MacAurthur Professor of Physics
Thesis Supervisor

Certified by . . . .
David E. Pritchard
Cecil and Ida Green Professor of Physics
Thesis Supervisor

Accepted by . . . .
Thomas J. Greytak
Professor of Physics, Associate Department Head for Education

Quantum Reflection of Bose-Einstein Condensates

by

Thomas A. Pasquini

Submitted to the Department of Physics
on August 21, 2007, in partial fulfillment of the
requirements for the degree of
Doctor of Philosophy in Physics

Abstract

Recent developments in atom optics have brought Bose-Einstein condensates within 1 μm of solid surfaces where the atom-surface interactions can no longer be ignored. At long-range, the atom-surface interaction is described by the weakly attractive Casimir-Polder potential which is classically predicted to accelerate an incident atom toward the surface where it will interact strongly with the internal modes of the surface, lose energy, and land in a bound state of the surface. When the incident atom is very cold, on the order of a few nanokelvin, however, the acceleration of the atomic wavefunction is so abrupt that the atom may partially reflect from the attractive tail in a process known as quantum reflection.

This work presents experimental evidence for quantum reflection from a solid surface at normal incidence. Using atoms from a ^{23}Na BEC, cooled to a few nanokelvin in a recently demonstrated single-coil trap, controlled collisions were induced between atoms and solid silicon surface. A maximum reflection probability of $\sim 12\%$ was observed for an incident velocity of 1 mm/s. Atoms confined against the surface at low density exhibited an enhanced lifetime due to quantum reflection.

A surprising aspect of quantum reflection is that nano-structured surfaces are predicted to exhibit enhanced quantum reflection due to the reduction of the atom-surface interaction from reduced density surfaces. Using a pillared surface with an density reduced to 1% of bulk density, we observe an enhancement of the reflection probability to $\sim 60\%$.

At velocities from 2-25 mm/s, predicted threshold dependence of the reflection probability was observed. At velocities below 2 mm/s, the reflection probability was observed to saturate. We develop a simple model which predicts the saturation as a result of mean-field interactions between atoms in the incident Bose-Einstein condensate.

Thesis Supervisor: Wolfgang Ketterle
Title: John D. MacAurthur Professor of Physics

Thesis Supervisor: David E. Pritchard
Title: Cecil and Ida Green Professor of Physics

For the parents in my life,
Sharon and Tom,
Ann and Monty,
and Elisabeth.

Acknowledgments

In 2002, I searched for a graduate research advisor who was excited about the "tabletop" research they were doing and who smiled in their photographs. With Dave and Wolfgang, I found excitement and smiles twice over. I thank them for the opportunity to explore and experiment in their lab for the last five years and for their support and encouragement throughout my time at MIT.

Help exploring was never in short supply in the Science Chamber, and I have benefitted from group members who have moved on and those who will remain. My work here has been eased along by patience and understanding of graduate students Aaron and Yong, who nurtured my development on the apparatus, driven forward by the insights of post-docs Dave and Michele, and "boosted" by diploma students Andre, Christian, and Sebastian. Visitors to the group Won-Ho and Carsten have also contributed to the lab. Thank you for paving the way for this work. In recent years, we have all benefited greatly from the quiet diligence of Gyu-Boong, the gung-ho attitude of Caleb, the probing questions of Tony and the exuberance of Ye-Ryoung and Jae. Thank you for making the last years so productive and good luck in the years to come.

The work of the Science Chamber is not limited to the members of BEC III. Up and down the building 26 hallway, collaborators in the Ketterle/Pritchard group and the Vuletic group too numerous to thank by name have left their mark on the experiments of the last 5 years. More recently, members of BEC I and BEC II, particularly Christian, Andre, Yong, Dan, and Jit Kee, have provided guidance and expertise in the rebuilding the Science Chamber to work with fermionic lithium. Beyond the halls of MIT, I have benefitted from discussions with Jim Babb and Robin Scott whose understanding of atom-surface potentials and BEC interactions have helped to grow and shape my own.

Five years at MIT has shown me that even a competitive atmosphere can give rise to great friendships. I was fortunate, in my first years at MIT, to work with Jamil, Kendra, Julia, and Cort (and so many others) in an effort to secure health care funding for graduate students. That year I also fell in with Molly and Tim and Will and Sarah Jane who have remained close to my family throughout our time in Boston. Within the lab, there are too many friends to recognize individually. Four colleagues in particular, have been support in times of stress and joyful in times of success; thank you Micah, Gretchen, Jit Kee, and Dan for your friendship. Finally, the families at Westgate have made the last 6 months very special for my growing family; you are one of the greatest parts of MIT.

Parents, to whom I have dedicated this work, have supported and encouraged me as I worked toward this degree. Tom and Sharon, my parents, believed in me and pushed me to do my best work throughout graduate school; thank you for your unswerving faith in me. Monty and Ann, my parents-in-law, are my family in Boston and have always opened their

home to me, particularly following the birth of my children; thank you for all your support. Most importantly, my wife Elisabeth, now a parent herself, has carried me through the many challenges of MIT. I owe her so much, and I hope that the journey we begin now is the right path for our family.

Contents

List of Figures

List of Tables

Chapter 1

Introduction: Nanokelvin Atoms and Surfaces

In the early 1800's, Cambridge, through the entrepreneurship of William and Frederic Tudor, became a major center for cold atom technology [188]. Although mechanical refrigeration techniques involving vapor compression and expansion were being developed at the time, the dominant source of "cooling" was an environmental reservoir, specifically the frozen layers atop small, bodies of fresh water like Fresh Pond and Walden Pond. Blocks of ice from these ponds were harvested in the winter, stored, and shipped as far as India as the ice trade flourished in the century or so following its inception. Today, Cambridge continues as a center for low temperature science and technology. The Center for Ultracold Atoms at MIT and Harvard boasts one of the largest consortiums of scientists working at temperatures below 1 μK, a regime non-existent in nature. While no new economy has yet sprung up around ultracold atoms, the techniques developed here are part of a rapidly expanding field that promises to revolutionize precision measurements [82], offer new insight into condensed matter systems [61, 196], realize new materials [4, 102] and allow the processing and storage of quantum information [17].

The scientific community's fascination with low temperatures stems from a desire to see what lies beyond the limits of ordinary human experience. There are phenomena, like Bose-Einstein condensation, that could never be observed without years of pre-planning and sophisticated apparatus [88, 32]. There is also simplicity in the well controlled, isolated system; the physics uncovered at low temperatures is ubiquitous, but obscured by the relatively high temperatures encountered daily. Moving to the bottom of the energy scale allows scientists to understand natural phenomena from the ground up rather than attempt to de convolve the myriad factors which underlie them.

The main experimental achievement of this thesis, quantum reflection, involves the question of what happens when atoms strike a solid surface. Will the collision be elastic
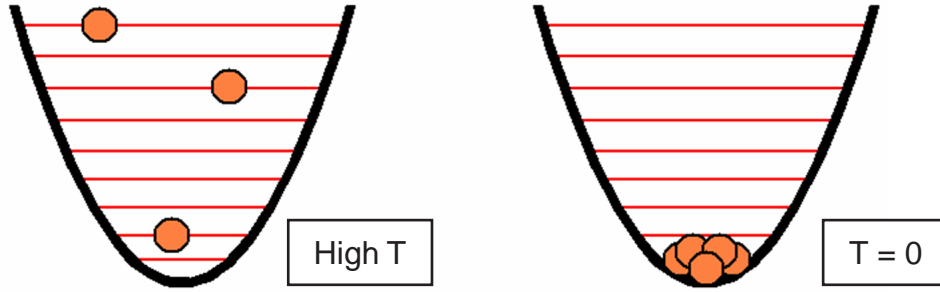
Figure 1-1: At high temperatures, atoms sparsely occupy the energy levels of a system, as shown in the left panel. In the zero temperature limit (right panel), bosonic atoms "pile up" in the ground state of the systems forming a Bose-Einstein condensate.

or inelastic? Will the atom reflect from the surface at all, or will it stick? The wonder of working with ultracold atoms is that even mundane questions such as these can have surprising answers that help us to understand the world around us.

This Chapter motivates the work of the thesis and provides some background in the physics of Bose-Einstein condensates and surface potentials.

1.1 Phase transitions for dilute gases

A Bose-Einstein condensate (BEC) is the macroscopic occupation of the ground state of a system. A fair understanding of BEC is reached through a simplified 1D system: a harmonic oscillator potential with frequency ω containing N non-interacting, identical bosons and comprising an infinite number of evenly spaced energy levels $E_j = j\hbar\omega$. At a temperature T, energy levels with $E_j \leq k_B T$, where k_B is the Boltzmann constant, are classically accessible to each of the bosons. At high T, $k_B T/\hbar\omega \gg N$, and the probability of any one state being occupied is small. But as T is reduced, the bosons are restricted to fewer energy levels. When the number of accessible levels is less than N, the occupation of the ground state becomes larger than unity and the bosons in this ground state are referred to as the Bose-Einstein condensate.

A model 3D harmonic oscillator potential and rigorous accounting for the occupation of energy levels gives a transition temperature, T_c, for the onset of BEC as

$$k_B T_c = \hbar\bar{\omega}\left(\frac{N}{\zeta(3)}\right)^{1/3} \tag{1.1}$$

where $\zeta(3) \approx 1.202$ and $\bar{\omega} = (\omega_x \omega_y \omega_z)^{1/3}$ is the geometric mean of the trap frequencies. In our magnetic trap (discussed in Section 2.1.4), $\bar{\omega} \sim 2\pi \times 100$ Hz and $N \sim 10^7$, giving

$T_c \sim 1$ μK. The peak density of atoms is typically 10^{15} cm^{-3}, far below the density of air ($n \sim 10^{20}$ cm^3). This low density is extremely important: higher densities would give significantly higher transition temperatures, but the 3-body collision rates which allow molecules to form would lead to significant trap loss, preventing the BEC transition.

Even at the low densities in our traps, the long-range atom-atom interactions play a significant role in condensate behavior, e.g. collisions are responsible for the re-thermalization of the cloud during evaporative cooling. Interactions are accounted for by including a term in the Schrödinger equation characterizing an atom's interaction with all other atoms in the trap. In the simplest case, only the lowest energy, s-wave collisions are considered by including a potential $V(\mathbf{r}) = 4\pi\hbar^2 a/m \times n(\mathbf{r})$, where the parameter $a = 2.75$ nm is the scattering length and $n(\mathbf{r})$ is the local density. This introduces a density dependent term into the Hamiltonian and generates the Gross-Pitaevskii equation (GPE) [63, 138]

$$\left(-\frac{\hbar^2}{2m}\nabla^2 + V_{\text{trap}}(\mathbf{r}) + \frac{4\pi\hbar^2 a}{m}n(\mathbf{r}) \right) \psi(\mathbf{r}) = \mu\psi(\mathbf{r}) \tag{1.2}$$

where V_{trap} is the external potential and μ is the chemical potential which generates the temporal evolution of the condensate wavefunction $\Psi(\mathbf{r}, t) = \psi(\mathbf{r})e^{-i(\mu/\hbar)t}$. The density dependent term, while small, will dominate the kinetic contribution to the total energy when $E_{\text{interaction}} \propto 4\pi\hbar^2 a/m \times N \times N/l_{\text{ho}}^3 > E_{\text{kinetic}} \propto N\hbar\bar{\omega}$ where $l_{\text{ho}} = \sqrt{\hbar/m\bar{\omega}}$ is the trap length. This is the Thomas-Fermi limit in which most of our experiments are performed [35, 136].

The most prominent effect of the inclusion of this atom-atom interaction energy is the spatial expansion of the ground state wave function with increasing condensate number. In the absence of interactions, condensing atoms which "pile up" in the ground state are all energetically confined to the same limited region of space near the trap center and the size of the condensate is independent of the number of atoms. With atom-atom interactions, however, the size of the condensate grows with N as the collisions between atoms act to "push" the atoms up the sides of the trap. In the Thomas-Fermi limit, the spatial derivative term is dropped from the GPE resulting in definitions for the chemical potential and condensate radius, R_{TF}:

$$\mu = \frac{1}{2}\hbar\bar{\omega} \left(15N\frac{a}{l_{\text{ho}}} \right)^{2/5} \tag{1.3}$$

$$R_{\text{TF},i} = \left(\frac{2\mu}{m\omega_i^2} \right)^{1/2} \tag{1.4}$$

for atoms in a 3D harmonic trap.

For a full, easy-to-read treatment of fundamental condensate physics, I recommend the review paper by Pitaevskii and Stringari [35] or the book by Pethick and Smith [136].
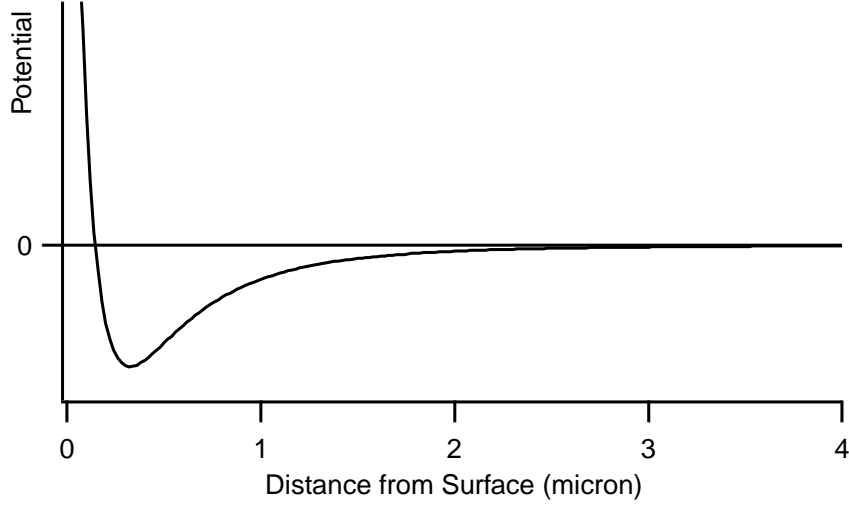
Figure 1-2: The atom-surface interaction is short range repulsive and long range attractive. In general, the potential minimum supports many bound atomic states.

1.2 Atoms near surfaces

The interaction between atoms and surfaces is typically long-range attractive and short-range repulsive, as sketched in Figure 1-2. The repulsive interaction is Coulomb repulsion that onsets when the electron clouds of the incident atom begin to overlap with those of the surface. The long-range attractive interaction, known in various regimes as the London-van der Waals [106], Casimir-Polder [23], of Lifshitz force [103, 117] originates in the fluctuating dipole moment of atoms and is a theoretical challenge that, even today, attracts continued study [6]. Part of what makes the interaction so intriguing is that, classically, it shouldn't exist at all; the energy needed to create an atomic dipole moment exceeds the energy that can be gained from the interactions of that dipole moment with another atom or a surface. Only when the atom is considered quantum mechanically do fluctuations in the atomic ground state necessitate a fluctuating dipole moment and insure that atoms interact at great distances [174].

The atom-surface interaction is mediated by the electromagnetic field. Accounting for the various frequency dependencies of atoms and surfaces, correlations between the atoms and surfaces, and the quantum and thermal fluctuations of the electromagnetic field is difficult, and the general theory developed by Lifshitz leads to expressions like

$$
\begin{aligned}
V_{\text{surf}}(d) &= -\frac{k_B T \alpha_0}{4d^3} \frac{(\varepsilon_0 - 1)}{(\varepsilon_0 + 1)} - \frac{KT}{c^3} \sum_{n=1}^{\infty} \alpha \xi_n^3 \\
&\times \int_1^{\infty} \exp\left(-\frac{2p\xi_n d}{c}\right) \left[\frac{(\sqrt{\varepsilon_1 - 1 + p^2} - p)}{(\sqrt{\varepsilon_1 - 1 + p^2} + p)}\right.
\end{aligned}
\tag{1.5}
$$

20

$$+ (1 - 2p^2)\frac{(\sqrt{\varepsilon_1 - 1 + p^2} - p\varepsilon)}{(\sqrt{\varepsilon_1 - 1 + p^2} + p\varepsilon)}\bigg]\bigg) dp$$

Fortunately, these expressions simplify to more wieldy expressions, like $V_{\text{C}-\text{P}}(d) = C_4/d^4$, as long as we are only concerned with interactions on a particular length scale. Here, the C_4 coefficient encompasses all of the relevant information about the surface in question and certain assumptions have been made about the atomic structure. *Ab initio* calculations of the C_4 coefficient are difficult, requiring precise knowledge of the frequency dependent terms in the atomic polarizability and the dielectric function of the wall, but have been done for many alkali species on a range of conducting and dielectric surfaces [175, 192, 91, 112, 38, 111, 55].

There is a more illuminating, if less rigorous, path to understanding atom-surface interactions. The system of choice for an atomic physicist is the isolated atom; the isolated alkali atom is ideal for its simple optical structure, dominated by the behavior of the valence electron. The presence of other atoms is accounted for as a perturbation to the single-atom picture, as was done above in Section 1.1. Atom-atom interactions are also responsible for the atom-surface interactions when the surface is understood to be a high-density collection of atoms: intuitively, any surface can be broken down into its constituent atoms which interact with the atom in free space. These interactions are summed to give the atom surface interaction [118]. This treatment, best detailed in Ref. [174], is complimentary to the rigorous quantum electrodynamical treatment of Refs. [103, 138, 117].

1.2.1 The atom-atom interaction

Electromagnetic forces dominate the inter-atomic and intra-atomic interactions. At short ranges, on the order of the Bohr radius a_0, as in solids or molecules, the response of the electron wavefunction to the nuclear Coulomb potential determines the behavior of the composite material [9]. At large distances and low energies, as in Bose condensed atomic gases, the pure Coulombic potential ($\propto 1/r$) is absent; neutral atoms have no net charge and, to first order, we expect no interaction when the distances separating the atoms becomes large relative to a_0. For neutral atoms, the dominant term in the electric field is the dipole term:

$$E(\mathbf{r}) = \frac{1}{4\pi\varepsilon_0}\frac{(3\mathbf{p}\cdot\hat{r})\hat{r} - \mathbf{p}}{|\mathbf{r}|^3} \tag{1.6}$$

where $\mathbf{p}$ is the dipole moment of the atom.

For two isolated dipole moments, there is an energy associated with the relative orientation of the dipoles, specifically, $V_{\text{dipole}-\text{dipole}}(r) = (1/4\pi\varepsilon_0)(\mathbf{p}_1\mathbf{p}_2 - 3(\mathbf{p}_1\cdot\hat{r}(\mathbf{p}_2\cdot\hat{r}))/r^3$. It is worth noting that atoms do not have permanent electric dipole moments, that is, $\langle\mathbf{p}\rangle = 0$. Eigenstates of the atomic Hamiltonian are also eigenstates of the parity operator [31]. Some
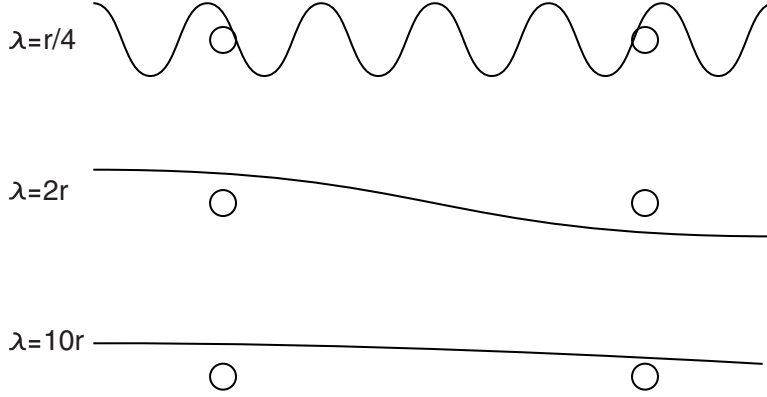
Figure 1-3: For EM modes with $\lambda = c/\omega$ much smaller than the separation of two atoms, we expect that the driven-dipole fluctuations will be uncorrelated, except in the particular case when only one mode of the field is occupied, as in a laser field. For EM modes with λ larger than the separation of two atoms, however, the field does not change appreciably between the two atoms, and the fluctuations will be strongly correlated. These correlations survive time averaging, and so we expect an interaction between fluctuating neutral atoms as a result.

perturbation, typically in the form of an electric field, must be present to mix states of definite parity, allowing the dipole operator, $\mathbf{p} = e\mathbf{z}$, which is parity odd, to take a non-zero value[1]. Therefore, while the average interaction between two atoms is zero, in the presence of fluctuations, there may be higher order terms that survive the temporal averaging.

Fluctuations of the electromagnetic field, either due to the zero-point energy of the vacuum or to thermal fluctuations, play a critical role in the interactions of neutral atoms; any occupied mode of the electromagnetic field will drive dipole fluctuations in atoms. The magnitude of the potential experienced by dipole $\mathbf{p}_1$ due to the field of fluctuating dipole $\mathbf{p}_2$ can be approximated as

$$V(\mathbf{x}_1, \mathbf{x}_2, t) = \int_0^\infty \mathbf{p}_1(\omega, t)\mathbf{E}_{2\to 1}(\omega, t)N(\omega)d\omega \tag{1.7}$$

where $\mathbf{E}_{2\to 1}$ is the field of dipole $\mathbf{p}_2$ at $\mathbf{x}_1$ and $N(\omega)$ is the density of modes of the electromagnetic field as a function of frequency, ω. Not all modes of the fluctuating field are relevant to this integral, as discussed in Figure 1-3. Specifically, only modes with wavelength $\lambda = c/\omega > \mathbf{x}_2 - \mathbf{x}_1$ will contribute to the integral because the electric field is nearly the same at $\mathbf{x}_1$ and $\mathbf{x}_2$. Since shorter wavelengths interfere destructively, the integral can be effectively cut off at $\omega = c/r$.

The response of a neutral atom to an oscillating electric field is, approximately, for the

---

[1]There may be states of opposite parity that are degenerate or very nearly degenerate, as in the $2s$ and one of the $2p$ states of hydrogen. This degeneracy is only broken as result of zero-point fluctuations of the electromagnetic field which give rise to the Lamb shift.

center of the electron wavefunction to be displaced slightly from the nucleus. As long as the fields are not too strong, the electron can be likened to a mass on a spring; the induced dipole moment is proportional to the applied electric field $\mathbf{p} = \alpha(\omega)\mathbf{E}$. The polarizability, $\alpha(\omega)$, characterizes the response of an atom with ground state $|g\rangle$ and excited states $|k\rangle$ and to an applied electromagnetic field at frequency ω, such that:

$$\alpha(\omega) = \frac{2e^2}{\hbar} \sum_k \frac{\omega_{kg}|\langle k|z|g\rangle|^2}{\omega_{kg}^2 - \omega^2} \tag{1.8}$$

where $E_k - E_g = \hbar\omega_{kg}$ is the energy difference between the various excited states. For an atom with a dominant transition ω_0, this expression simplifies to:

$$\alpha(\omega) = \frac{e^2}{m} \frac{1}{\omega_0^2 - \omega^2} \tag{1.9}$$

where we have made use of the Thomas-Reiche-Kuhn summation rule to set the oscillator strength for transition ω_0 equal to 1. Obviously, this result breaks down very close to resonance as we have ignored radiative damping in our treatment of the atomic oscillator.

At large distances, the radiation field of a driven dipole moment $\mathbf{p}_2$ goes, approximately as $\mathbf{E}_{2\to1} = \ddot{\mathbf{p}}_2/c^2 r = \alpha(\omega)\mathbf{E}(\mathbf{x}_2)\omega^2/c^2 r$. Since the time averaged field at $\mathbf{x}_2$ is the same as at $\mathbf{x}_1$, Equation 1.7 simplifies to

$$V(\mathbf{x}_1, \mathbf{x}_2) = \int_0^{c/r} \alpha_1(\omega)\alpha_2(\omega)|\mathbf{E}(\omega)|^2 \frac{\omega^4}{c^5 r} d\omega \tag{1.10}$$

where the usual substitution $N(\omega) = \omega^2/c^3$ has been made.

We are now in a position to evaluate Equation 1.10. There are three relevant limits that emerge[2].

Casimir-Polder limit: $r \gg c/\omega_0$

At large distances, that is for separations larger than the transition wavelength of the atoms, the relevant modes of the fluctuating field are low frequency. At low frequency, the frequency dependence of the atomic polarizability is trivial, simplifying the treatment. A substitution of $|\mathbf{E}(\omega)|^2 = \hbar\omega$ to account for the vacuum fluctuations of the electric field gives, finally, $V_{\text{atom}-\text{atom}}(r) = \hbar\, c\alpha_1\alpha_2/r^7$. This expression is the famous Casimir retarded potential for atom-atom interactions. The term "retarded" refers to the fact that a radiative field couples the atoms and the finite speed of light becomes relevant. In the van der Waals limit discussed below, the correlations between atoms exists in the near field of the atomic dipole and the speed of light can be safely ignored. The dependence on $\hbar$ shows that the

---

[2]We restrict the following discussion to the interaction between two identical atoms for simplicity.

long-range atom-atom interaction is a purely quantum effect.

Lifshitz limit: $r \gg c/\omega_0$ **and** $r > \lambda_T$

At large distances and finite temperatures, the zero-point fluctuations can be dominated by the background of thermal photons. The energy in a particular mode of the electromagnetic field due to zero point fluctuations is $E_{\text{zeropoint}} = \frac{1}{2}\hbar\omega_0$, whereas the energy in that mode due to thermal fluctuations is

$$E_{\text{thermal}} = \frac{\hbar\omega_0}{e^{\frac{\hbar\omega_0}{k_b T}} - 1} \tag{1.11}$$

For small ω_0, $E_{\text{zeropoint}}$ approaches zero while $E_{\text{thermal}} \approx k_B T$, so thermal fluctuations dominate for wavelengths larger than the thermal wavelength, $\lambda_T = \hbar c/k_B T$.

Using the earlier expression for the classical potential, Equation 1.7, but substituting the thermal mode energy removes an $\hbar c/r$ and replaces it with a $k_B T$, giving $V_{\text{atom}-\text{atom}}(r) = \alpha_1 \alpha_2 k_B T/r^6$. The disappearance of the $\hbar$ from this expression shows that the quantum fluctuations of the vacuum are no longer responsible for the atom-atom interaction at very long range.

van der Waals limit: $r \ll c/\omega_0$

In the limit that the atoms are spaced more closely than the wavelength associated with the dominant electronic transition, we cannot make the simplifying assumption that the atomic polarizability remains constant and, additionally, the near field of the dipole becomes dominant. Instead, we must approach the problem from perturbation theory. At second order, a non-zero atom-atom potential potential emerge, $V_{\text{atom}-\text{atom}}(r) = [V_{\text{dipole}-\text{dipole}}(r)]^2/(E_e - E_g)$, where $(E_e - E_g)$ gives the characteristic excitation energy of the system, typically on the order of e^2/a_0 when the dipole moments are of order ea_0, where e is the electron charge and a_0 is the Bohr radius. This expression gives $V_{\text{atom}-\text{atom}}(r) = -\hbar\omega_0(a_0/r)^6$, which shows the typical r^{-6} dependence associated with the van der Waals interaction.

1.2.2 The atom-surface interaction

A simple way to extend atom-atom interactions to atom-surface interactions is to integrate over the many atoms that make up a surface. An integration over the volume shows that the atom-surface interaction will necessarily depend on the density of the surface. The atom-surface separation determines which limit of the atom-atom interactions will dominate. In other words, the bulk of the atom-surface interaction for a separation r derives from the atoms in the layer of thickness r near the surface. For the three relevant limits above, the
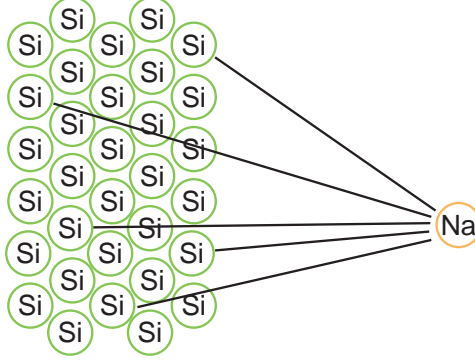
Figure 1-4: Cartoon explanation of atom-surface interactions. The individual atom-atom interactions between the incident atom and the constituent atoms of the surface gives rise to the atom-surface potential.

expressions for the atom-surface potential can be written as

$$V_{\text{Casimir}-\text{Polder}} = -\frac{C_4(\rho)}{r^4} \tag{1.12}$$

$$V_{\text{Lifshitz}} = -\frac{C_L(\rho)T}{r^3} \tag{1.13}$$

$$V_{\text{van der Waals}} = -\frac{C_3(\rho)}{r^3} \tag{1.14}$$

This approach, while intuitive, ignores the structure of the surface and the generally complex frequency dependencies that arise when atoms are spaced at distances comparable to a_0, and should not be used to derive a value for C_3 or C_4.

Effect of non-equilibrium temperatures

Concurrent to the quantum reflection work presented in this thesis, theoretical work by Stringari's group [119, 11, 6, 7, 5, 139] and experimental work by Cornell's group [70, 127, 128] has addressed direct measurement of the atom-surface force in the regime where thermal fluctuations become relevant. While the dominant contribution of thermal radiation to the atom-surface potential has been well understood since Lifshitz [103, 138, 117], there had been no measurements of such forces and the non-equilibrium system had not been considered. When the surface temperature T_{surf} differs from the temperature of the vacuum between the atom and the surface T_{vac}, the potential takes the form $V_{\text{non}-\text{eq}} = -(C_2/r^2)(T_{\text{surf}}^2 - T_{\text{vac}}^2)$ [7].

1.3 BEC III research

Over the past 5 years, research efforts in my research group, BEC III, have been directed toward understanding condensates in double-well potentials and the interaction between atoms and surfaces. Following the construction of the Science Chamber and initial transfer of atoms [64], the first atom chip installed in the science chamber revealed that wire imperfections posed serious challenges for working with atoms near surfaces [100]. Some creative thinking from Aaron Leanhardt, then a senior graduate student, led to the very successful optical double well trap used by Yong-Il Shin to first demonstrate phase coherent splitting of BEC [169] and to study the formation of condensates out of cold thermal clouds [170, 157]. The introduction by Michele Saba of Bragg scattering to couple atoms from one well to another replaced the matter wave interference readout of the phase [3] with the continuous monitoring of the relative phase of the two BECs with either an atomic or optical signal [148] and created a novel geometry where the two condensates were weakly coupled in a controllable fashion [168].

Parallel to the work on atoms in double well geometries, a second effort was directed toward quantum reflection of BEC at normal incidence from solid surfaces [133, 151] and the improvement of quantum reflection by tailoring the atom surface potential [132].

Perseverance with the challenges of atom chips led to a better understanding of the sensitivity our continuous deformation splitting scheme to technical noise [171] and led to the adoption of a more successful method pioneered by the Schmiedmayer group in Heidelberg [158]. In the past year, our rf splitting atom chip has, under the adept hand of Gyu-boong Jo, produced number squeezed splitting and record setting coherence times [82] and allowed studies of the recombination of condensates in trap [81] and the influence of phase fluctuations on condensate coherence [80].

This thesis will focus on the atom-surface interaction work because I was more deeply involved with that work. For a detailed review of our group's early work on condensates in double-well geometries, please refer to the theses of Aaron Leanhardt [98] and Yong-Il Shin [172].

1.4 Outline of thesis

Chapter 2 introduces the experimental apparatus that was nearing completion as I joined the group in 2002 and provides an overview of the experimental techniques for working with nanokelvin atoms. The Chapter also focuses on the single coil trap geometry used in the quantum reflection experiments. Chapter 3 lays the theoretical groundwork for the quantum reflection studied in this thesis. Chapter 4 reviews the current state of quantum reflection research and describes the first experimental effort on quantum reflection within

the Ketterle group. Chapter 5 describes our work at improving the reflection probability by reducing the density of the reflecting surface. Our group's contribution to the current theoretical model of BEC quantum reflection is described in Chapter 6.

The final year of my thesis research has been dedicated to a major extension of the experimental apparatus to produce degenerate Fermi gases of sympathetically cooled ^{6}Li. Section 2.3 describes some aspects of the upgrade.

Chapter 2

The Science Chamber Apparatus

The experimental apparatus used for all of the experiments in this thesis came online in 2001 as a third generation machine in the Ketterle/Pritchard group, intended to allow for easy manipulation of sodium Bose Einstein condensates (BEC). Following the naming traditions of the lab, the machine was given a name describing its major feature (the Science Chamber) and the group who constructed and maintained it a serial name (BEC III). In the Science Chamber, BEC is transported with optical tweezers from the production chamber into the auxiliary "science" chamber, an independent vacuum chamber with improved optical access. Once in the science chamber, condensates are loaded into magnetic and optical micro-traps for study. The science chamber affords flexibility in experimental design and rapid cycling of experiments without compromising the ultrahigh vacuum required for condensate production. Research in the science chamber is focused on the manipulation of condensates, novel trapping geometries, and atom interferometry [25, 98, 157, 151, 172].

An extensive description of the construction and design of the Science Chamber can be found in Ananth Chikkatur's thesis [25]. Most aspects of the machine were modeled on the successful BEC I and BEC II machines, so the thesis work of Dan Stamper-Kurn [176] and others are also relevant.

This chapter will present an overview and details of the most relevant aspects of the apparatus.

2.1 Apparatus overview

The science chamber apparatus was designed as a condensate beamline which would separate the *production* of BEC from the *experiments* performed with BEC. All of the techniques in the following discussion are used in the experiments we publish, they are typically summarized by a single line: "Bose-Einstein condensates containing more than 10^7 ^{23}Na atoms were created in the weak field seeking $|F = 1, m_F = -1\rangle$ state in a magnetic trap, captured
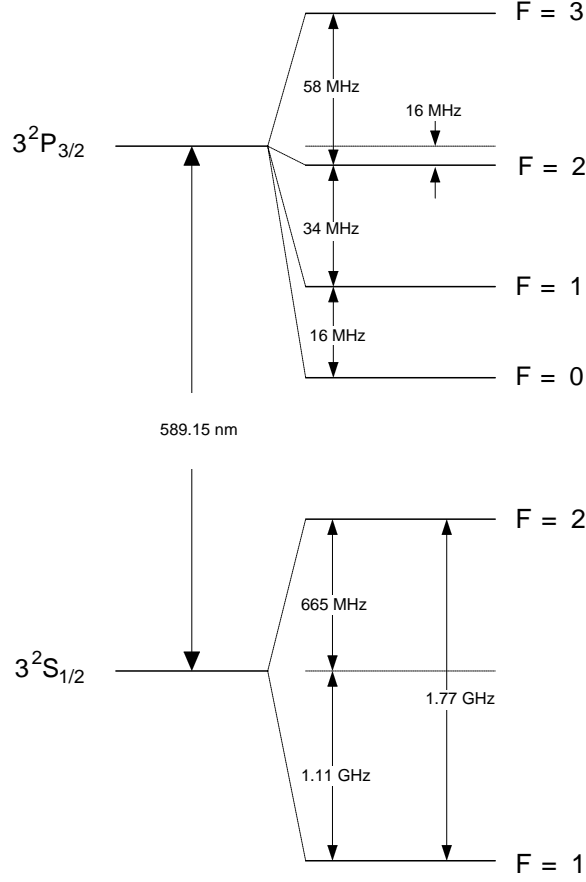
Figure 2-1: ^{23}Na D2 line structure, adapted from Ref [180]. MOT trapping light is near resonant with the $F = 2 \rightarrow F' = 3$ cycling transition, repumping light is near resonant with the $F = 1 \rightarrow F' = 2$ transition, and slowing light is 1GHz detuned from the $F = 2 \rightarrow F' = 3$ transition. Trapped atoms are typically in the ground ($F = 1$) state, and are imaged with light near the repumping frequency or optically pumped into the $F = 2$ state with repumping light then imaged with light near the MOT frequency.

in the focus of an optical tweezers laser beam and transferred into and auxiliary "science" chamber as described in [64]." This section presents a less streamlined overview of the experiment, as might be given to an undergraduate interested in working on the experiment. The presentation is intended to supplement a technical description of the machine [182, 25] by giving the reader an appreciation for the various systems that must be maintained in order to work with BEC.

2.1.1 ^{23}Na

In the Science Chamber, we work with ^{23}Na, an alkali metal total nuclear spin $I = 3/2$ and a single, ground-state valence electron in the $3S$ orbital ($S = 1/2, L = 0$). The first excited

30

Atomic Mass	22.989 u= 3.818×10^{-26} kg
Melting Point	$97.8°$C
Ground State Magnetic Moment	$\mu_B/2 = 463.70$ J/T=0.7MHz/G
Natural Line Width	$2\pi \times 9.795$ MHz
Recoil Velocity	2.9461 cm/s
Saturation Intensity	6.40 mW/cm^2
Scattering Length	2.75 nm

Table 2.1: Sodium data collected from Ref. [180].

state sees the promotion of this electron to the $3P$ orbital ($S = 1/2, L = 1$), resulting in the fine structure doublet. Of these, the $D2$ transition from the $3^2S_{1/2}$ state to the $3^2P_{3/2}$ state is the one used for trapping and cooling. The relevant optical structure is shown in Figure 2-1. A few relevant physical properties are collected in Table 2.1.

2.1.2 Vacuum system

The vacuum system for the BEC III lab was designed with four main sections, visible in the photo of Figure 2-2. The "main" chamber, where BECs are created, was designed to accommodate the magnetic field coils and half-dozen optical axes necessary for cooling and trapping. Slowed atoms are introduced to the main chamber via the multi-species oven [178] and the Zeeman slower, a ~ 2 m long tube connecting the oven to the main chamber. These three sections comprise the heart of any large number BEC apparatus [182]. The science chamber, is connected to the main chamber by a pneumatic gate valve. When closed off, the science chamber can be vented to atmospheric pressure and reconfigured to introduce new experiments. When opened, the gate valve allows for condensed atoms to be transported via an optical dipole trap (ODT) from the main chamber to the science chamber. Since the original construction, described in Reference [25], the science chamber has been replaced with a larger volume chamber as described in Reference [172].

Bose-Einstein condensates exist at temperatures roughly a billionth of room temperature; nitrogen and oxygen molecules travel at speeds of $\sim$300 m/s at room temperature while the atoms in a BEC travel at a few cm/s. Interactions between BEC and room temperature gases must be avoided. All of our experiments are performed at "ultra-high" vacuum (UHV) in an evacuated stainless steel vacuum chamber maintained at a nominal pressure of 10^{-11} Torr, as opposed to atmospheric pressure of 760 Torr. The density of "air" in the vacuum chamber is roughly 10^{-14} times the density of air at sea level; instead of a number density of 2.6×10^{19} atoms/cm^3 for air at standard pressure, inside the vacuum chamber, the number density is roughly 3×10^5 atoms/cm^3. There are no more than a few billion room temperature air molecules inside the entire apparatus.
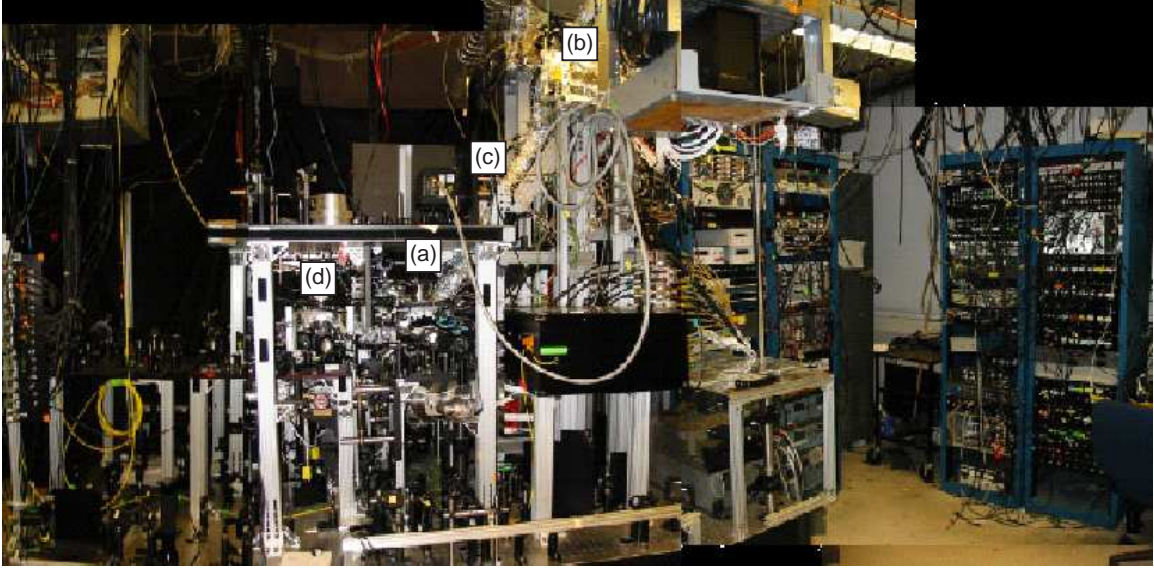
Figure 2-2: The Science Chamber as in 2007. There are four main vacuum sections: (a) the main chamber for BEC production, (b) the multi-species oven for generating flux of ^{23}Na and ^{6}Li, (c) the slower for slowing the atomic beams, and (d) the science chamber for rapid cycling of experiments.

At such low pressures, the desorption of gases from surfaces becomes substantial, gradually destroying the UHV environment. The vacuum is maintained from day-to-day by several ion pumps and titanium sublimation pumps [129, 65]. In the event that any part of the system is exposed to air at atmospheric pressure, for example to refresh the atomic source or reconfigure the science chamber, the vacuum is re-established with a turbo pump. After brief, controlled exposure to an inert gas, like argon, vacuum can be re-established within a day. For extended exposure to oxygen and water vapor, the surfaces of the vacuum chamber typically need to be heated to 120° C with the turbo pump running for one or more days to allow these gasses to desorb from the surfaces completely. Extensive descriptions of the baking procedures used by the lab to prepare the system for 10^{-11} Torr can be found in Reference [25].

2.1.3 Cooling atoms

Sodium and, recently, lithium atoms are introduced to the vacuum via an atomic beam originating in the oven. A gas of the desired atom is produced by heating a solid sample in the oven. A small hole in the oven, the nozzle, allows this gas to stream out of the oven and into the Zeeman slower. Along the path to the main chamber, a series of apertures ensure that only atoms traveling directly along the line connecting the oven to the center of the vacuum chamber enter the ultra-high vacuum region.
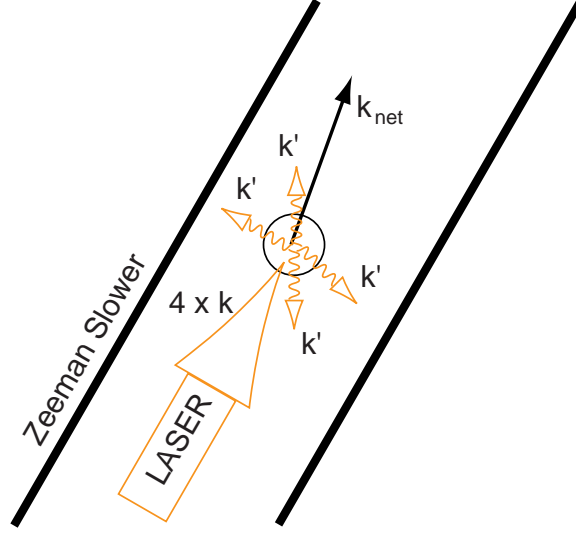
Figure 2-3: Slowing of the atomic beam. When an atom traveling down the Zeeman slower scatters a photon, it receives a "kick" of momentum $\hbar\mathbf{k}$ opposite the direction of motion. It may spontaneously re-emit this photon into a randomly directed the mode $\mathbf{k}'$, where $|\mathbf{k}| = |\mathbf{k}'|$. As this event is repeated some $N = 10^5$ times, the $\hbar\mathbf{k}$ kicks sum to remove the majority of the atom's original momentum and the $\hbar\mathbf{k}'$ kicks add in quadrature to give an expected final momentum of $\sqrt{N}\hbar\mathbf{k}$, which is only about 1% of the initial momentum. The figure shows the resultant momentum kick for N=4 scattered photons.

In the Zeeman slower, the atoms scatter light from counter-propagating laser light tuned near resonance in a process called Zeeman slowing [115]. Many scattering events reduce the mean velocity of the atoms from a velocity of ~ 800 m/s to ~ 30 m/s, as described in Figure 2-3. Because of the large initial velocity, the atomic resonance is Doppler shifted by ~ 1.5 GHz and a magnetic field profile must be added to Zeeman shift the atoms back on resonance with the laser. The details and characterization of the Science Chamber Zeeman slower can be found in Ref [25].

The Zeeman slower provides a continuous flux of $\sim 10^{11}$ s^{-1} atoms to the main chamber. These atoms are continuously loading into a dark-SPOT [89] magneto-optical trap (MOT) [142], as shown in Figure 2-4. The MOT comprises 3 pairs of counter-propagating laser beams tuned near the $F = 2 \rightarrow F' = 3$ cycling transition which exert a force on outwardly propagating atoms, a spherical quadrupole magnetic field which brings the atoms into resonance with the proper beam, and a repumping laser beam which transfers atoms from the $F = 1$ lower ground state to the $F = 2$ upper ground state when an unfavorable scattering process leaves the atom in the $F = 1$ state. In the MOT, atoms are further cooled to the Doppler limit of 240 μK. Following a brief (~ 5 ms) period of sub-Doppler polarization gradient cooling, atoms are transferred into the magnetic trap.

The Zeeman slower and MOT rely on the scattering of resonant light to corral atoms
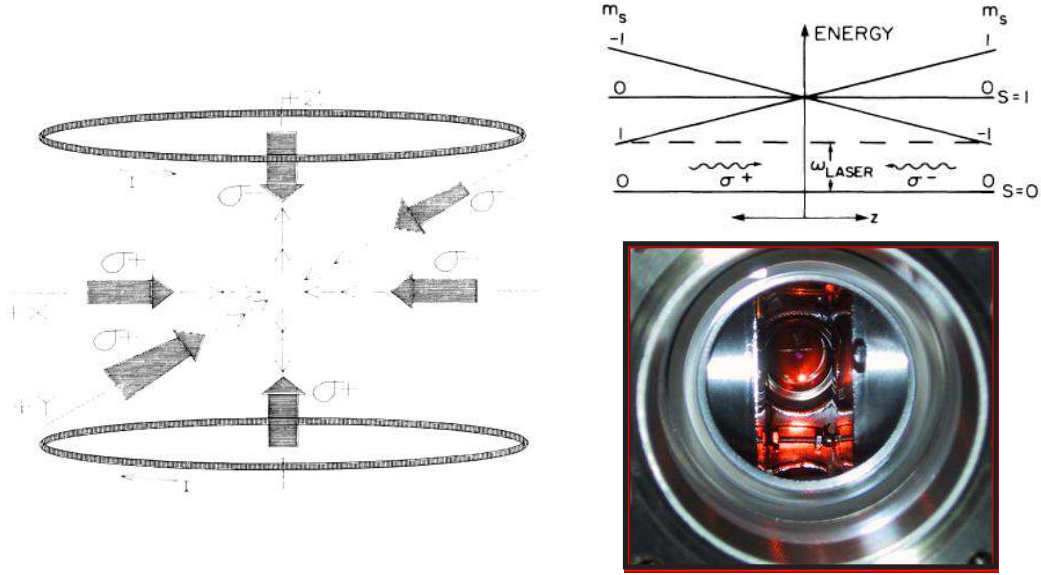
Figure 2-4: The left panel, from Ref. [142], show the field and laser configuration for a magneto-optical trap. The upper right panel, also from Ref. [142], shows how the energy levels of a zero angular momentum ground state (S state) and an excited P state in a hypothetical atom vary spatially in the quadrupole magnetic field, bringing escaping atoms into resonance with the appropriate, counter-propagating MOT beam. The lower right panel is a picture of a MOT through the bucket window of the vacuum chamber.

by "watching" for diffusive motion and opposing with small kicks any atom that is nearing escape. Magnetic trapping of atoms, in contrast, creates a uniform potential of sufficient depth that all atoms are contained by their small kinetic energy, the same way the earth's atmosphere is confined gravitationally. Unlike the slower and MOT which are open systems in which the light can carry away energy, atoms in a magnetic trap, which is a closed system, are not "cooled", and can only exchange kinetic and potential energy with each other and the trap. In order to cool in a magnetic trap, hotter atoms must be removed from the trap. This is accomplished by evaporative cooling [90]; an atom in a "trappable" state is coupled to an "un-trappable" state in a small region of the magnetic trap. This region is initially placed far from the center of the trap so that only the most energetic atoms can reach the region and be ejected from the trap. By selectively removing the high energy tail of the thermal distribution of atoms, the remaining atoms are cooled. As the region is slowly brought closer to the center of the trap, the temperature falls.

2.1.4 Magnetic and optical trapping

Atoms that have a non-zero magnetic moment can be trapped by magnetic fields. When a magnetic moment is oriented along the magnetic field lines (polarized) it experiences an
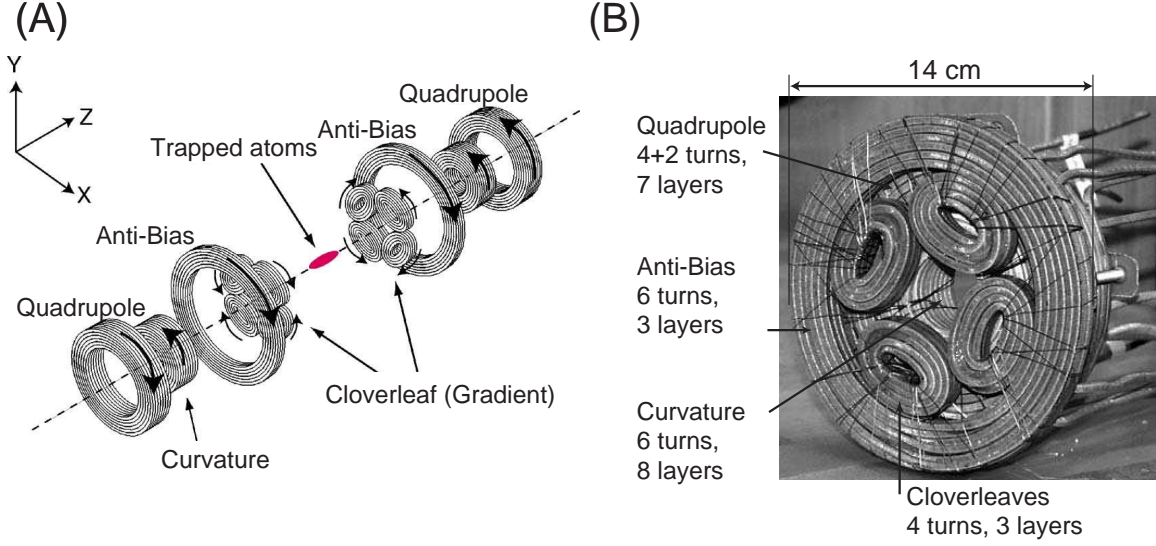
Figure 2-5: Panel A (reproduced from Ref.[182]) shows the assembly of the Science Chamber magnetic trap. Panel B is a photograph of the actual coil before installation with specifications.

energy shift, and therefore a force, due to a magnetic field gradient. The magnetic moment of an atom is quantized with respect to the local field, and can be in a state that is drawn towards regions of larger field or drawn toward regions of smaller field. These states are identified as the strong and weak field seeking states. Strong field seeking atoms are "untrappable" in free space because magnetic field maxima are found only at sources. Magnetic field minima are possible, so the weak field seeking states are "trappable".

The spherical quadrupole magnetic field, generated by a pair of coils running equal currents in opposite directions, creates a central magnetic field zero which traps weak field seeking atoms. As these atoms move away from the center, they enter regions of increasing magnetic field and thus feel a restoring force. Our trap geometry, see Figure 2-5, is slightly more sophisticated than a spherical quadrupole, having a non-zero field minimum in order that the atoms remain polarized in the trap. Our cloverleaf magnetic trap is one form of Ioffe-Pritchard trap [60, 141, 116], and is described in detail in many Ketterle group theses [176, 25, 181]. The MOT windings provide the spherical quadrupole field for the MOT, the curvature and anti-bias windings can provide either a low bias, high curvature field (when $I_{\text{curvature}} = -I_{\text{anti-bias}}$), or high bias, low curvature field (when $I_{\text{curvature}} \approx -0.1 \times I_{\text{anti-bias}}$), and the cloverleaves provide a magnetic field gradient.

In optical trapping, an induced electric dipole moment is generated and manipulated by a strong laser. In a laser field, which is best described as an oscillating electric field, the ground and excited states of a two-level atom are coherently mixed. The resulting mixed states (the "dressed" states) have an energy that depends on the intensity of the

laser field and the detuning of the laser frequency from the atomic transition frequency. Specifically, for red (blue) detuning, that is the laser frequency is lower (higher) than the transition frequency, the mixed ground state has lower (higher) energy for higher laser field intensities. Atoms are therefore drawn into regions of high (low) intensity. This "dipole" force is different than the scattering forces involved with the Zeeman slowing or MOT cooling of atoms as it can be made large in the absence of significant excitation of the atom [115]. Traps using the dipole force for confinement are regarded as conservative.

Optical trapping is central to the "optical tweezers" (optical dipole trap) used to transfer Bose-Einstein condensates from the main chamber to the science chamber [64]. Approximately 1 W of laser power at 1064 nm is focused by a series of lenses to a ~ 25 μm diameter to create a trap in the center of the main chamber. As the laser power is ramped up, the confinement of atoms is transferred from the magnetic field to the optical field until the magnetic confinement may be turned off. The focus is then horizontally translated $\sim$36 cm by horizontally translating one of the focusing lenses. After some hold time to relax the few excitations that result from translation, the condensate is transferred into the experiment by ramping up the experimental trap and reducing the laser field to zero.

2.1.5 Generation of light

The laser light at 589 nm necessary for the experiment is generated by a Coherent 899 dye laser pumped by 8.5 W of 532 nm light from a Spectra Physics Millenia solid state laser on an optical table separate from the experiment. The 899 is locked via saturated absorption spectroscopy 200 MHz from the $F = 2 \rightarrow F = 3$ transition in a vapor cell heated to 95°. A series of acousto-optic modulators (AOMs) shift the frequency of the light to the relevant frequencies, shown in Figure 2-1, and two electro-optic modulators (EOMs) add repumping sidebands to the slower and MOT beams. Optical fibers carry the light between the laser table, pictured in Figure 2-6 and shown in Appendix A of Reference [172], to the experiment table.

Historically BEC III and BEC I shared control and maintenance of a laser table for their experiments. In my first year at MIT, the two groups collaborated to duplicate this system and allow for greater independence, resulting in the Science Chamber Na laser table pictured in Figure 2-6. The separation allowed both machines to be run simultaneously, but has meant increased upkeep for BEC III; the sodium laser's particular sensitivity to fluctuations in temperature is problematic every summer as the temperature control in the experiment room (26-248) shared by Science Chamber and Lithium Lab cannot be maintained by MIT central services as well as the Lithium Lab laser room (26-242). A typical plot of temperature (Figure 2-7) throughout the day shows the uncontrolled rise in temperature. Consequently, the efficiency of experiments in the Science Chamber during
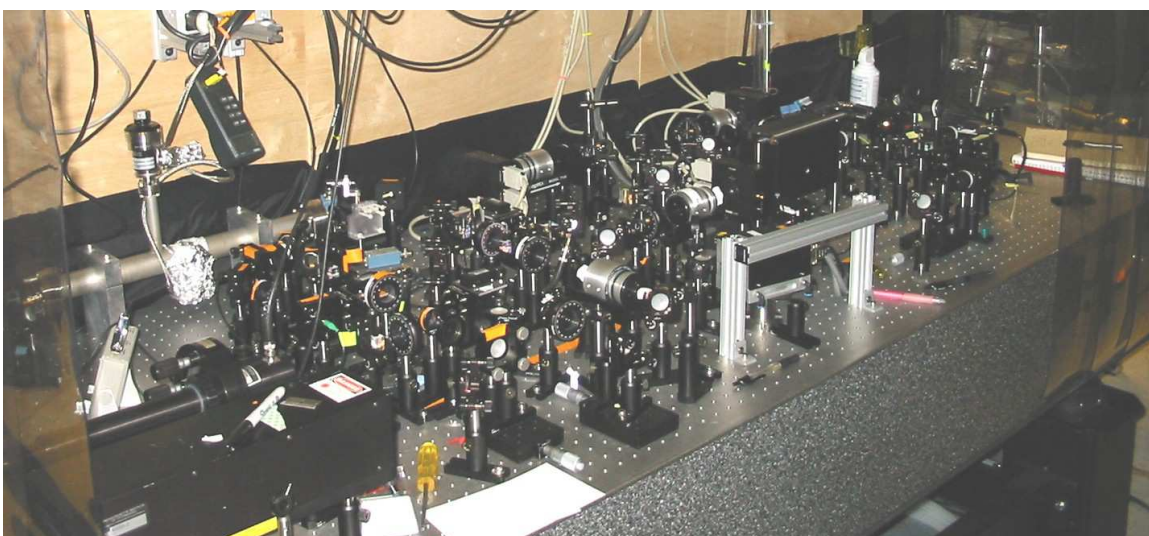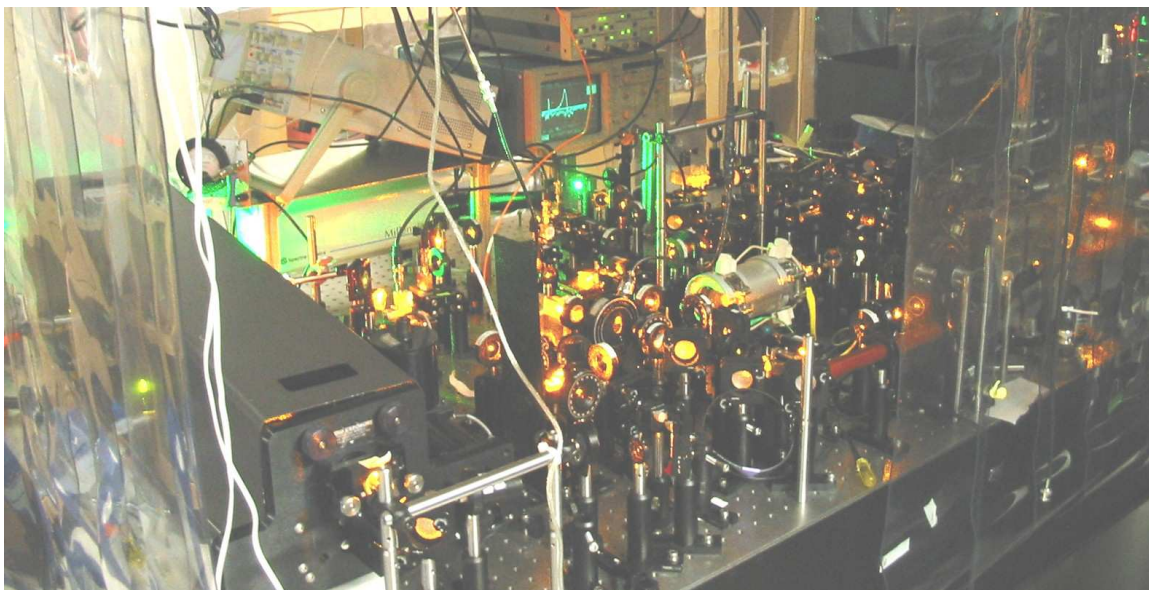
Figure 2-6: The sodium (top) laser and lithium (bottom) laser tables.
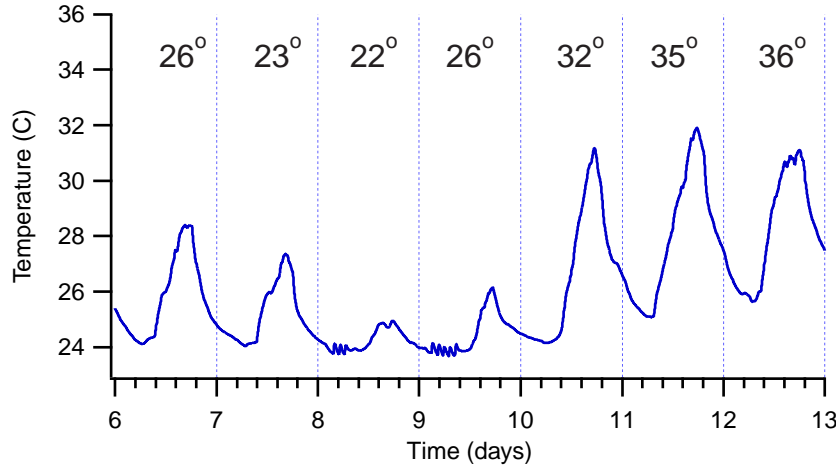
Figure 2-7: A plot of the temperature inside the Na laser table during summer 2007. Grid lines show the approximate location of midnight. The daily outdoor highs are given for each day. Days 8 and 9 are Saturday and Sunday, when the machine was not turned on. The source of the small fluctuations before noon on those days is probably due to the temperature being appropriately regulated by the AC unit to $\pm 0.2°$ C.

the summer is greatly decreased.

2.1.6 Imaging atoms

All data on Bose-Einstein condensates are collected photographically. When a resonant laser beam is shown onto a cloud of atoms, some of the light is scattered, that is, absorbed by the atoms and emitted into a vacuum mode. The beam is now "missing" some photons. By comparing an image of the beam with atoms to an image of the beam without atoms reveals a "shadow" where the BEC "absorbed" light from the beam. This form of imaging is called absorption imaging.

In this work, two forms of absorption imaging are used. In $F = 1$ imaging, atoms in the $F = 1$ lower ground state are imaged with light resonant with the $F = 1$ to $F = 2$ transition. In $F = 2$ imaging, atoms are first optically pumped into the $F = 2$ upper ground state and then imaged on the $F = 2$ to $F = 3$ cycling transition. In $F = 1$ imaging, each atom scatters, on average, two photons before transitioning into a non-resonant state, where as in $F = 2$ imaging atoms at a given density scatter a known fraction of the laser field. Some sample BEC $F = 1$ images are shown in Figure 2-8.

At times, the density of atoms is too high to obtain a decent image or the dimensions of the trapped atoms are too small to be resolved optically. In this situation, the trapping potential can be removed such that the atoms, allowing the atoms to expand as they fall under the influence of gravity. During this "time of flight", the potential energy of the
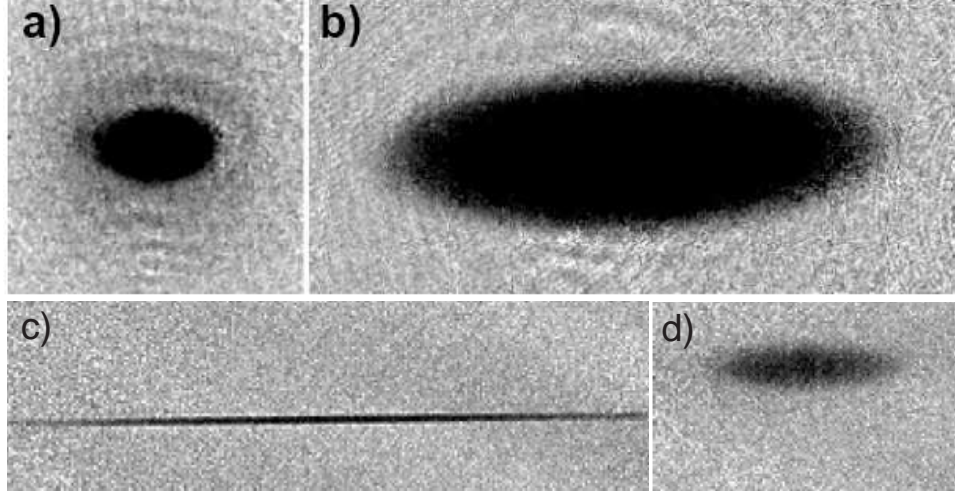
Figure 2-8: Some sample images of BEC. The upper images show a BEC from the main chamber magnetic trap containing a) 3 million atoms with 25 ms time-of-flight and b) 14 million atoms with time-of-flight 65 ms. The lower images show a BEC of 1 million atoms c) in the optical tweezers trap and d) with 10 ms time-of-flight.

trap and the mean-field energy are converted into kinetic energy. The expanded clouds are typically of sufficiently low density to image after ~ 10 ms time of flight. The images shown in Figure 2-8 have differing time of flight from the same trap.

2.1.7 The science chamber

The Science Chamber has enjoyed success in various aspects of condensate physics, continuous BEC [27], BEC interferometry [148], atom chips [82], atom surface interactions [133], and guiding atoms through fibers [189] in large part due to the flexibility of the science chamber at accommodating new experiments on a routine basis. The science chamber, initially a small spherical chamber with an atom chip, a piece of glass for quantum reflection, and a beam shutter for the continuous BEC experiment crammed inside. Since then, the science chamber has been replaced with a 6 inch cube with full sized viewports which can accommodate a wide range of vacuum feedthroughs and provides optical access comparable to the glass cell of BEC II [43]. Of particular note is a stepper motor controlled linear motion feedthrough that was installed and tested during the second quantum reflection experiment.

Linear motion feedthrough

One benefit of the science chamber is the ability to host several experiments simultaneously. To achieve the best control over the externally applied bias fields, however, all experiments
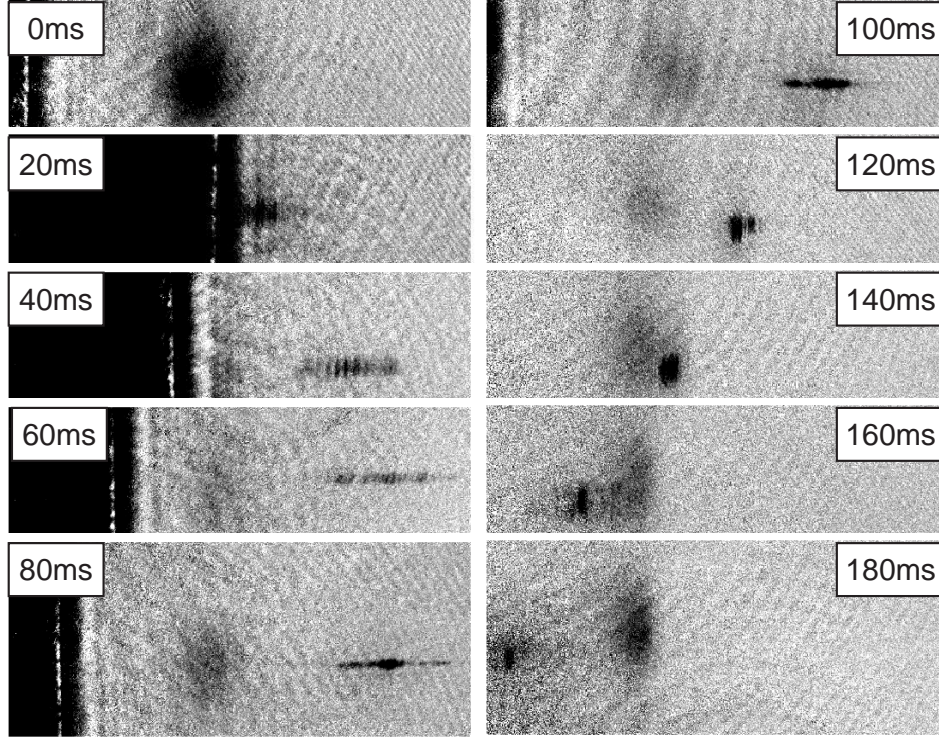
Figure 2-9: A series of quantum reflection images collected by moving the surface into the condensate at 8 mm/s. The surface was stopped in the center of the condensate and immediately removed. It remains visible in the first several images. The center of mass of the reflected atoms oscillates in the trap as expected, but the reflected cloud has "velocity sidebands" of up to ±20% of the center of mass velocity which spatially separate during the dipole oscillation.

would be situated in the center of the science chamber. In the past, we had compromised by running two experiments simultaneously, with each of slightly off center. During the construction of the reduced-density quantum reflection experiment, we wanted to be able to accommodate more than two surfaces and wanted to be able to compare the performance of these surfaces in the same trapping potential. This meant finding some way to reposition the surfaces in vacuum. Further, if the surfaces could be moved relative to the trap, we could "hit the atoms with the surface" rather than "hitting the surface with atoms" during the experiment.

To this end, we installed a linear actuator (MDC part number BLM-133-2-03) in a "mini-flange" port of the custom designed 6-port flange shown in Appendix E. Two of the remaining mini-flange ports were used for electrical connects and the 2 3/4 inch port was used for a window to maintain the imaging axis. The actuator was connected to a "cart on rails" apparatus which held the various surfaces above the single coil, as pictured in Figure 4-2 and shown in Appendix E. The actuator was controlled by a 200 W AC servo

motor (Yaskawa part number SGMAH-02BAN21) fitted with an interface collar and driven by a Legend digital torque amplifier (Yaskawa part number SGDG-04GT). The motor had a built in 13-bit encoder and a maximum angular speed of 5000 rpm, corresponding to a maximum linear velocity of ~ 5 cm/s (1 revolution = 0.025 inches of linear travel). The encoder signal allowed for closed loop control of the angular position to less than 1 μm. A PC interface card (SPiiPlus PCI-4) was used to pre-program and adjust motion waveforms.

The performance of the linear feedthrough apparatus was both good and not good. Point-to-point control of the surfaces was reproducible over many runs of the experiment and the resolution of the system was below the diagnostic limits of our imaging. Additionally, we did not observe any deleterious effects (vibrations, etc.) from the torques generating linear accelerations. However, there were problems with the "smoothness" of acceleration and deceleration. The most telling diagnostic are a series of quantum reflection images that puzzled the group for several weeks, shown in Figure 2-9. While the physics of the observed "velocity sidebands" may be related to the deceleration of the surface at the moment of reflection, we think that the discrete nature of the sidebands must come from the discrete nature of the encoder in the feedback loop.

There are a few other options for generating linear motion in UHV. Of note is the Nanomotion linear motor which interfaces piezo elements with a friction plate to generate nanometer resolution motion with unlimited travel. Some systems are compatible with 10^{-10} Torr.

2.2 The single-coil trap

This section supplements work reported in the following publication, included in Appendix A:

- A. E. Leanhardt, T. A. Pasquini, M. Saba, A. Schirotzek, Y. Shin, D. Kielpinski, D. E. Pritchard, and W. Ketterle *"Cooling Bose-Einstein condensates below 500 picokelvin"*, Science **301**, 1513 (2003).

Many of the experiments described in this work were performed in a trapping geometry designed and implemented during my first year at MIT. The "single-coil" trap or "gravito-magnetic" trap rivals the planar "z-trap" for simplicity. The single coil trap comprises a single current-carrying coil to provide a magnetic field gradient which levitates the atoms against gravity and an external bias field to create an on-axis field minimum which confines the atoms in the horizontal plane[1]. The defining characteristics of the single-coil trap are

---

[1]We were interested to learn, after the fact, that the single coil trap had been described previously by Chris Monroe for the trapping of cesium atoms. A similar trap geometry, the opposed coil trap, was used to trap cesium atoms [121]

extremely low mean trap frequencies (on the order of a few Hertz) and densities (on the order of 10^{11} atoms/cm^3) in a geometry that ranges from spherical to "pancake". Through adiabatic decompression, the single-coil trap has been used to create the coldest manmade temperatures [99, 49] of 450 picokelvin for samples of a few thousand atoms.

The single coil trap is a specialty of our labs, crucial to the quantum reflection experiments presented here, and quickly becoming unfamiliar on the hallway. This section is therefore intended as both a primer and a troubleshooting guide. The section begins with an analysis of the hypothetical "single loop" trap, much of which directly extends to the many-loop single coil trap. The sensitivities of the single coil trap and some standard techniques for using the single coil trap are then discussed.

2.2.1 Single-loop trap geometry

A single loop of radius R carrying current I creates an on-axis magnetic field profile that is a maximum at the center of the coil and falls off with height z as

$$B_z = \frac{\mu_0 I}{2} \frac{R^2}{(R^2 + z^2)^{3/2}} \tag{2.1}$$

where μ_0 is the permeability of free space. The gradient of this field,

$$B_z' = -\frac{\mu_0 I}{2} \frac{3R^2 z}{(R^2 + z^2)^{5/2}} \tag{2.2}$$

will exert a force, $F_B = \mu B'$, on an atom with magnetic moment μ. In the single loop trap, this force is used to balance the force of gravity on the atoms, giving an expression for the required levitating gradient $B_0' = 2mg/\mu_B \approx 8$G/cm where m is the mass of the atom, g is the acceleration due to gravity and we have used $\mu = \mu_B/2$ as the magnetic moment of ^{23}Na in the $F = 1$, $m_F = -1$ state, where μ_B is the Bohr magneton. Because the force of gravity on the atom is constant, but F_B falls off with z, there is, given sufficiently large I, a point above the loop where the magnetic force balances the gravitational force, as shown in Figure 2-10. There are typically two real roots to the expression $mg = \mu_B/2 \times B'$; the smaller of these roots is not a stable trapping point because the curvature is negative below $z = R/2$. The expression for the trapping minimum, z_0, is easily found by selecting the correct root when substituting B_0' into the above expression. As the current in the loop is decreased, z_0 moves closer to the $z = R/2$. Below the threshold current, $I_{min} \approx 4.66 \times mgR^2/\mu_B\mu_0$, there is no point with sufficient gradient to levitate a sodium atom.

The resulting trapping potential, $V_z = \mu B + mgz$, is not harmonic in z, as is readily apparent from Figure 2-10, but may be approximated as harmonic for small oscillation amplitude. The trap frequency is found from the second derivative of the potential as
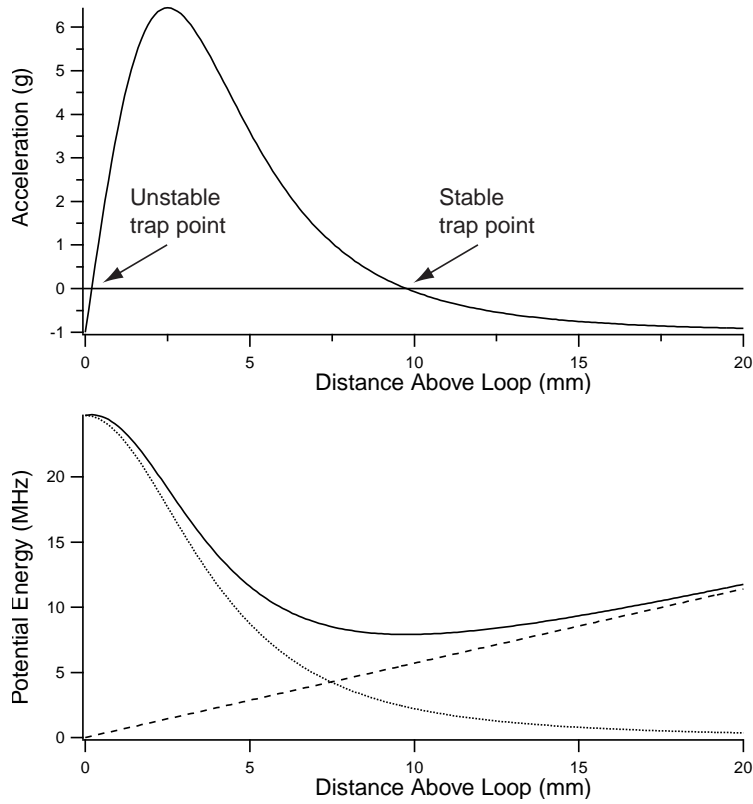
Figure 2-10: In the vertical direction, the force on an atom due to the gradient of the magnetic field of a single loop is used to balance the force of gravity. The top panel shows the acceleration (in units of g) of a ^{23}Na atom above a 1 cm diameter loop running 28 A. The zero crossing is the vertical trapping position, z_0. The total trapping potential (solid line) is the sum of the gravitational potential (dashed line) and the magnetic potential (dotted line), shown in the bottom panel. The potential can be approximated as harmonic for small displacements.
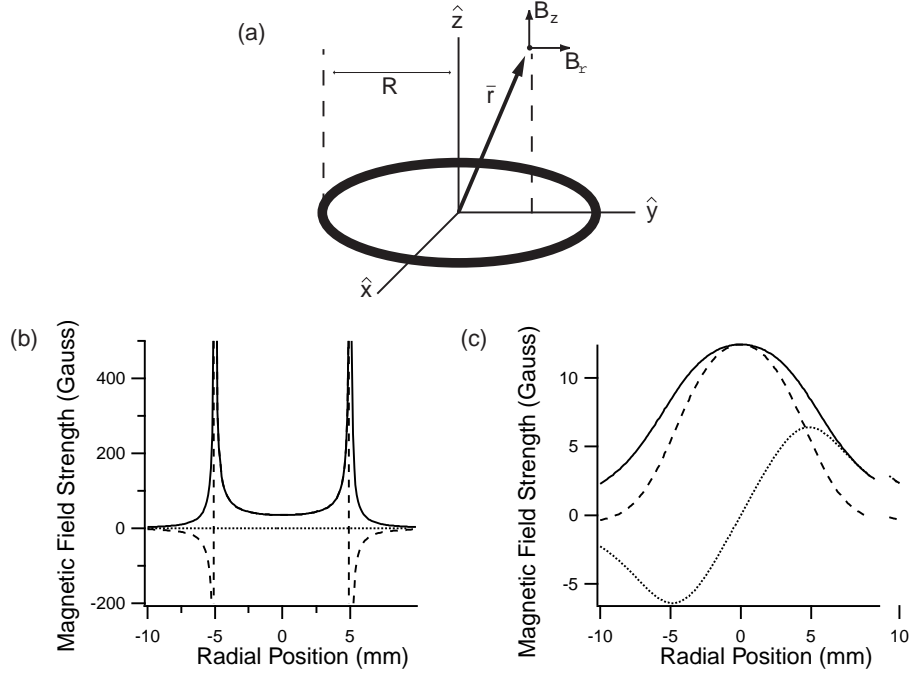
Figure 2-11: The geometry for the magnetic field calculations. (a) The coil resides in the x-y plane. The magnetic field profiles for $B_z(\rho)$ (dashed), $B_\rho(\rho)$ (dotted), and $B_{tot}(\rho)$ (solid) are shown for (b) $z = 0$ and (c) $z = R$.

$f_z = \omega_z/2\pi = 1/2\pi \times (V_z''/m)^{1/2}$. Within the experimentally relevant region ($z_0 >$R), tighter (looser) confinement in the vertical direction can be obtained by working closer to (further from) the loop where the field curvature is larger (smaller) or by working with a smaller (larger) radius loop which provides a larger (smaller) field curvature. The vertical trap frequency is fairly insensitive to z_0, varying only by a factor of 2 over the range $R < z < 2R$. It should also be noted that adding a bias field in the z direction, as is necessary for radial confinement, will not change the location of the trap minimum or change the vertical trapping frequency.

Support against gravity is necessary, but not sufficient, to provide three-dimensional confinement for atoms. In order for the atom to be confined radially, we require that the on-axis magnetic field be a local minimum (positive radial curvature). In this scenario, atoms in the weak field seeking state will be drawn toward the axis. Analytic off-axis calculations of the magnetic field of a loop are notoriously un-illuminating, involving elliptic integrals and requiring numeric evaluation. Reasonable treatments use the vector potential as in Jackson [79] or the Biot-Savart law as in Griffiths [62]. However, by approximating the off axis field to second order, some general observations can be made [12].

44

Maxwell's equations constrain the behavior of static fields [190, 121, 149]. Specifically,

$$\sum^{i=3} \frac{\partial B_i}{\partial x_i} = 0 \tag{2.3}$$

$$\frac{\partial B_i}{\partial x_j} = \frac{\partial B_j}{\partial x_i} \tag{2.4}$$

If we approximate the vertical field at the trap position to second order as: $B_z = B_0 + (mg/\mu)z + \kappa_z z^2 + \kappa_\rho \rho^2$, Maxwell's equations require that $B_\rho = -(mg/\mu)\rho - 4\kappa_1 z\rho$ and $2\kappa_2 = \kappa_1$. We therefore write

$$B_z = B_0 + \frac{mg}{\mu}z + \kappa(z^2 - \frac{1}{2}\rho^2) \tag{2.5}$$

$$B_\rho = -\frac{mg}{2\mu}\rho - \kappa\rho z \tag{2.6}$$

Close to the axis of the loop, the total magnetic field, $B_{\text{tot}}(z\rho) = \sqrt{B_z^2 + B_\rho^2}$, is dominated by B_z, with B_ρ increasing roughly linearly off-axis. When the fields add in quadrature, the term linear in ρ in B_ρ combines with the bias field B_0 to give a total field with a lowest order quadratic dependence $B_{tot} \approx B_0 + ([B_z']^2/8B_0)\rho^2$. The radial trap frequency proportional to $B_r'/\sqrt{B_0}$. An exact calculation of the near-axis magnetic field is shown in Figure 2-11.

In the plane of the loop, the radial curvature of the total magnetic field is positive, providing a radially confining potential $V_\rho = \mu B_{\text{tot}}(\rho)$. Out of the plane of the loop, the radial curvature of the total magnetic field decreases from its on-axis maximum, eventually becomes negative (anti-trapping) at a height, $z_{0\text{curv}} \simeq 0.63 \times R$, as shown in Figure 2-12. The radial curvature reaches a minimum value at $z_{\text{mincurv}} \simeq 0.98 \times R$, before increasing to zero at $z = \infty$.

The isolated single loop, then, has a 3D stable trapping point for height $0.5R < z_0 < 0.63R$. The current running in the loop must be chosen to provide the appropriate vertical gradient to support atoms against gravity. The minimum 3D trap frequency is found with z_0 close to $0.63R$.

In practice, it is useful to trap atoms further from the plane of the loop, where the radial curvature due to the loop current is negative. This is accomplished by introducing a singularity in the potential experienced by the atoms. By applying an "anti-bias" field, B_{anti} in the z direction, B_z is completely canceled on-axis at a height z'. At this point, B_{tot} is dominated by B_ρ, which increases *linearly* off-axis. The discontinuity in B_{tot}' becomes a positive singularity in the radial curvature, as shown in Figure 2-13(a). This extends the range of positive curvature to all points above the loop, excepting a small region between $z_{0\text{curv}}$ and the zero crossing created by the singularity. This technique has the further benefit of independent control of the vertical trapping position and the radial trap frequency, as
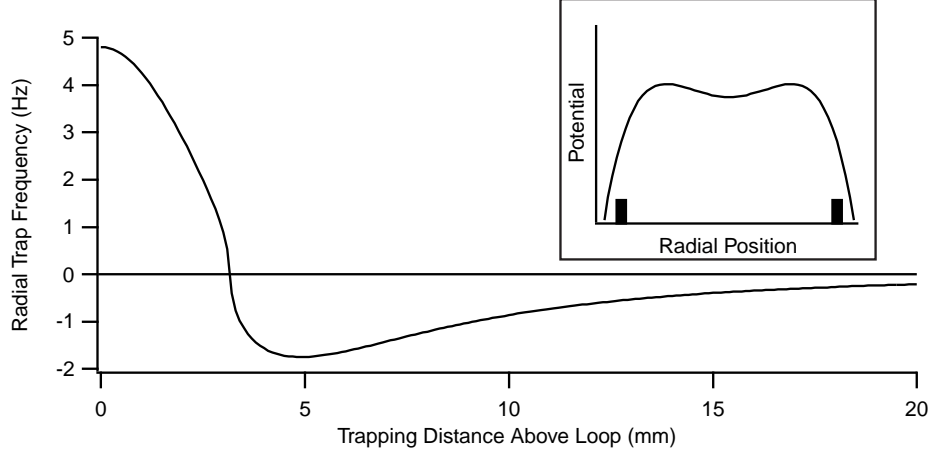
Figure 2-12: The radial trap frequency as a function of z for a 1 cm diameter loop carrying 1A. The trap frequency scales as the square root of the current, so the value of ω_ρ can be found by scaling this plot by $\sqrt{I}$. Negative values for the trap frequency indicate an "anti-trapping", negative curvature. The inset shows the radial potential topology for typical trapping parameters. The limited trap depth is discussed in Section 2.2.3.

shown in Figure 2-13(b). With z_0 set by the loop current I, the radial trap frequency can be varied between zero and any positive value by changing the value of the anti-bias field. Atoms can be loaded into a tightly confining trap and adiabatically decompressed (and cooled) by decreasing or increasing the anti-bias field and moving the location of the singularity.

In a common situation, the loop is actually a series of loops comprising a coil. Most of the "loop" analysis above transfers directly to the "coil" analysis by careful accounting of the magnetic field produced by each winding. In practice, such calculations are overkill when atoms are supported more than a loop radius away from the center of the coil. Comparisons for the single coil used in this experiment to a single loop are shown in Figure 2-14. The coil shows a slightly decreased (about 10%) vertical trap frequency for a given trapping height. The only major difference is in the current required. Significantly less current is required to levitate atoms at a given height when the current passes through several, tightly wound loops. Because the radial trap frequencies are controlled by a bias field, any change associated with the coil configuration can be compensated by changing the bias field slightly.

To summarize the single coil trap: a single coil can support atoms against gravity by balancing the force of gravity with the force on the magnetic moment of the atom from the magnetic field gradient; the horizontal confinement of the atom is achieved by adjusting an anti-bias field, ensuring that the total magnetic field is a minimum on axis.
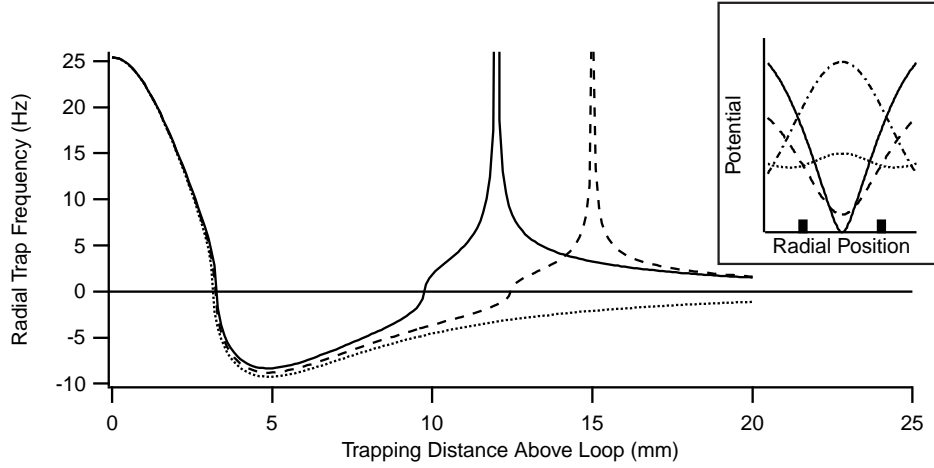
Figure 2-13: The single loop trap with an applied anti-bias field. The magnitude of the anti-bias field was selected to exactly cancel B_z for a 1 cm diameter coil carrying 28 A ($z_0 \approx 1$ cm) at $z = 1.5R$ (dashed line) and $z = 1.2R$ (solid line). The zero bias field line is shown for reference (dotted line). For the solid (dashed) line case, the radial trap frequency is $\sim$2 Hz ($\sim$85 Hz) at z_0. The inset shows V_ρ at $z = R$ for various anti-bias field strengths; B_{anti} =0 (dot-dashed line), 1.5 G (dotted line), 2.5 G (dashed line), and 3.5 G (solid line). An on-axis field maximum is turned into an on axis minimum. The large tick marks represent the location of the coil. The overall offset of the potential is unimportant.
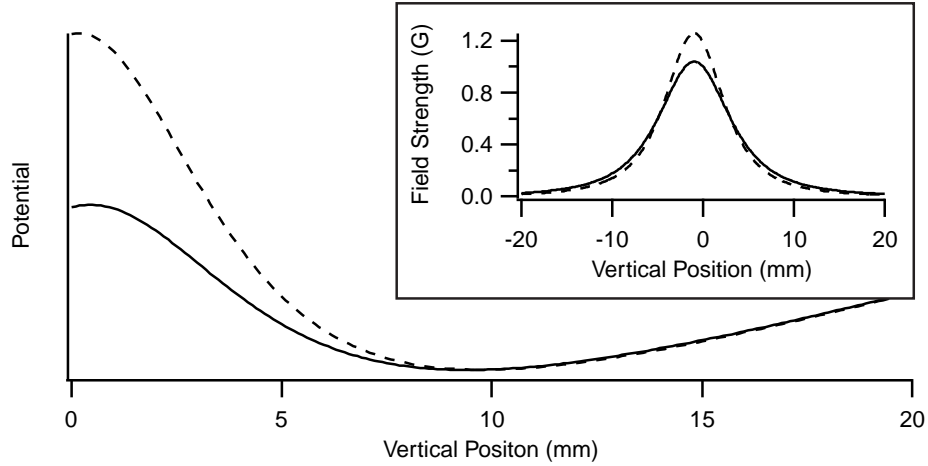
Figure 2-14: The vertical trapping potential for a single loop (dashed line) compared to a single coil (solid line) for a constant trapping position, $z_0 \approx 1$ cm. The vertical trap frequency for the coil is reduced by approximately 10%. The inset shows the on axis magnetic field strength for the single loop running 1 A (dashed line) and single coil with integrated current 1 A (solid line).

47

2.2.2 Sensitivity of the single-coil trap to external fields

One of the challenges of working with the single-coil trap is its sensitivity to external magnetic fields. At this point, we have only considered the field of the coil and an external, vertical anti-bias magnetic field. We now discuss the effect of (a) external bias fields in the horizontal (X-Y) plane and (b) magnetic field gradients.

Bias fields in the horizontal plane shift the position of the magnetic field minimum off axis. Without a bias field, the B_ρ is zero on axis; and the addition of a bias field, ΔB moves the location of the zero off axis by approximately $\Delta B/B'_\rho$. For the typical trapping parameters of $R = 5$ mm, $I = 28$ A, $z_0 = 1$ cm, and $\omega_\rho = 5$ Hz give a residual bias field of $B_{\text{tot}} \approx 1$ G. Adding a 1% horizontal bias field of 10 mG shifts in the point where $B_\rho = 0$ off axis by 25 μm and the trapping position 60 μm off axis. These distances are comparable to typical condensate length scales. The shift off axis changes the trap frequency by less than 0.1% and, as such, a jump in the horizontal bias field will "kick" the trapped atoms, providing a useful mechanism for measuring a trap frequency.

It is worth noting that the horizontal component of the Earth's magnetic field in Boston is roughly 200 mG [187], which, unless compensated, will shift the trap position roughly 1 mm off axis and therefore must be compensated in our experiments.

External magnetic field gradients are less prevalent than bias fields, and their effect on the trap less important. Vertical gradients will exert a force on the atoms which will add or subtract from the force of gravity. It is unlikely, therefore, that vertical gradients would be detected unless they were transient. Near the axis, B_ρ changes linearly, so adding a gradient would just emphasize or de-emphasize the role of B_ρ, increasing or decreasing the trap frequency correspondingly. The greatest impact of a horizontal gradient is to break the cylindrical symmetry of the trap, giving different trap frequencies in the direction parallel to and perpendicular to the gradient.

Static magnetic fields and gradients, then, are a significant, but not major, hassle when working with the single coil trap. Transient fields, however, can be very troublesome. In any trap, the timescales for relaxation scale with the trap frequency; excitations in the single coil trap damp some tens of times slower than in the ODT or a chip-based wire trap. Furthermore, the electronic noise at low frequencies may be larger. Experiments in the single coil trap take seconds to perform as opposed to milliseconds, creating large temporal windows for excitations to enter the system.

One notable source of transient excitations is the Lithium Lab magnetic trap, used to create kG bias fields for working with Feshbach resonances. These fields are generated approximately by a pair of coils run in Helmholtz configuration roughly 2.5 m away from the Science Chamber apparatus. The fields fall off as $\sim 1/r^3$, which drops the field by a factor of $\sim 10^4$, meaning that the residual field is several 10s of mG. This is sufficient to
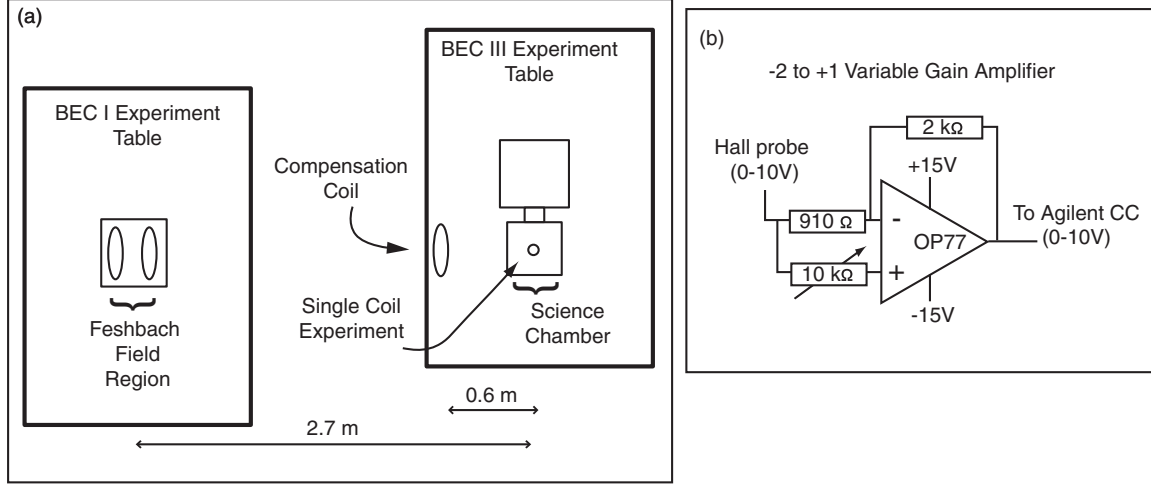
Figure 2-15: a) The Feshbach coils of the BEC I experiment and science chamber y-bias coils of the BEC III experiment are collinear. (b) The current in the BEC I Feshbach coils is monitored by a Hall probe. A proportional current through the compensation coil, tuned using the above circuit, will cancel the magnetic field above the single coil experiment.

shift the horizontal trap position more than 1 mm when the coils are running.

To protect against these transient fields and allow both experiments to be run simultaneously, we considered both passive and active stabilization techniques, finally settling on a compensation coil installed collinearly between the two experiments, as shown in Figure 2-15. Conveniently, the axis of the Li Feshbach coils is aligned with the axis of the science chamber. A pickup circuit was installed, see Figure 2-15, to monitor the current in the Li Feshbach coil and apply a proportional current in the compensation coil. The current in the compensation coil generated a field that canceled the field of the Li Feshbach coils in the center of the chamber. When put into operation, the compensation coil removed any measurable effect. As a negative side effect, the compensation coil introduced a stray magnetic field gradient of about 3 mG/cm (up from 0.7 mG/cm with the Feshbach coil).

A second technique considered for maintaining field stability inside the science chamber was the installation of a passive high magnetic permeability (mu-metal) shield around the chamber. Such shields are in wide use in precision experiments and can reduce field strengths by orders of magnitude. Ultimately, this choice was unwieldy because of the size of the region to be shielded (the external bias field coils must be enclosed by the shield) and the proximity of stray field sources, like ion pump magnets, whose field lines could be concentrated by the optical apertures in the shield.

A third technique, still in development, was small, vacuum compatible magnetic field sensors. An array of such sensors could be used to actively monitor the field inside the science chamber and correct for fluctuations by feeding back on the external bias coils.
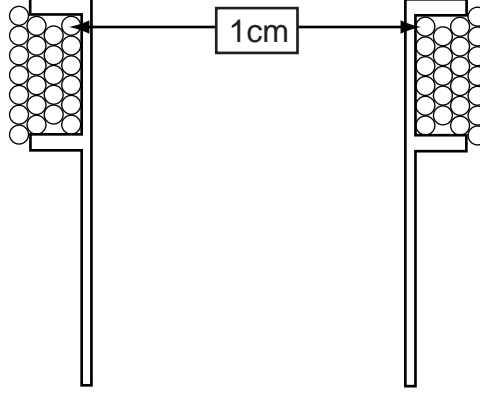
Figure 2-16: Winding pattern for the single coil used in the quantum reflection experiments. The loops were supported by an aluminum cylinder, also used for mounting purposes.

Such a system may be considered for future applications.

2.2.3 Experimental single-coil trap

Having established the theoretical operation of the single coil trap, we turn now to the implementation of the single coil trap used for the first quantum reflection experiment. The coil comprised 24 turns of Kapton coated 30 gauge wire (0.5 mm diameter with coating) in an aluminum holder, configured as in Figure 2-16. The coil was coated in an electrically insulating, vacuum compatible epoxy (Epo-Tek H77 Epoxy). The final trapping position was on-axis approximately 8 mm above the 10.5 mm (average) diameter coil, well outside of the zero-bias trapping region. The anti-bias field was provided by a pair of 10 cm diameter coils mounted outside of the science chamber (the z-bias coils).

The single coil trap is characterized by three trap frequencies, the vertical trap frequency and two horizontal trap frequencies. For a given coil geometry, the vertical trap frequency is purely a function of the vertical trapping position, z_0, while the horizontal trap frequency depends on both the vertical trapping position and the applied anti-bias field. These trap frequencies are easily measured by (1) changing the current running in the single coil or (2) applying an external, horizontal bias field. The vertical trap position can be changed by changing the coil current. Typically a change of a few tens of milliamps is sufficient to induce a small amplitude oscillation that is monitored to give the vertical trap frequency. As discussed in Section 2.2.2, the addition of a horizontal bias field shifts the trap center off-axis. Typically a field of a few tens of milligauss is sufficient for measuring a horizontal trap frequency. In the quantum reflection experiment, the angular trap frequencies are typically held at in the range of $(\omega_z, \omega_x, \omega_y) = 2\pi \times (8, 4, 5)$ Hz or $(6, 2, 2.5)$ Hz.

Condensates of ^{23}Na were transferred into the science chamber with optical tweezers
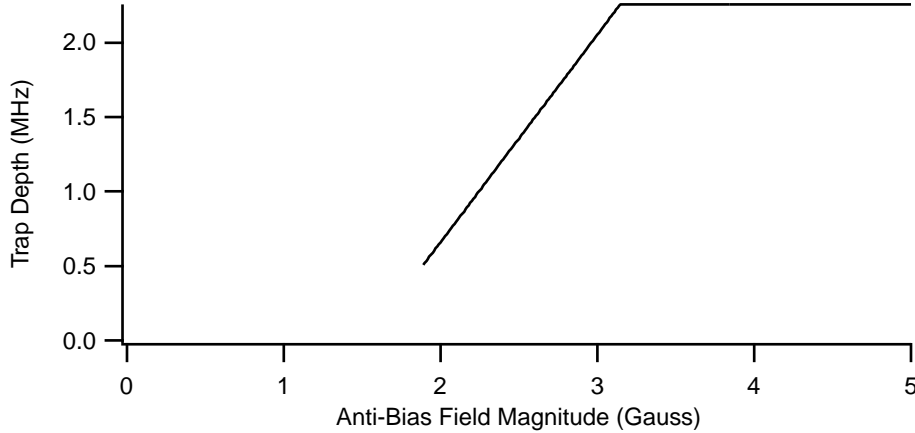
Figure 2-17: Trap depth for the single coil vs. applied anti-bias field. Calculations are done with a 1 cm diameter coil running 28 A, where $z_0 \approx 1$ cm.

in the usual way, described in Section 2.1.4. Once in position above the single coil, the currents in the single coil and the external bias coils were ramped up over 2 s after which the power in the tweezers beam was ramped to zero over 2 s. Regardless of the desired final trap frequencies, transfer was always done into the "compressed" trap with $(\omega_z, \omega_x, \omega_y) = 2\pi \times (8, 4, 5)$ Hz. Typically, the two traps would need to be aligned on a daily basis. The horizontal alignment was more sensitive than the vertical alignment. Because the combined single coil/tweezers trap was dominated by the optical potential of the tweezers, alignment was monitored by looking for center of mass oscillations in the condensate after transfer. The current in the single coil was adjusted to compensate for vertical misalignment and the external x and y-bias fields were adjusted to compensate for horizontal misalignment. Transfer into the single coil trap was nearly lossless, leading to approximately 5×10^5 atoms in the trap.

Following the transfer into the single coil trap, the final trapping parameters were adjusted. The vertical trap position was adjusted first by increasing current in the single coil. The anti-bias and horizontal bias fields also required slight adjustments during this "rising" stage. The timescale for rising, about 5 s followed by a 4 s hold time, was set by the need to remain adiabatic with respect to the low trap frequency. The final horizontal trap frequencies were then adjusted via adiabatic decompression by reducing the anti-bias field over 5 s, as suggested by Figure 2-13. Again during decompression, the horizontal bias fields were adjusted slightly to maintain the horizontal trapping position. In the second quantum reflection experiment, the atoms could be delivered to the science chamber at the correct vertical position, owing to the translation of the surfaces, so only the decompression stage was necessary.
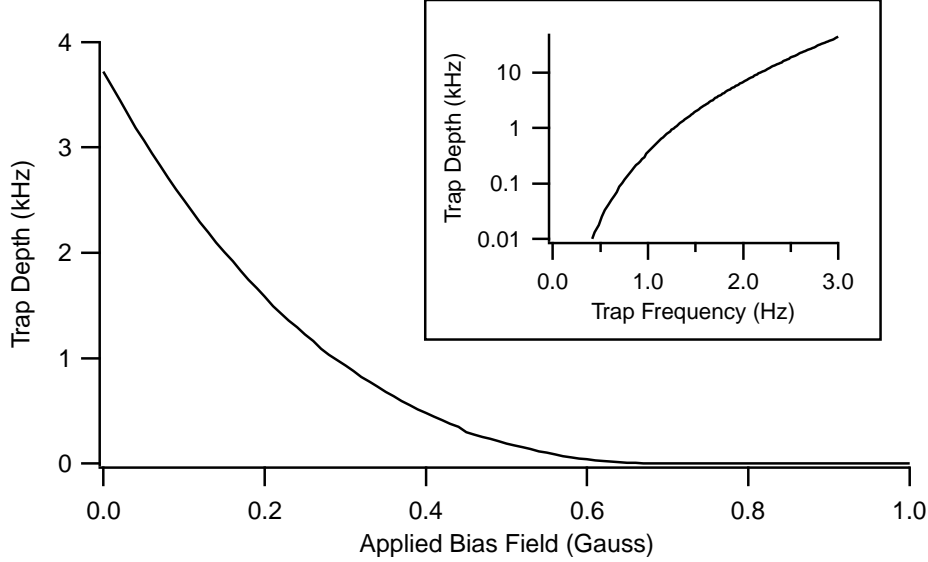
Figure 2-18: Trap depth for the single loop vs. applied bias in the "bias-free" trapping region between $0.5R$ and $0.63R$. Calculations are done with a 1 cm diameter coil running 3.85 A, where $z_0 \approx 0.3$ cm. The inset shows how the trap depth varies with the trap frequency as the bias field is applied.

For a single atom, it is possible to reduce the horizontal trap frequencies without limit. However, for a condensate with mean-field interactions, the depth of the trap might ultimately limit decompression. Because for $\rho > R$, $V_\rho(\rho)$ falls to zero, the trap depth is defined as the difference between the maximum of $V_\rho(\rho)$ and the on axis local minimum $V_\rho(0)$. Because the radial trap frequency scales as $B'_\rho/\sqrt{B_0}$ and $B'_\rho = B'_z/2$ is fixed, the trap frequency can be reduced to zero by increasing the on axis bias field to zero.

First, we consider the case where the atoms are trapped at $z > 0.63R$, such that an anti-bias field is required to create a radial minimum on axis. There are two regimes determined by the location of the trapping height relative to the singularity of Figure 2-13. When the anti-bias field is just sufficient to provide a radial trapping potential, the trap depth due to the quartic term in the potential V_ρ is already significant, approximately $h\times500$ kHz. Increasing the anti-bias field will *decrease* B_0 on axis and *increase* the trap depth until the singularity reaches the trapping point, as shown in Figure 2-17. Further increasing the anti-bias field beyond this point will gradually decrease the trap frequency to zero while maintaining substantial trap depth (~ 2 MHz at $B_{anti} = \infty$). For comparison, the vertical trap depth, which is asymmetric due to gravity, is approximately 17 MHz in the $-\hat{z}$ direction and infinite in the $+\hat{z}$ direction.

Trap depth limitation during decompression is more significant when the trap is operated in the "bias-free" region between $0.5R$ and $0.63R$, that is, where a bias field need not be

Trap Geometry	$\omega/2\pi$ (Hz)	N (atoms)	T_C (nK)	n_0 (cm^{-3})
Magnetic trap (evaporation)	$(20, 200, 200)$	10^7	1000	3×10^{14}
ODT (tweezers)	$(4, 440, 440)$	2×10^6	500	10^{14}
Atom Chip trap	$(10, 2000, 2000)$	10^6	1500	10^{15}
Single coil	$(8, 4, 4)$	10^6	25	5×10^{12}
Single coil (decompressed)	$(2, 1, 1)$	10^5	2	5×10^{10}

Table 2.2: A comparison of parameters for the various trapping geometries used in the Science Chamber. The parameters are the typical angular trap frequency ω, the typical condensate atom number N, the condensate transition temperature T_C and the central atom number density n_0.

applied to achieve a 3D trapping potential. When decompression is attempted in this regime by applying a bias field (as opposed to an anti-bias field), the trap frequencies are reduced to zero at the expense of the trap depth, as shown in Figure 2-18. The opposite sign of the quartic term in B_{tot} is responsible for the limiting trap depth, a difference which can be seen by comparing the insets of Figure 2-12 and Figure 2-13.

2.2.4 Further applications of the single-coil trap

The single coil trap provides unique access to ultra-low temperatures and ultra-low densities, as shown in Table 2.2. Low temperatures and densities are useful for precision metrology, where Doppler broadening and collisional broadening and line shifts must be controlled. When the number density is so low, on the order of 10^{11} cm^{-3}, the interactions between atoms in a condensate are drastically reduced. Reducing interactions has proved useful in some atom interferometry schemes [186, 76]. The single coil also provides support against gravity with minimal radial confinement, which may be useful for lattice experiments where external harmonic confinement is undesirable.

2.3 Modifications for dual species work

In 2006, one of the major frontiers cold atom physics lay in the merging of two recently developed fields: optical lattice potentials for ultracold gases and well controlled interactions with ultracold fermions. As a group, BEC III realized that, while high quality physics remained in studies of pure BEC, the best direction for the lab was to put fermions in optical lattices. Preliminary studies in this field were, literally, surrounding us in the major results of BEC I [196], BEC II [19], and BEC IV [28]. Not wanting to fall behind our hall mates, and with a cautious optimism that defines any major operation, we decided to upgrade our machine to incorporate fermionic lithium [57].

The Science Chamber apparatus is ideally suited for the demands of optical lattice

science. Transfer to the science chamber should be possible for ultracold fermions, possibly for bosons and fermions simultaneously, and the auxiliary chamber can be reconfigured, as was done in BEC IV [16], for optical lattices.

This section will detail a few of the upgrades made over the last year.

2.3.1 Multi-species oven

Lithium atoms were introduced to the vacuum system via a dual-species oven designed for the BEC I experiment by Claudiu Stan [178, 177] which replaced the sodium oven [25]. The basic design involves two isolated atomic sources which are connected by a small nozzle which allows the species to mix. A second nozzle in the "mixing chamber" creates the effusive beam that is coupled into the Zeeman slower. The system was so successful that it was installed on the BEC II apparatus in 2004 and on our experiment in 2007. The installation proceeded smoothly and the system appears to be robust.

2.3.2 Lithium laser table

Because $\sim 90\%$ of the vacuum system remained unchanged, the major component of the lithium upgrade was the design and construction of the laser source. We considered two schemes: a single source design involving a tapered amplifier and a distributed source design using the recently developed Mitsubishi slave diodes. Both schemes were successfully in use along the hallway; BEC I had developed the Mitsubishi diodes to viability and BEC II had recently acquired a tapered amplifier system. At the time, neither system seemed to be the overwhelming favorite, so, due to the availability of parts on the shelf, we chose to work with the slave diode scheme.

In the slave diode scheme, a master laser (Toptica DL 100 grating stabilized diode laser) generates ~ 25 mW of optical power near the lithium $D2$ transition wavelength of 671 nm. Acousto-optic modulators are used to generate the various frequencies needed for optical trapping, slowing and imaging. These low-power ~ 3 mW beams are coupled into slave diodes where they are amplified to high-power ~ 100 mW, while retaining the narrow spectral characteristics of the master laser. The beams are then shaped, coupled into optical fibers and transferred to the experiment. Details of the experimental techniques associated with maintaining the slave locking are found in the excellent Appendix of Ref. [66]. The only major difference between our laser scheme and the one described in Ref. [66] is that we use an EOM to generate repumping sidebands on the slower beam rather than using modulating the slower slave diode. A schematic of the table is shown in Figure 2-19 and a picture is shown in Figure 2-6.
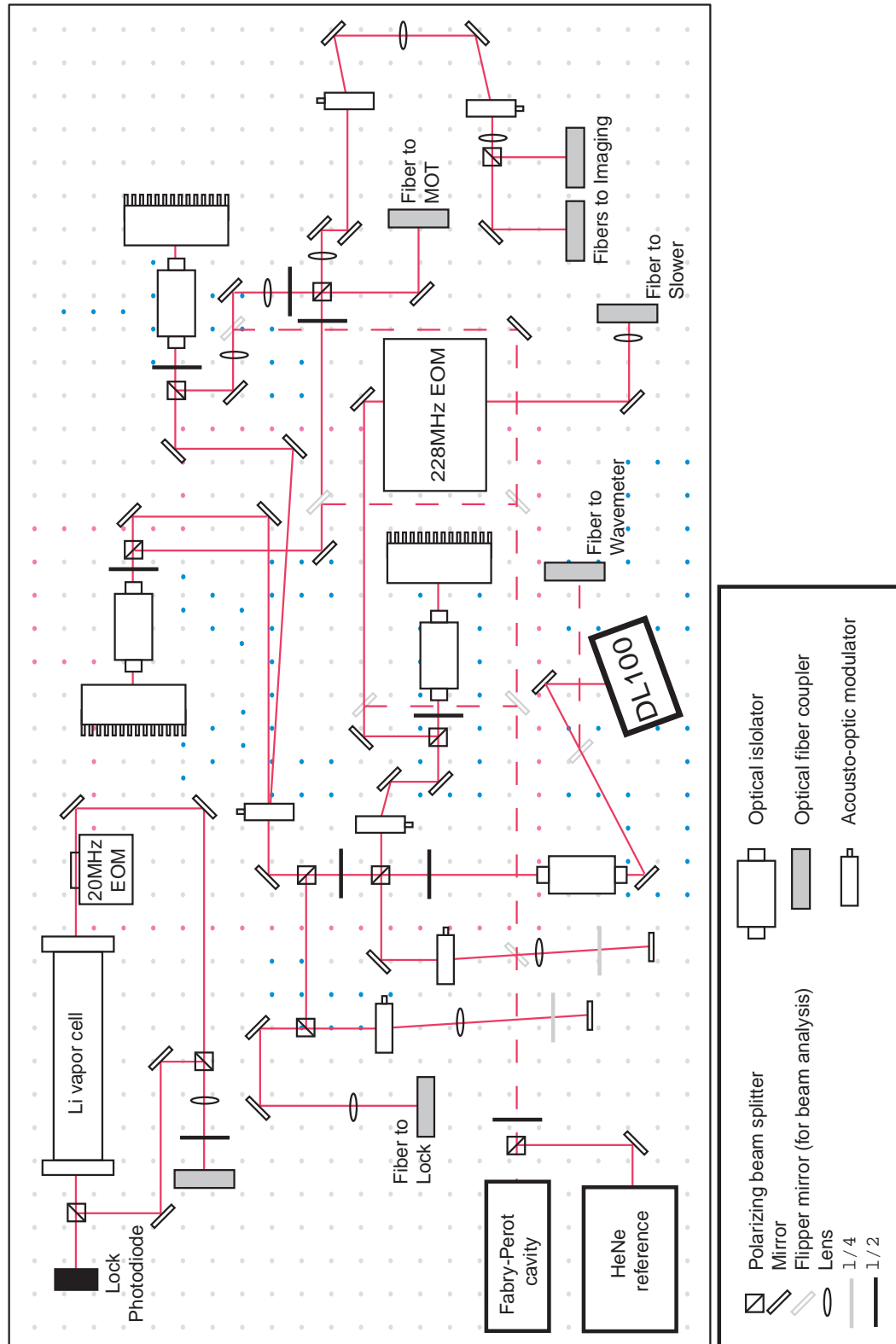
Figure 2-19: Lithium laser table layout. Dashed beam lines derive from flipper mirrors and are typically not present on the table.

Fiber to MOT

Fibers to Imaging

Fiber to Slower

228MHz EOM

Fiber to Wavemeter

DL100

20MHz EOM

Li vapor cell

Fiber to Lock

Fabry-Perot cavity

HeNe reference

Lock Photodiode

Optical islolator

Optical fiber coupler

Acousto-optic modulator

Polarizing beam splitter
Mirror
Flipper mirror (for beam analysis)
Lens
1/4
1/2

AOM driver power supplies

During the development of the laser table, we were troubled with electronic noise in the frequency range of 20-100 kHz. Eventually, we traced the problem to switching power supplies in use in the AOM drivers we had built and were able to mitigate the problem by exchanging the switching power supplies with linear power supplies. Linear power supplies generate voltages by step-down transforming an AC line, then rectifying and regulating the output voltage. Switching power supplies, in contrast, rectify the AC voltage directly and use rapidly switched MOSFETs and capacitors to step down the DC voltages. The switching rate is typically near 50 kHz. The output voltages of a switching power supply are intended to float, and are not well referenced to ground as with a linear power supply, i.e. the common output at 0 V is really a 5 V square wave at 30kHz.

Our analysis of the problem is this: there is nothing inherently wrong with switching power supplies as long as care is taken to isolate the supply voltages from ground. If, however, the isolation is done poorly, the lab ground can become seriously contaminated with high frequency noise. Since the main advantages of switching power supplies are reduced cost and weight, the tradeoff does not favor their use in lab electronics.

Laser stabilization

During the construction of our laser table, a diploma student in BEC I, Peter Zarth, was constructing a similar laser table for use with potassium. Rather than use the typical scheme for saturation absorbtion spectroscopy for referencing the laser to the atomic line, Peter constructed a frequency modulated (FM) scheme. His success convinced us to try the fm scheme on our lithium laser table. Our success has further convinced both BEC I and BEC II to switch their lithium spectroscopy as well. Peter's thesis provides some details on the implementation of fm spectroscopy [194].

Saturated absorbtion spectroscopy is a well-understood technique for extracting a narrow atomic feature from a severely Doppler broadened sample. In a hot ($\sim 100°$ C) vapor cell, the spread in atomic velocity causes the cell to scatter a near-resonant "probe" laser over a line-width determined by the temperature of the cell (~ 1 GHz) rather than the shape of the underlying atomic transition, which typically is much narrower (~ 10 MHz). The narrow spectral features can be recovered if the atoms of a particular velocity class have their transition saturated by a strong "pump" beam, sent counter propagating to the probe beam. The absorbtion of the probe beam will be the same except when the beam is resonant with the saturated atoms. Then, the absorbtion of the probe beam will be reduced as the two beams "compete" to excite the same atoms. The width of features in a saturated scheme are determined by the line-shape of an individual atom rather than the hot ensemble.

Saturated absorbtion spectroscopy provides a minimum when a resonance condition is satisfied by the pump and probe beams. However, locking to a minimum is inconvenient. How, for example, do you tell which way the frequency is drifting or when the "minimum" has been reached? The differentiation of the signal is accomplished by introducing some sort of frequency modulation, thereby sampling a small region near the center frequency. The frequency modulation is detected in the probe beam and interpreted as the derivative at the center frequency through lock-in detection. In the typical saturated absorbtion spectroscopy scheme, the frequency modulation is applied to the pump beam by an AOM modulated at ~ 20 kHz. In the FM scheme, the frequency modulation is applied to the probe beam by an EOM driven at ~ 20 MHz. For the FM scheme, the derivative is more "non-local", but, due to its high frequency, provides a higher signal to noise ratio.

The FM spectroscopy scheme is visible in the upper left hand corner of Figure 2-19. Approximately 2 mW of light from the master laser is frequency shifted and delivered by optical fiber to the lock region where it is divided roughly evenly into pump and probe beams. The probe beam has sidebands at 20 MHz added (the frequency modulation) before being sent, counter-propagating to and overlapping with the pump beam, through a lithium vapor cell [177]. The probe beam is then detected on a fast photodiode (Thorlabs part number PDA10A).

The signal detected on the photodiode depends on the relative phase and intensity of the sidebands on the probe beam. When the laser falls on the photodiode,the sidebands interfere, modulating the laser intensity at the sideband frequency. The amplitude of the in-phase component of the modulation can be interpreted as the derivative of the absorbtion line. The phase is detected by a home built lock-in amplifier described in Ref [58] and used to provide an error signal to a PID controller (Toptica PID110).

Extracting a good signal from the fm spectroscopy lock has proved difficult. Eliminating electronic noise from the system by (1) grounding one plate of the EOM to the optics table, (2) separating the rf amplifier from the detection electronics, (3) adjusting the length of cable in the detection electronics, (4) shaping the pump and probe beam with an optical fiber, and (5) filtering higher harmonics from the photodiode signal have all helped to improve the error signal. In the end, we are able to lock the laser for long periods of time. The quality of the lock will be determined when we have ultracold lithium atoms to diagnose the laser line-width.

2.3.3 Large bias-field generation

One immediate requirement for future work in BEC III is control over the atom-atom interactions. As has been shown in recent years, the easiest way to control atom-atom interactions is by adjusting the magnetic bias field to raise the energy of a bound molecu-

	Bias (G/A)	Gradient (G/cm/A)	Curvature (G/cm^2/A)
Curvature Coils	3.00	0.50	0.86
Anti-Bias Coils	3.05	1.46	-0.081
MOT Coils	3.82	1.23	0.40

Table 2.3: Fields, gradients, and curvatures generated by the main chamber magnetic trap.

lar state near threshold. Two atoms colliding at near zero velocity are resonant with the molecular state. The presence of this "Feshbach resonance" strongly influences the scattering, and hence, the strength of inter-atomic interactions. Experiments have shown useful Feshbach resonances for Na-Na scattering at 907 G [78], for Li-Li at 822 G [39], and for Na-Li 746, 760, and 796 G [179].

Ultimately, we anticipate that the majority of future experiments will be performed in the science chamber where new coils can be designed and installed for the sole purpose of generating kilogauss fields. In the mean time, this work could be performed in the main chamber. In this section, we discuss how the main chamber magnetic trap might generate these magnetic fields with little modification.

Fields from the magnetic trap

Helmholtz coils are a pair of co-axial current carrying loops of radius R which are separated by a distance R. When the current is run in the same direction in both loops ("Helmholtz" configuration), the on-axis field halfway between the loops is uniform, having no gradient or curvature. When the currents are run in the opposite directions ("anti-Helmholtz" configuration), the gradient is uniform, having no bias field or curvature. Spacing the loops closer (further) than R retains the behavior of the on-axis central bias-field and gradient in either configuration, but adds a positive (negative) curvature to the field in Helmholtz configuration. Pictures and schematics of the Science Chamber magnetic trap in Figure 2-5, show 3 pairs of co-axial coils in near Helmholtz configuration: the curvature coils, the anti-bias coils, and the MOT (quadrupole) coils. In reality, the coils, with average radius 26 mm, 63 mm, and 46 mm, are spaced at 69 mm, 39 mm, and 67 mm respectively such that none of them will provide a curvature-free bias field. The bias-fields and curvatures provided by these coils in Helmholtz wiring and the gradients provided in anti-Helmholtz configuration are given in Table 2.3.

These coils are currently wired as shown in Figure 2-5. In this configuration, the curvature and anti-bias coils combine to provide (nearly) bias-free curvature by being wired in Helmholtz configuration, but it the opposite direction from each other so that the bias fields cancel out. If the wiring of the trap were re-configured such that current could be provided to either the curvature coils or the anti-bias coils, running ~ 300 A in either pair

would produce a bias field near 1000 G with a curvature of ~ 250 G/cm^2 or $\sim$-25 G/cm^2. The second would be preferable for working with lithium atoms in the ground state [195]. As an alternative, a zero curvature bias field of 1000 G can be generated by running current in the curvature and the anti-bias coils in a ratio of $\sim 1 : 10$, such that the curvature is canceled. A similar current of ~ 300 A would be required.

Thermal management of coils

The wire comprising the magnetic trap is low resistance, ~ 2.5 mΩ/m, however, because of the lengths involved with winding the coils (~ 5 m) and the high currents necessary to generate tight confinement (~ 100 A), significant power is dissipated (~ 200 W). This power is dissipated by a stream of water constantly circulated through the coils. During evaporation, the circulating water is warmed by about $3°$ C from an initial temperature of $\sim 20°$C. Because the Feshbach fields require currents approximately 3 times larger, the power dissipated will increase by an order of magnitude, as will the rise in water temperature. We anticipate a final water temperature near $50°$ C when 300 A is run through either the curvature or anti-bias coils.

It is unfortunate that this puts us within a factor of 2 of catastrophic coil failure (when the circulating water boils), even more-so given the crude nature of the temperature measurements. Care must be taken when first raising the current to ensure that the heat load does not overwhelm the system. In the event that sufficient field cannot be achieved with a single set of coils, it would be possible to split the current amongst all three sets of coils (curvature, anti-bias, and MOT). Because the field scales linearly with current, but the power dissipated scales with the square of the current, this operation should be failsafe. With 100 A running in each coil, we obtain a total bias field of ~ 1000 G and a curvature of ~ 100 G/cm^2. The positive curvature would need compensation when working with ground state lithium atoms, e.g. by optical dipole forces.

Precision control of bias fields

Because atomic properties vary so strongly with magnetic field near the Feshbach resonance, it is crucial that the magnetic field be stable and reproducible. A stabilization scheme described in Ref [37] was implemented first in BEC II [24] and later in BEC I. The scheme is this: a power supply run in voltage control mode will provide an arbitrary current depending on the resistance presented. The current is controlled by an IGBT operating in the regime of linear resistance. A PID controller maintains the current through the coil (as measured by a hall probe) at the desired set point by changing the resistance of the IGBT.

Finally, it is useful to maintain the bulk of the bias field with a single set of coils and provide tuning with a second coil set. This is simple for us to accomplish by re-wiring the
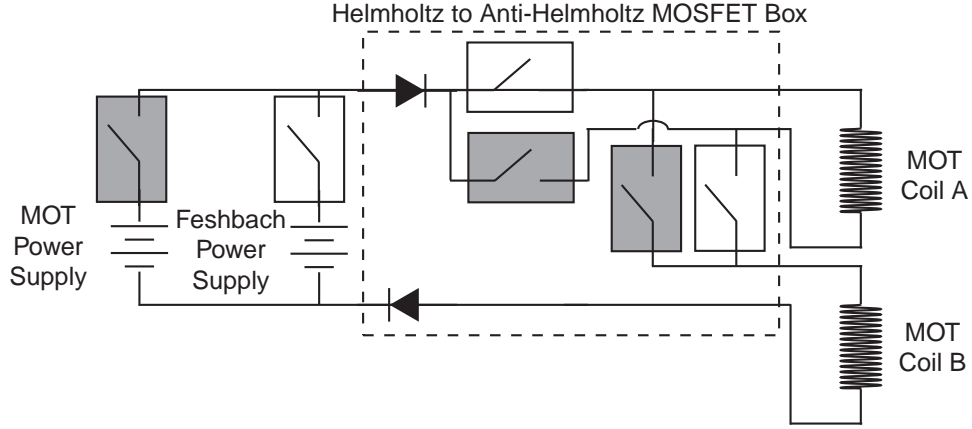
Figure 2-20: Schematic of MOT control box. MOSFET switches, boxed in either grey or white are to be switched simultaneously. For the MOT fields, the coils run in anti-Helmholtz configuration. For Feshbach tuning fields, the coils run in Helmholtz. TTL controls for the box are not shown.

MOT coils to run in Helmholtz as opposed to anti-Helmholtz configuration. A schematic for the control box is shown in Figure 2-20.

The proposed wiring of the magnetic trap, shown in Figure 2-21 integrating these control schemes. The major electronic components have been assembled, but at the time of this writing, not installed in the apparatus.
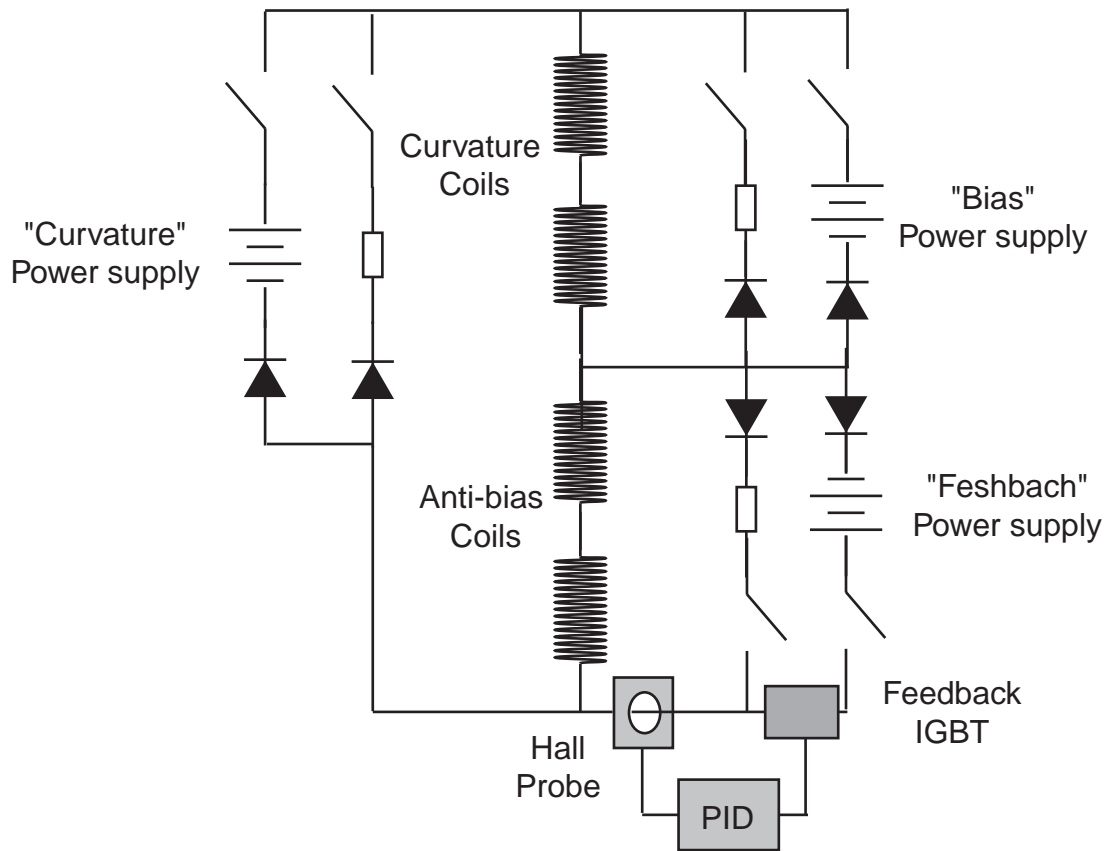
Figure 2-21: The proposed wiring configuration for the magnetic trap includes additional power supplies and control IGBTs to allow the production of 1 kG bias fields. In parallel to each power supply is the associated "de-bounce" circuit. The "curvature" and "bias" power supplies are labeled according to lab terminology for clarity.

Chapter 3

Quantum Reflection Theory

Mechanics is concerned with the propagation of particles subject to forces or external potentials. Newton's first and second laws are sufficient to describe classical motion: (1) in the absence of a force, a particle will continue in its motion indefinitely, and (2) when subject to a force an object will accelerate at a rate proportional to the force and inversely proportional to the mass. In terms of potentials, an object with kinetic energy E (at zero potential energy) is confined to regions of potential less than or equal to E. Points where the potential energy is equal to E are known as the classical turning points, as shown in Figure 3-1. In an elastic collision, an object approaching a classical turning point is observed to slow as kinetic energy is converted to potential energy, then to reverse direction and accelerate away from the turning point as the potential energy is released. This process is known as reflection. Reflection may be gradual, as in the case of a ball reversing its motion at the top of its arc, or pronounced, as in the case of a ball bouncing off of a hard wall.

Reflection is also associated with the propagation of excitations, either electromagnetic waves, such as light from a mirror, or matter waves, like sound or ocean waves. As these excitations propagate through a medium, they do so without significant motion of the medium in the direction of propagation, eg. sound is not carried by individual atoms in the air. The character of the propagation, i.e. the speed, dispersion, etc. depend on the character of the medium, e.g. light travels faster in a vacuum than through a piece of glass. We require that the excitation satisfy a continuity equation at all points, so when the medium changes, the details of the excitation must change as well. Whenever an excitation meets the boundary of a medium, the excitation can be entirely or partially reflected. The classic example is a beam of light propagating through partially silvered mirror; light divided at the interface into a transmitted beam and a reflected beam.

Quantum mechanics is concerned with the propagation of quantum mechanical wavefunctions subject to external potentials. Because a matter wavefunction exhibits both wave and particle properties, we expect that the process of reflection in quantum mechanics may
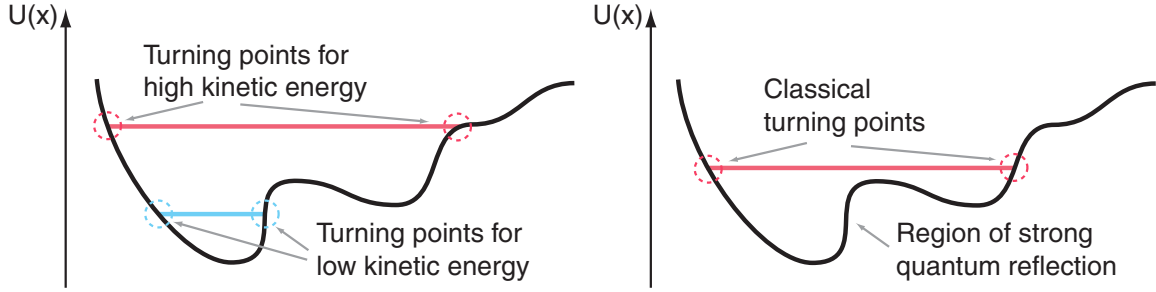
Figure 3-1: Classical turning points confine a classical object to a region of space. The position of a classical turning point depends on the kinetic energy of the object, as shown in the left panel. Regions of strong quantum reflection, shown on the right, exist where the potential changes abruptly relative to the kinetic energy and the de Broglie wavelength of the particle.

show characteristics of both Newtonian reflection and of excitation reflection. This is indeed the case. Quantum mechanical reflection is similar to Newtonian reflection because it involves the propagation of matter, not an excitation. Further, it is easily shown that the behavior of wavefunctions at classical turning points is is the same as the behavior of a classical particle. However, the quantum treatment of propagation resembles mathematically the propagation of excitations, and the wavefunction can become divided via partial reflection when the propagation medium, that is, the potential, changes sharply, as shown in Figure 3-1. Specifically, the quantum treatment reveals the partial reflection of a particle wavefunction without the presence of a classical turning point, a phenomenon called quantum reflection.

This chapter addresses the theoretical treatment of reflection of cold (quantum) atoms from surfaces and reviews the current state of research on the reflecting of atoms from surfaces. I will begin with the most basic treatment of quantum mechanical reflection and progress rapidly to an "experimentalist's" view of quantum reflection from a real solid surface. Along the way, I will touch on some the subtler points of current quantum reflection theory.

3.1 Quantum scattering from a 1-D potential

The general question we wish to address is: "How does a spatially isolated potential affect a freely propagating particle wavefunction?" Answers to this question can be used to determine the scattering properties of atoms, the decay of radioactive particles, and the bulk interactions between atoms in a gas in addition to the reflection properties of surfaces. According to J. J. Sakurai, "it is impossible to overemphasize the importance of this topic" [150]. The one-dimensional case is the simplest, free from considerations of angular

momentum.

Quantum reflection can be understood by starting with a canonical first year quantum mechanics problem and generalizing to the semi-classical propagation of wavefunctions. As quantum reflection represents the breakdown of classical behavior, we will see that quantum reflection occurs when the semi-classical approximation fails [30, 110, 22, 120, 55, 114, 29, 56].

3.1.1 Barrier scattering

The canonical freshman quantum mechanics problem involves the scattering of a particle from a one dimensional barrier of height V [36]. In this case, the potential is fixed and solutions to the Schrödinger equation

$$\left(-\frac{\hbar^2}{2m}\nabla^2 + V\right)\Psi = \imath\hbar\frac{\partial\Psi}{\partial\,t} \qquad (3.1)$$

take on the particularly simple form of a stationary state multiplied by a phase factor $\Psi(\mathbf{r},t) = \psi(\mathbf{r})e^{-\imath\,Et/\hbar}$. The time-dependence can be eliminated and the result is the time independent Schrödinger equation

$$\left(-\frac{\hbar^2}{2m}\nabla^2 + V\right)\psi = E\psi \qquad (3.2)$$

Solutions to the time independent Schrödinger equation take the form of plane waves of wavevector k, with $k^2 = 2m(E - V)/\hbar^2$ where m is the particle mass and $\hbar$ is Planck's constant, h, divided by 2π. In the event that $V > E$, the wavevector is imaginary and, instead of a plane wave, the solution is exponential decay or growth.

In the simplest barrier scattering case, a particle is incident on an infinitely sharp step to a classically forbidden region. We consider 3 wavevectors in our solution, the forward and backward propagating wavevectors (k and $-k$)in the classically allowed region and the exponentially damped wavevector ($-\imath k$) in the classically forbidden region. The step represents a classical turning point and the solution of the Schrödinger equation reveals that the amplitude of the reflected wave is equal to the amplitude of the incoming wave, just as we expect classically (see Figure 3-2).

Suppose the particle is assumed to approach the infinitely sharp potential step with sufficient kinetic energy to be classically allowed in either half space (see Figure 3-2). On either side of the boundary, the wavefunction takes the form of a traveling wave. At the boundary, the potential changes abruptly and to satisfy the requirements that the wavefunction and its first derivative be continuous, we include a third traveling wave. This reflected component has the opposite wavevector of the incident component. The reflection
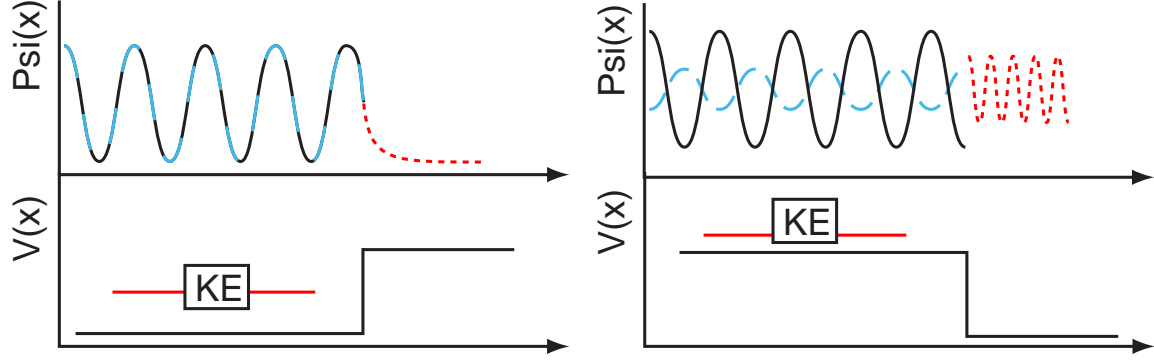
Figure 3-2: Left panel: The quantum mechanical treatment of a potential barrier reproduces the classical behavior if the barrier height exceeds the kinetic energy of the particle. The incoming particle (black solid) will penetrate the barrier slightly (red dotted), but the reflected amplitude (blue dashed) is equal to the incoming amplitude.
Right panel: The quantum mechanical treatment of a potential step reproduces the classical behavior of accelerating or decelerating the particle, but introduces the novel behavior of dividing the wavefunction into transmitted (red dotted) and reflected (blue dashed) components. This behavior is more akin to the splitting of an excitation at a medium boundary and a direct consequence of the wave nature of matter. We interpret the partial reflection as a probability of the particle being reflected from the potential step.

and transmission probability are easily found as

$$R = \left|\frac{B}{A}\right|^2 = \left(\frac{1 - k'/k}{1 + k'/k}\right)^2 = \left(\frac{k - k'}{k + k'}\right)^2 \tag{3.3}$$

$$T = \left|\frac{C}{A}\right|^2 = \left(\frac{2}{1 + k'/k}\right)^2 \left(\frac{k'}{k}\right) = \frac{4kk'}{(k + k')^2} \tag{3.4}$$

where k (k') is the wavevector in the region of space where the potential equals zero (V). The partial reflection of the wavefunction may be interpreted as the probability that the incoming particle was reflected.

Of particular interest is that Equation 3.3 applies to both a positive potential step of amplitude $V < E$ and a negative potential step (potential drop). Neither of these is a classical turning point. Unlike the mechanical reflection due to insufficient energy to penetrate a barrier, the partial reflection of the wavefunction at a step or drop is interpreted as a demonstration of the wave nature of matter. In the limit of a large step, $k \gg k'$ and the probability of reflection goes to unity. This general feature of quantum reflection is preserved in the generalization to an arbitrary barrier.

3.1.2 Threshold behavior

Briefly, we remark that the sophisticated theoretical apparatus we are about to construct is not necessary to understand the threshold behavior of quantum reflection. The expressions R and T in Equation 3.3 can be expanded for small values of $k \propto \sqrt{E}$. The results, $R \simeq 1 - 4k/k'$ and $T \simeq 4k/k'$ show that as the incident wavevector falls to zero, the reflection probability approaches unity as $1 - \sqrt{E}$ with a proportionality constant determined by k', which depends on the details of the potential barrier [101, 22].

3.1.3 Numeric solutions for quantum reflection

In general, the 1D scattering problem is not analytic. The sharp barrier is simple because the time independent Schrödinger equation can be solved exactly at all points in space and the free coefficients matched at the discontinuity. However, when the scattering potential is continuous, this strategy becomes intractable for most potentials[1]. An alternative is to assume that the wavefunction has a particular form at one point in space and use the Schrödinger equation to develop the wavefunction spatially. For a potential confined to a region a $-a < x < a$, and a particle incident from the right (that is, from $+\infty$), with sufficient energy to propagate in the region $-\infty < x < -a$ will couple to two states after interaction: a transmitted state propagating toward $-\infty$ and a reflected state propagating toward $+\infty$. By beginning in the region $-\infty < x < -a$ with a forward traveling wave, propagating the solution through the region $-a < x < a$, and, finally, decomposing the solution in the region $a < x < \infty$ into forward traveling and backward traveling waves, the reflection probability can be calculated numerically for a given incident energy. An example of the propagated wavefunction in a $1/r^4$ potential is shown in Figure 3-3.

This is the approach, described at length in Christian Sanner's Diploma thesis [151] and in Ref. [55, 114], that we will use to calculate the reflection probability for the Casimir-Polder potential.

3.1.4 The badlands function

There is an alternative, analytic technique for understanding semi-quantitatively quantum reflection from an arbitrary potential. The WKB or semi-classical approximation of the propagating wavefunction takes the form:

$$\psi_{\text{WKB}}(x) = \frac{1}{\sqrt{p(x)}} e^{\pm \frac{i}{\hbar} \int p(x)dx} \tag{3.5}$$

---

[1]Although, interestingly, the function $-sech(x)^2$ has an analytic solution.
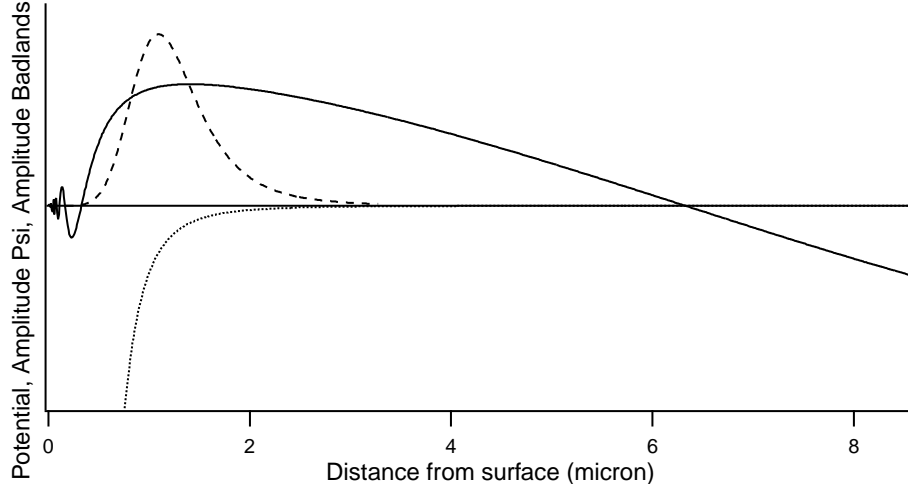
Figure 3-3: The solution to the Schrödinger equation (solid line) for a $1/r^4$ potential (dotted line) and the amplitude of the associated badlands function (dashed line) are the diagnostics for quantum reflection, as described in the text.

where $p(x) = \sqrt{2m(E - V(x))}$ is the momentum of a mass m particle with energy E traveling in a potential $V(x)$ [15, 62]. This wavefunction is a good approximation of the true wavefunction $\psi(x)$ when the energy of the particle need not be treated quantum mechanically, i.e. where the kinetic energy is large and the particle wavelength is small relative to changes in the potential. If this is not the case, we expect that the WKB approximation will fail and quantum behavior will become relevant.

The second derivative of ψ_{WKB} differs from the Schrödinger equation by a term $B(x)p(x)^2\psi_{\text{WKB}}$ where $B(x)$ is the badlands function given by

$$B(x) = \frac{1}{p(x)^2}\left[\frac{3p'(x)^2}{4p(x)^2} - \frac{p''(x)}{2p(x)}\right] \tag{3.6}$$

which must be small for the WKB approximation to remain valid [55]. Wherever this term grows large, we find that the semiclassical treatment is poor. Figure 3-3 shows the the badlands for the a sample $1/r^4$ potential.

For the purposes of quantum reflection, we will consider the point where the badlands function is a maximum to be the point where reflection occurs and the magnitude of that maximum to be an indication of the reflection probability. The form of the badlands function indicates that this point will occur when there is change in potential, through p' and p'', which is large relative to the local momentum of the particle. Both terms tend to grow

68

large at the same point and the essential physics is retained by focusing only the first term:

$$\lambda(x) = \frac{p(x)'}{p(x)^2} = \frac{mV'(x)}{p(x)^3} \ll 1 \tag{3.7}$$

which has a maximum when $V'(x)^2/V''(x) = p(x)^2/3m$. The situation where $\lambda' = 1$ corresponds to the particle wavelength, λ, increasing by λ (a factor of 2) over a distance of λ and the breakdown of the WKB approximation.

By plugging the expression for the maximum of λ' back into the Schrödinger equation, we arrive at an expression relating V to E. Here we find that the maximum value for the failure occurs when $V(x) = -\frac{2(\alpha+1)}{\alpha-2}E$ when the potential takes the form $V(x) = -C_\alpha/x^\alpha$. This expression suggests that quantum reflection will not occur when $\alpha < 2$, that is, for potentials which do not fall off faster than $1/r^2$. Bearing in mind that quantum reflection does not really occur at a single point, this expression can also be used to determine the "point" of reflection, $r_\circ \simeq (C_\alpha/E)^{1/\alpha}$. The value for λ' can be evaluated at this point; the result will in general depend on the incident energy as $C_\alpha^{-1/\alpha}E^{-1/\alpha}$. Thus, higher reflection probabilities are associated with lower incident energy and smaller C_α coefficients.

It is curious that weaker potentials with smaller C_α will exhibit greater quantum reflection; for the sharp step, quantum reflection from a smaller potential drop is smaller. Why doesn't the power law potential behave like the sharp step? The difficulty with power law potentials is that they have no characteristic length scale. However, because reflection is strongest when the magnitude of the potential is roughly equal to the particle's initial kinetic energy, there is a length scale associated with the particle energy. For a given kinetic energy, this length scale is shorter for a weaker potential, that is, the magnitude of the potential reaches the initial kinetic energy closer to the origin. As any inverse power law potential falls to $-\infty$ at the origin, the weaker potential appears "sharper" due to the shorter length scale, and hence exhibits strong quantum reflection.

3.2 Reflection of cold atoms from a solid surface

The interaction between a classical atom and a solid surface is inelastic scattering. When the atom reaches the short-range repulsive potential of the surface, it interacts with the many degrees of freedom in the surface where it may gain or lose energy. If the atom loses energy, it may not have sufficient energy to escape the attraction of the van der Waals attraction and is adsorbed on the surface in a bound state. If the surface is sufficiently warm, the atom will eventually be ejected from the surface [101, 22]. Evidence for this behavior, which predicts that classical atoms will reach thermal equilibrium with confining surfaces, is as close as the radiator or refrigerator; both devices rely on the thermalization of surfaces and gases. Quantum reflection subverts this behavior by suppressing the overlap
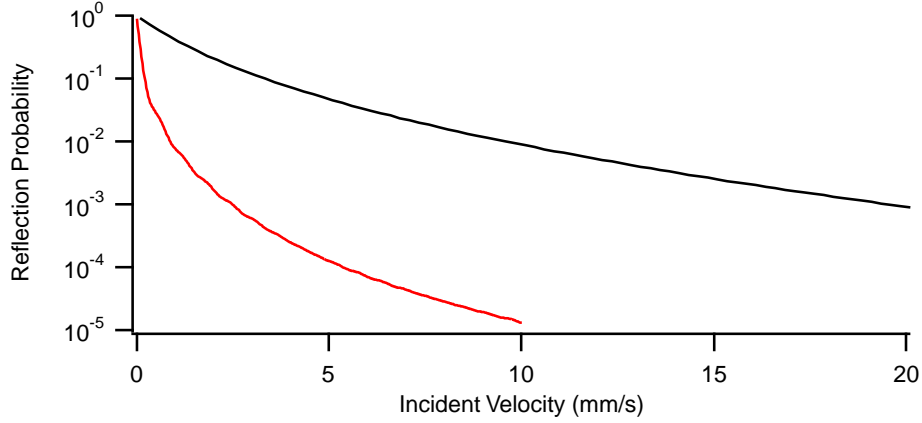
Figure 3-4: Numerically calculated reflection probability for sodium incident on the pure Casimir-Polder potential of a silicon surface (upper curve) and the un-retarded van der Waals potential of a silicon surface (lower curve). The range of velocities plotted extends from ~ 1 nK to ~ 1 μK.

of the incoming atomic wavefunction and the bound states of the atom-surface potential.

Having provided a general framework for understanding quantum reflection, we turn our attention to the specific case of atoms incident on the Casimir-Polder potential of a solid surface. As discussed in Chapter 1 Section 5, the dominant interaction between a neutral atom and a solid surface is the fluctuating dipole-dipole interaction. This potential is long-range attractive and takes the form $V_{\text{C--P}} = -C_4/r^4$. In the following calculations use $C_4 = C_4^{\text{Si}} = 6.2 \times 10^{-56}$ Jm^4, calculated in Ref [192]. Our use of the purely retarded form of the atom-surface potential is justified a posteriori by the observation that the point of reflection as defined by the badlands function resides entirely in the region $r > c/\omega_0$ and $r < \lambda_{\text{T}}$, as discussed in Section 1.2.

Using the techniques discussed above, we can analyze the atom surface interaction to see when we anticipate significant reflection of an incoming atomic wavefunction. First, using the analysis of the badlands function, we find that reflection of atoms at 10 nK (~ 3 mm/s) occurs approximately 1 μm away from the surface, while reflection of atoms at 1 muK (~ 30 mm/s) occurs at roughly 0.25 μm, well into the region where the region where the potential is well approximated by the pure Casimir-Polder potential [55]. Second, using the full numeric treatment [165, 151], we calculate a reflection probability that approaches unity as the velocity approaches zero, shown in Figure 3-4. This figure also shows the reflection probability from the potential $V_{\text{vdW}} = -C_3/r^3$, with $C_3 = 6.9 \times 10^{-49}$ as the van der Waals coefficient[2].

[2]This value is $C_4/(\frac{2}{3}\pi^2\lambda)$, where $\lambda = 589$ nm is the wavelength of sodium [55].

The effect of resonances

In the previous section, the quantum treatment of the atom-surface potential focused on the long-range attractive tail and ignored the short-range repulsive potential and the bound states it hosts; only in the classical treatment of the atom-surface interaction did the bound surface states come into the discussion. However, it is possible for a surface excitation to resonantly connect an unbound state to a bound state. Resonances play a major role in determining scattering behavior, as was discussed in Section 2.3.3.

A more sophisticated treatment of quantum reflection uses a potential which can support the bound states into which non-quantum reflected atoms can become adsorbed [30, 120, 29]. What happens if one of these bound states is close to zero energy? The solid surface itself has numerous degrees of freedom, and a correspondingly high density of low-energy states which could connect an incident atom to a deeply bound state. What role does the internal structure of the surface play in quantum reflection? An excellent discussion of these problems, and of reflection processes in general is presented in Ref. [120]. The general result is: when an isolated resonance exists at threshold, either a bound state with zero energy or a bound state connected by a surface mode, it will play a role in reducing the reflection probability. However, this case is exceedingly rare, and typically the many resonances near threshold couple the incoming atomic state to the rapidly decohering internal states of the surface leading to no net effect, and quantum reflection proceeds without concern for resonant adsorbtion.

Chapter 4

Normal Incidence Quantum Reflection

This chapter supplements work reported in the following publication, included in Appendix B:

- T. A. Pasquini, Y. Shin, C. Sanner, M. Saba, A. Schirotzek, D. E. Pritchard, and W. Ketterle, *"Quantum reflection form a solid surface at normal incidence"*, PRL **93**, 223201 (2004).

The quantum interactions between atoms and surfaces has become increasingly important in recent years; atom chips confine BEC within a few μm of surfaces [130, 50, 146, 47], atom-surface interactions are being used to place limits on short-range Yukawa potentials [70], material diffraction gratings are an important component in precision interferometry experiments [134, 135], and a growing field of atom optics searches for novel devices to manipulate and control ultracold atoms [144, 143, 51, 52]. Finally, quantum reflection, as discussed in Chapter 3, is one of the most basic and beautiful demonstrations of the wave nature of matter and the power of nano-kelvin temperatures to uncover fundamental physics.

This Chapter contains a review of previous experiments studying quantum reflection and details of the first observation of normal incidence quantum reflection with alkali atoms. The major result is the observation of $1 - \sqrt{E}$, threshold dependence of the reflection probability at normal incidence for atoms with velocity from 1-10 mm/s. Further, atoms were held in a trap divided in half by a solid surface.

4.1 Previous work on quantum reflection

The only requirements to observe quantum reflection are a population of atoms with well controlled atomic velocity and a detector sensitive to the reflected fraction. However, be-

cause reflection drops off so quickly with increasing incident energy, quantum reflection has been studied primarily in two settings: (1) the scattering of helium and hydrogen off of liquid helium surfaces, and (2) with atomic beams incident on surfaces at grazing incidence. The first scenario is favorable because of the anomalously weak interactions of liquid helium and the availability of cryogenically cooled hydrogen and helium. The second scenario uses the small transverse velocity of a collimated atomic beam to decrease incident energy while maintaining high atom flux.

For the interaction of helium or hydrogen atoms on liquid helium, specular reflection can be observed at temperatures below a few K; threshold quantum reflection, which displays the appropriate $\sqrt{E}$ scaling occurs at temperatures below 100 mK. Some experiments involve generating a pulsed effusive beam of helium by localized heating and then detecting the pulse as it travels either directly to a bolometer or is specularly reflected off a helium surface [46, 122]. Other experiments pre-trap and cool a population of hydrogen atoms before allowing one wall of the trap to be replaced by a liquid helium surface; the resulting atom loss rate can be used as a measure of the reflectivity of the helium [41, 193]. Extensive theoretical work [44, 45, 18] and experimental efforts [122, 191] on the helium-liquid helium interaction have helped to clarify the initial work of Ref. [46]. Similar work was done with hydrogen incident on liquid helium surfaces, first at high energy where threshold quantum reflection behavior was not observed [14, 13] and later in the threshold regime [41, 73, 193]. Of particular note is the work of Ref. [13] where, working in a regime where the sticking probability varied linearly with energy [14], hydrogen was focused by a concave liquid He surface. Theoretical work with liquid He is complicated, however, by the presence of riplon modes in the liquid surface and by the fact that, being a liquid, the "surface" of liquid He is poorly defined.

The second class of quantum reflection experiments, grazing incidence thermal beams on solid surfaces, has received more attention in recent years. In a typical experiment, a highly collimated beam of thermal atoms impinges on a surface at angles of 80°-90°, such that the velocity normal to the surface is a tenth to a thousandth of the beam velocity [2, 165, 67, 42, 126]. Such experiments are ideally suited for studying quantum reflection as the incident velocity can be easily varied over orders of magnitude and, due to the high flux of atoms, the reflection probability can be accurately measured down to the 10^{-6} level where quantum reflection occurs in the non-retarded region of the potential [42].

Grazing incidence experiments also allow the study of a wide range of surfaces, including micro and nano-structured surfaces which demonstrate enhanced reflectivity. In Ref. [166], silicon surfaces were etched to create a series of parallel ridges which were oriented perpendicular to the incident beam. The surface showed a greatly enhanced reflection. One interesting side effect of periodically structured surfaces is the introduction of a wavevector

k_{surf} parallel to the transverse wavevector of the atomic beam. Instead of pure specular reflection, atoms may also diffract from the surface, gaining or losing k_{surf}, thereby increasing or decreasing the reflection angle relative to the incident angle. This effect was used to demonstrate an interferometric "hologram" with quantum reflection [167].

A simple model to explain the enhanced quantum reflection due to structured surfaces is an effective reduction in the C_3 and C_4 coefficients which reduces the strength of the reflection potential, as discussed in Section 3.1.4. A more detailed analysis of the reflection from ridged surfaces suggests that other physics is involved, namely, Fresnel diffraction of the atomic beam [125, 95] [1]. In this theory, the diffraction orders from the ridges will add constructively to create the specularly reflected beam. There is little dependence on the details of the atom-surface potential and the model is in good agreement with the observations for grazing incidence beams.

Some experiments and theoretical models with evanescent waves have explored atom-surface interactions and quantum reflection. Aspect's group found effects of the attractive van der Waals potential when studying reflection from a repulsive evanescent wave optical potential at normal incidence [97], an effect discussed at length in . references [163, 33]. In an interesting modification to the typical blue-detuned (repulsive) evanescent wave mirror, reference [72] discusses quantum reflection from a purely attractive red-detuned evanescent wave. In related work, reflection from the periodic potential of blue-detuned 1D optical lattice was studied in the context of quantum reflection [54].

4.2   History of quantum reflection experiments at MIT

Quantum reflection experiments have a history at MIT[2]. The first observations of quantum reflection were made in the early 1990's by Tom Greytek and Dan Kleppner by measuring the sticking probability[3] of evaporatively cooled hydrogen on films of liquid helium [193]. An earlier work by the same group, Ref. [41], was in the appropriate regime to observe quantum reflection, but failed due to an insufficient coating of highly reflective liquid helium on the poorly reflecting sinter surface [73]. These studies led to a resurgence in theoretical treatments of quantum sticking near threshold which have generally converged to the accepted picture presented in Chapter 3.

When the first result of threshold quantum reflection from solid surfaces were reported

---

[1]A similar analysis may be performed by considering reflection as occurring due to the rapid, repeated measurement of the atom wavefunction on the outside of the grating. This Zeno effect analysis of quantum reflection is useful for approximating the reflection, but does not contain some of the essential physics [94].

[2]There are interesting parallels between the history of quantum reflection experiments at MIT and "family tree of atomic physicists" that was widely publicized when the Nobel Prize in 2001 was shared by Carl Wieman, Eric Cornell and Wolfgang Ketterle [88, 32]. One notable difference is the major contributions made to the field with atomic beam quantum reflection by F. Shimizu who has no connection to the "tree".

[3]The sticking probability being the compliment of the reflection probability, S=1-R.
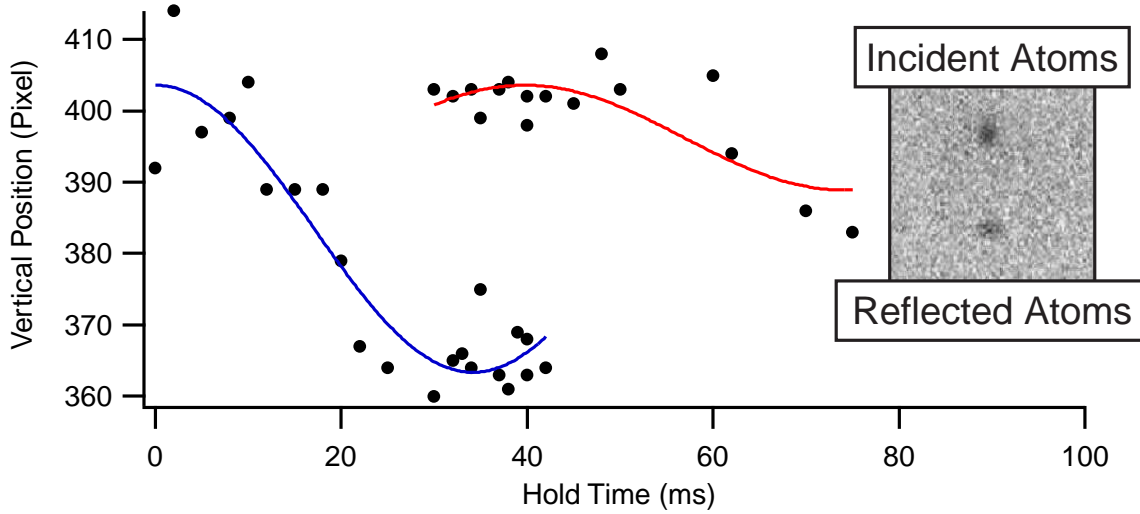
Figure 4-1: The first signature of normal incidence quantum reflection. For times between 30 and 45 ms, the positions of the centers of the two condensate blobs are given. The inset shows the image for 32 ms. **This figure will be updated**

by F. Shimizu in 2001 [165], the Ketterle group at MIT became interested in achieving unity reflection of ultracold atoms from solid surfaces. The hope was that trapped BEC had such well controlled velocity that quantum reflection could be observed at normal incidence and could possibly be useful for manipulating and even confining ultracold atoms. The first round of experiments loaded into the science chamber included a modest piece of glass, mounted at 45° above the surface of the first atom chip. The experiment involved loading atoms into the tweezers, translating to the science chamber and pushing the tweezers into the glass slide. Quantum reflection would be observed as atoms being ejected perpendicular to the trap due to the small trap depth. Unfortunately, no signal was observed. The negative result was attributed to the velocity of atoms within the condensate was dominating the center of mass velocity when the collision was induced.

I arrived at MIT in the fall of 2002 when a new quantum reflection experiment was being mounted. The single coil trap had been designed by Dave Kielpinski as a way of reducing the speed of sound[4]. Later that year, the single coil trap was installed in the science chamber ~ 1 cm below a plano-concave lens. The concave side was intended for use as a novel trap in which quantum non-sticking would both support the atoms against gravity and confine them radially, the flat side of the lens faced down and was intended for a conventional study of normal incidence quantum reflection. Atoms were to be pushed upward into the surface and reflect downward; the signature of reflection would be a sudden vertical shift in the position of the atoms in time of flight, indicating they were moving downward, not

---

[4]Dave left the group before any result could be obtained with the trap.
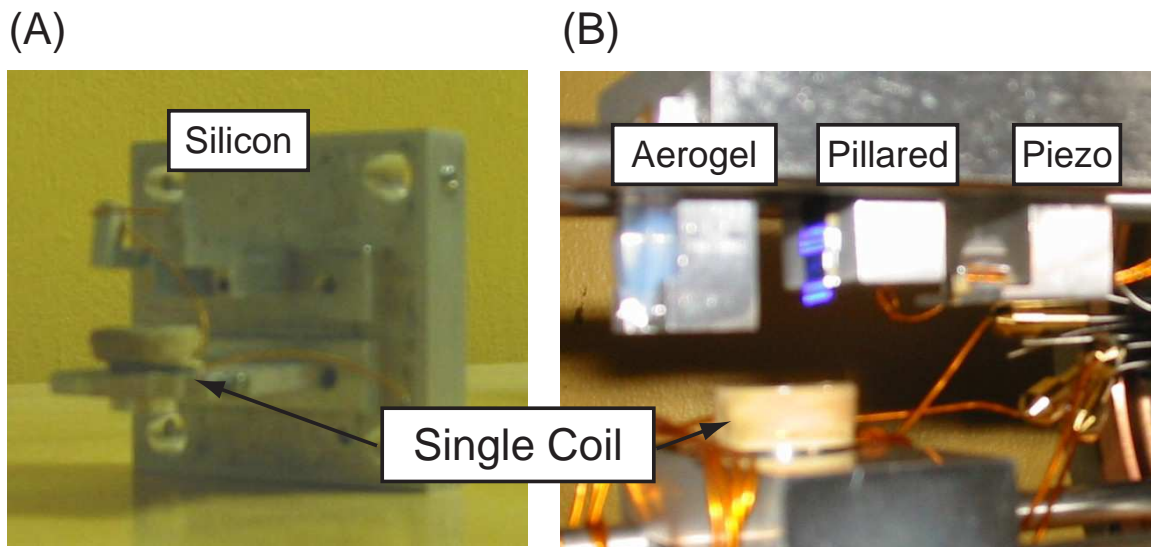
Figure 4-2: Pictures of the (now retired) experimental setups for studying quantum reflection. The silicon substrate is missing in the left panel due to damage.

upward when the trap was turned off. We were able to observe the signature of quantum reflection as shown in Figure 4-1, but moved on to other projects immediately afterward; characterization of quantum reflection along this axis was difficult. Instead, we used the single coil to produce world record low temperatures [49, 99].

Encouraged by our preliminary result and hoping to capitalize on the very low horizontal trap frequencies of the single coil, we designed a new set up in which a thin silicon substrate was mounted above the single coil with its face parallel to the vertical axis, as shown in Figure 4-2a. The success of this setup is described below. As a result of this work, a small number of groups have developed numerical simulations of quantum reflection [162, 105] to help explain the role that interactions and collective excitations play in the reflection of condensates.

As we were developing our work on normal incidence quantum reflection, Shimizu expanded on his original experiment by introducing structure to the surface, thereby modifying the reflection potential and greatly enhancing the reflection probability [166, 167]. In our next project on quantum reflection, we introduced several dilute surfaces into the science chamber, shown in Figure 4-2b. The aerogel with a mass density of 2% of glass and the nano-structured surface with mass density 1% of solid silicon were both expected to show greatly enhanced reflection. The silicon surface from the first experiment was mounted on a piezoelectric element so that its position could be rapidly varied in time, hopefully averaging (and weakening) the potential of the surface. The successes (and failures) of this experiment are also discussed below.
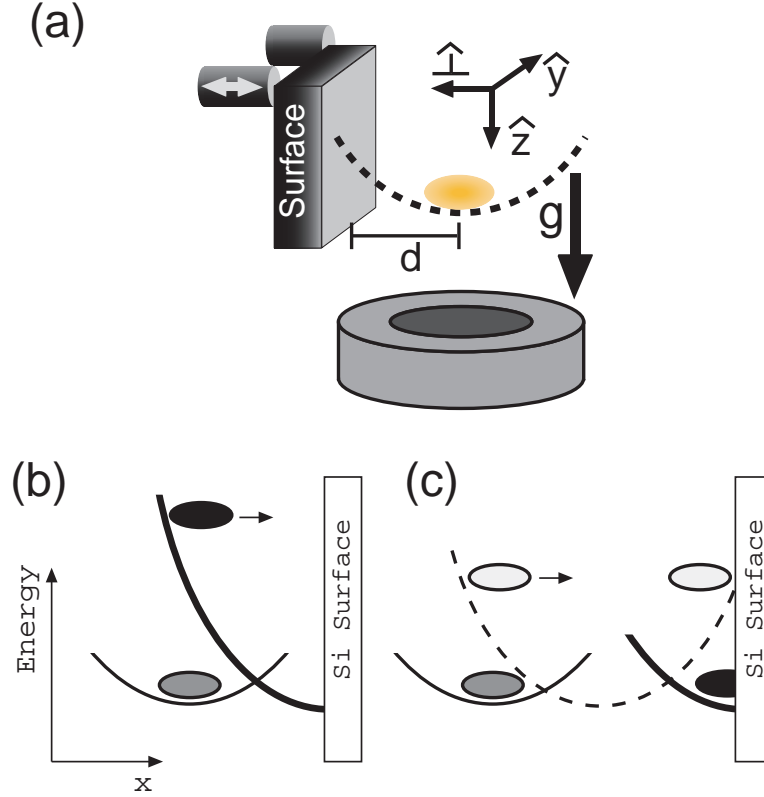
Figure 4-3: Panel (a) illustrates how atoms are confined near a solid surface above the single coil. Panel (b) and (c) illustrate the experimental techniques for studying quantum reflection. Atoms initially confined a distance d from the surface undergo a dipole oscillation when the trap center is shifted to the surface, as shown in (b). Atoms are loaded into the surface trap by shifting the trap position halfway to the surface, allowing the dipole oscillation to carry the atoms to the surface, then shifting the trap to confine the zero velocity atoms against the surface, as shown in (c).

The ultimate limitations to quantum reflection with BEC, as discussed in Chapter 6 suggested further studies on the reflection of condensates. By the time the second project wrapped up, however, we had decided to switch gears with the experiment. There are no plans to continue research on quantum reflection at this point.

4.3 Reflection at normal incidence

Observing quantum reflection with nano-kelvin temperature trapped atoms is fundamentally different than previous work with atomic beams. On the plus side, there is no need to work at grazing incidence as the mean velocity of atoms at 1 nK is less than 1 mm/s; the incident velocity must actually be increased by some other, easily controlled means, such as

a center of mass oscillation. On the other hand nano-kelvin atoms cannot yet be produced continuously [27] or in large quantities, so experiments must be pulsed and are limited to reflection coefficients greater than $\sim 1\%$ unless extreme measures are taken in detection. Furthermore, at low temperature and large number, atom clouds tend to be quite extended, so care must be taken in preparing the sample far from the surface[5].

A picture of the experimental setup is shown in Figure 4-2, and an experimental schematic is shown in Figure 4-3. Bose-Einstein condensates of $\sim 5 \times 10^5$ ^{23}Na atoms are prepared in the usual fashion (see Chapter 2) and transferred into the potential mini-mum of a single coil trap (see Section 2.2). Approximately 1 cm above the coil, a $\sim 1 \times 1$ cm sample of the surface to be studied was mounted. Condensates were positioned ~ 200 μm away from the bottom edge of the face of the surface. Velocity perpendicular to the surface was generated by shifting the trap minimum to be centered on the front face of the surface by applying a bias field $B_\perp$ (see Section 2.2.2). By changing the initial position of the trap relative to the surface, velocities between 0.5 mm/s and 25 mm/s were achieved. We attempted to use an actuator to move the surface into the stationary BEC, but could not control the velocity sufficiently well (see Section 2.1.7).

Reflection probabilities are calculated as the ratio of atoms reflected from the surface to atoms incident on the surface, making quantitative measurements quite simple; because the absolute number is unimportant, we can be a little careless in calibrating the imaging light. Atoms were released from the trap and, when possible, the surface was removed from the imaging field. A pulse of light resonant with the $F = 1 \rightarrow F' = 2$ transition was applied to the atoms for 1 ms to pump atoms in the $|F = 1\rangle$ state into the $|F = 2\rangle$ state. Because of the high optical density of atoms in the incident cloud, after optical pumping, the atoms were allowed to expand with their acquired photon recoil momentum for 2 ms. The cloud was then imaged on the $F = 2 \rightarrow F' = 3$ cycling transition.

Also of interest were excitations that might occur during quantum reflection of Bose-Einstein condensates. For observing excitations, imaging was done with low intensity light on the $F = 1 \rightarrow F' = 2$ to obtain undistorted images.

4.4   Experimental results

The published experimental results of our work are included in Appendix B.

---

[5]Actually, "surface evaporation" [107, 69] helps to maintain the low temperature of the BEC after the excitations from loading and decompressing the single coil trap have dissipated.
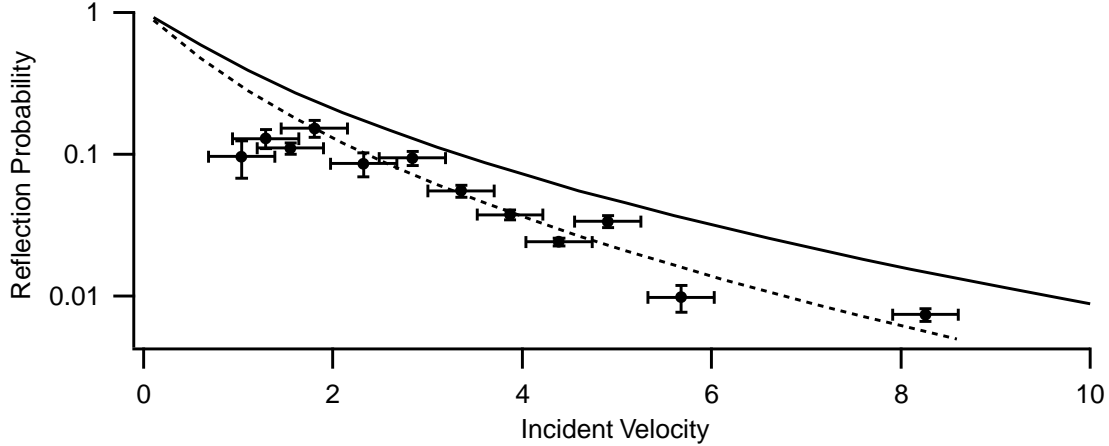
Figure 4-4: The reflection probability vs. incident velocity for sodium atoms reflecting off a solid silicon surface. Theory curves are described in the text.

4.4.1 Reflection probability

Figure 4-4 is the major result of Ref. [133]. Vertical error bars show the standard deviation of six measurements and horizontal error bars show the uncertainty in the initial velocity. The solid curve is the same as in Figure 3-4, the numerically calculated reflection probability for sodium on solid silicon. Two "interesting" features caught our attention: the data are better fit by increasing the C_4 coefficient by a factor of two and the lowest velocity data do not show threshold behavior, but rather saturate near 10%. Unraveling these mysteries was the subject of our second experiment with quantum reflection and, incidentally, the subject of the following two Chapters.

4.4.2 Quantum reflection surface trap

One of our original motivations for studying quantum reflection was for its potential use in trapping atoms [86, 193]. In the limit of zero incident velocity, a quantum reflecting surface could be used to construct a physical container for BEC. Atoms were transferred into a harmonic trap centered on a surface so that confinement in one dimension was provided by a solid silicon surface, as described in Figure 4-3 and Ref. [133].

If the surface were perfectly absorbing, we would expect the atom number to fall to zero within a half trap period, corresponding to ~ 50 ms for the compressed trap and ~ 150 ms for the decompressed trap. That atoms remain in the trap beyond this time indicates that quantum reflection enhances the trap lifetime. The lifetime measurement in Figure 4-5, in conjunction with a crude model for reflection suppressed trap loss, gave a "zero-velocity" reflection probability of between 50 and 70%.

Figure 4-5: Lifetime measurements for atoms confined in the surface trap. Solid (open) circles show the remaining atom fraction for a $2\pi \times (9, 9, 6.5)$ Hz $[2\pi \times (3.3, 2.5, 6.5)$ Hz] trap. The fitted $1/e$ lifetimes are 23 ms and 170 ms respectively.
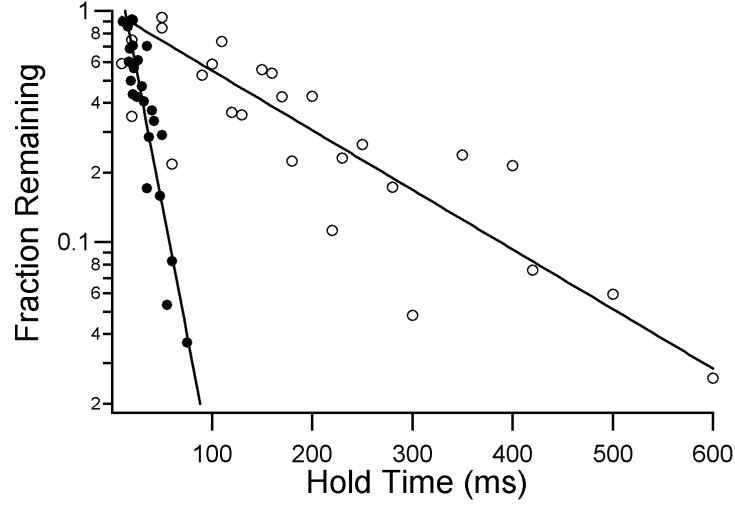
When the solid surface was replaced with the pillared surface, we did not observe a dramatic increase in the lifetime as expected.

Chapter 5

Structured Potentials for Quantum Reflection

This chapter supplements work reported in the following publication, included in Appendix C:

- T. A. Pasquini, M. Saba, G. -B. Jo, Y. Shin, D. E. Pritchard, and W. Ketterle, *"Low-velocity quantum reflection of Bose-Einstein condensates"*, PRL **97**, 093201 (2006).

Initial results from normal incidence quantum reflection on silicon were limited to $\sim 15\%$ at the lowest velocities as opposed to a predicted values near 50%. We had two goals with our second quantum reflection project: (1) improving the reflection coefficient and (2) understanding the limitations at low velocity. This Chapter will address our work on the first of these two goals.

As discussed in Section 3.2, the reflection probability depends only on the incident velocity and the properties of the surface, specifically, the C_4 coefficient[1]. *Ab initio* calculations of the C_4 coefficient are difficult, requiring precise knowledge of the frequency dependent terms in the atomic polarizability and the dielectric function of the wall, but has been done for many alkali species on a range of conducting and dielectric surfaces [175, 192, 91, 112, 38, 111, 55]. The resulting values for C_4 vary only by factors of ~ 2 from the perfect conductor to a strong insulator like glass [175, 165], so, apart from exceptional cases like liquid He, changing the reflecting material will have only minor effects.

On the other hand, C_4 is also approximately proportional to the density of atoms in the bulk material [118], a fact which can be exploited by microfabrication [166], metal foams [8] or silica aerogels [154, 48, 77]. For these surfaces, the atom-surface interaction is reduced; lower density means fewer surface atoms to attract the incident atom. This was

---

[1]For the work presented here, C_4 alone is sufficient to characterize the potential as the reflection occurs deep in the retarded tail of the atom-surface potential.

the approach favored by Shimizu, whose work with structured surfaces [166, 167] guided our efforts in improving the reflection coefficient.

In recent years, experiments and theory have addressed the question of how periodic structuring of surfaces influence quantum reflection. Tailored surfaces achieved through micro- and nano-fabrication have blurred the line between the interaction of atoms with bulk materials and the interaction of atomic waves with periodic structures. Specifically, the interpretation of the results of grazing incidence quantum reflection on grating surface [166, 125, 95, 94] have been analyzed with reference to the properties of the surface only as a correction term. Normal incidence quantum reflection from structured surfaces provides the complimentary limiting case to grazing incidence quantum reflection. Furthermore, adapting normal incidence reflection to large angles would be possible. The studies presented here show that, at normal incidence, a simple "reduced density" approach suffices [118] to describe quantum reflection.

This Chapter contains details of the Science Chamber's published work on improving quantum reflection probabilities by structuring surfaces. We report an enhancement of the reflection probability by a factor of 4-5 at a velocity of 1 mm/s. Discrepancies from the predicted behavior for sodium atoms on silicon are explained as resulting from adatoms on the surface. The published work is augmented by extended discussions of techniques for computing the relevant atom-surface potentials for structured surfaces.

5.1 Candidates for improved reflection

Because low-velocity quantum reflection occurs approximately 1 μm away from the surface, improving the reflection properties requires reducing the density of the surface in the upper ~ 1 μm. The following are the candidate surfaces for improving normal incidence reflection.

5.1.1 Silica aerogels

Silica aerogels push the low-density limit of bulk solids. Formed by controlled evaporation of a suspension of silica strands with densities in the range of 0.5% to 50% of bulk silica [154, 53]. There is no regular internal structure apart from a distribution of pore sizes which has been studied extensively [77, 48]. Above some typical length scale, ξ_0, aerogels appear homogeneous. Below a second length scale, a, the gels properties are determined by the surfaces of the silica clusters that comprise the aerogel. This makes them useful as a technique for introducing impurities for studies of ^{3}He [140, 68].

We obtained samples of aerogel manufactured to a bulk density of $\sim 2\%$ from Norbert Mulders at the University of Delaware, the same source for the aerogels of Ref. [140]. In Ref. [140] aerogels were characterized by $\xi_0 \cong 50$ nm and $a \cong 3$ nm. A photograph of the

Figure 5-1: One of the silica aerogels (outlined in red) used in the quantum reflection experiment in its aluminum holder. The slight blue color is due to Rayleigh scattering.

sample is shown in Figure 5-1. This density was the lowest achievable if the gel was to have a "flat" surface when removed from the growing container. Because any underlying structure in the aerogel is characterized by length scales below $\xi_0 \ll 1$ μm, this material should be well approximated by reducing the effective C_4 coefficient by a factor of ~ 50, as described below in Section 5.2.

5.1.2 Periodically pillared surfaces

Interference lithography is a process by which the interference pattern of two overlapped laser fields is transferred to a solid structure [173, 155, 153, 185, 152]. The much heralded Nanoruler, produced by interference lithography, has potential uses in semiconductor patterning and replication in addition to filling the role of a diffraction grating in telescopes [92]. By introducing two perpendicular interference patterns, the techniques for creating grating structures can be used to create arrays of pillars on surfaces. The surface selected for our experiment with quantum reflection was such a pillar structure etched into single-crystal silicon, shown in Figure 5-2.

As opposed to the aerogel, the periodically pillared surface was quite thin (~ 1 μm) and supported by a thick substrate of silicon at crystalline density. We anticipated that, because quantum reflection occurs a micron away from the surface, the bulk substrate would play only a small role in determining the reflection properties of the surface, and that the surface would be well approximated by an effective C_4 coefficient of $0.01 \times$ C_4^{Si}. However, we were concerned that, because the size of structures on the surface was comparable to the reflection distance that the potential, a bulk material approximation might not be appropriate, as described below in Section 5.2.
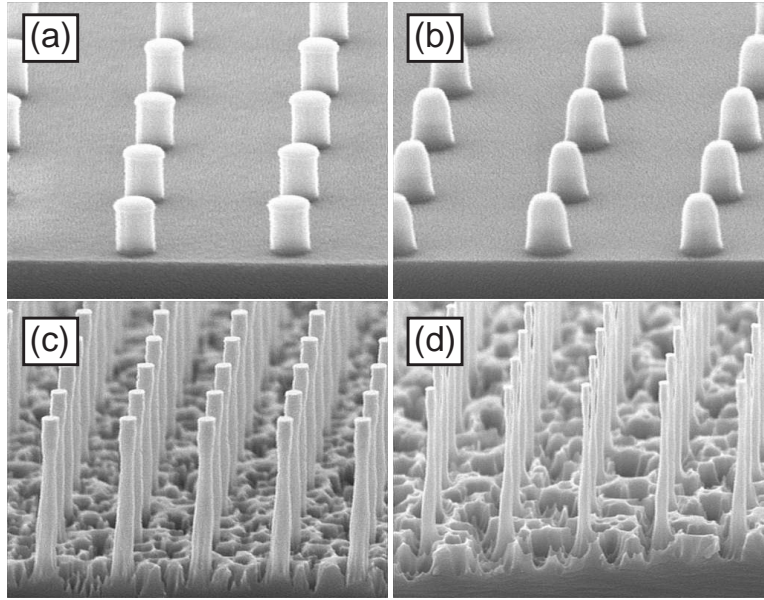
Figure 5-2: A multi-step etching process is used to create the periodically pillared surface. In the first step, a photoresist is annealed by the interference fringes of a 2D optical lattice above the surface. The pillars are spaced at 500 nm. The surface is then etched, leaving the array of pillars shown in panel (a). Repeated applications of etchant gradually remove material from the sides of the pillars and the bulk material below, shown in panels (b)-(d). In panel (d), the pillars are ~ 1 μm tall and approximately 50 nm in diameter.

5.1.3   Laser ablated surfaces

A surface that balances the structure-less nature of the aerogel with an etching process that removes material in the top ~ 1 μm of a bulk surface is the femptosecond laser ablated surface made by Eric Mazur at Harvard University [164]. The process involves the irradiation of a silicon surface submerged in water, creating a molten layer of silicon that rapidly cools in a "ripple" pattern. As this process is repeated thousands of times, the various ripples interfere, leaving behind pillars with a height of ~ 500 nm spaced at ~ 500 nm. Unlike the periodically spaced pillars, however, these ablated surfaces do not have a periodic structure. After an application of HF, the pillars have a diameter of roughly 200 nm, giving a density reduction of approximately 90%. It appears possible that a second stage of oxidation and HF etching could result in a reduced pillar diameter.

This surface was not available when we began our work on reduced density quantum reflection, but would make an interesting comparison to the periodically pillared surface.

5.1.4   Carbon films

A third technique for reducing the atom-surface interaction does not vary the density at all, but instead uses an extremely thin film. Section 1.2.2 arrived at the density dependence of C_4 through a volume integral over the surface to a depth comparable to the quantum reflection distance. If the surface is thinner than this distance, the interaction can be substantially reduced. In fact, the actual form of the potential is changed; the potential for a t thick film can be calculated as the difference between the potential of two semi infinite slabs separated by t. As t becomes very small, the $-C_4/r^4$ form of the potential becomes $\approx -C_5/r^5$ [120]. Going from bulk to a film 1 nm thick, the temperature for 90% quantum reflection is increased by about a factor of 100.

We selected a carbon film with 2.5 nm thickness (Goodfellow part number C 004905). Thinner films are available, but, according to the manufacturer, would be difficult to mount with significant unsupported area. As it turns out, we were unable to mount even this film owing to the fact that, once it was separated from the substrate in water, none of us could see it to mount it on anything. We did not attempt to work with thicker carbon films as the enhancement factor becomes less than a factor of 2 for a 10 nm thick surface.

5.1.5   Piezo-modulated silicon

Our final technique for reducing the atom-surface interaction was to temporally modulate the position of the surface. Because the atoms in the experiment move with such low velocity (mm/s) and the reflection process takes so long (10 ms), we thought it would be possible to reduce the effect of the surface by having it moved out of its "reflecting" position

for the majority of the time. As long as the modulation was much faster than the atoms propagation, the atoms should respond to the time-averaged potential, as is the case in the TOP trap [137]. Piezoelectric elements can be modulated at 10 kHz, significantly faster than the inverse reflection time of 100 Hz.

We selected a 2 mm pizeo cube which could be changed in length by ~ 2 μm with the application of 100 V. To the front side, we mounted a small silicon wafer with vacuum compatible epoxy. The assembly is visible in Figure 4-2. Once mounted, we found the maximum amplitude of motion could only be reached at frequencies near 1 kHz, so, we chose to modulate with a sine wave rather than a square wave. This resulted in an effective halving of the atom-surface potential. Since the reflection probability scales with the fourth root of the C_4 coefficient, however, we were unable to detect any change in the reflection probability with this technique.

5.2   What potential does an atom see?

Our most successful experiment with reduced density surfaces used the array of nano-pillars. We observed, as is discussed below, an enhancement of the low velocity reflection probability by a factor of 4 to 5. However, in order to match our observations with theory, we needed to understand the interaction between the pillared structure and the atoms. The naive assumption, that the reduction in density can be averaged and the C_4 constant reduced proportionally, breaks down when atoms can "see" the structure during reflection.

We create three models for generating the reflection probability: (1) the "average density" approach makes the assumption that an appropriate reduction of C_4 is sufficient to describe the structuring, (2) the "average potential" approach uses a spatial average of the full 3D potential of a structured surface, and (3) the "average reflection" approach uses a spatial average of the reflection probabilities calculated from different points above the full 3D potential. In the end, we find that all three models provide similar results in the experimentally accessible regime for the surface used in our experiments, and so the average density approach is sufficient in the nano-kelvin regime.

This section discusses the various numerical techniques employed to calculate the atom-surface interaction for a surface with structures of comparable size to the atomic wavelength. Furthermore, we discuss the role that surface adatoms play in reducing the reflection probability.

5.2.1   Models of the pillared surface

The pillared surface comprises a wafer of single crystal silicon with a ~ 1 μm thick overlayer of 50 nm diameter pillars spaced in a square array with side 500 nm, as pictured in Figure 5-

2. In each model, silicon substrate is included as a semi-infinite slab of silicon which provides a potential $V_{\text{bulk}}(z) = -C_4/(z + 1\mu m)^4$, although we find that the inclusion of this potential has negligible effect on the reflection probability in the experimentally relevant region. The pillars, while somewhat irregularly shaped, are assumed to be cylindrically symmetric. All calculations are strongly motivated by the "source theory" of Ref. [118] and a presentation made at the 2005 CAMS conference by J. Babb [10]. Source theory approaches the calculation of the Casimir type forces between dielectrics without explicit reference to the zero-point-field energy.

The average density approximation

The simple average density approximation is attractive for its intuitiveness: a reasonable expression for the atom-surface interaction can be built up from atom-atom interactions and an appropriate density [118] or, on the other hand, can be derived by starting with the surface-surface interaction and diluting the surface down to a single atom [6]. However, such a simple picture misses certain aspects of a bulk material: the source theory Milonni and Shih [118] overestimates the interaction between an atom and a metal surface by $\sim$ 15% [10]. Furthermore, when dealing with a "real" surface, the dielectric function has typically been measured for bulk materials only and small structures may exhibit different frequency dependent behavior [20, 131]. Nevertheless, when the structure of the surface is mesoscopic, it is reasonable to assume that the material behaves as the bulk.

Also supporting the use of an average density to simulate the surface is the large de-Broglie wavelength, $\lambda_{dB} \simeq 1\ \mu m$, which exceeds the spacing of the pillars. This is a major difference from grazing incidence reflection where the deBroglie wavelength parallel to the surface is quite small [166, 95, 94].

By scaling the C_4 coefficient for silicon down by a factor of 100, we anticipate improved reflection as shown in Figure 5-4 with a dotted line. The original reflection probability calculation for silicon is shown as a solid line.

The average potential approximation

A more sophisticated treatment of a structured surface would generate an atom-surface potential with structure at length scales comparable to the scale of the structure. For our periodic array of nano-pillars, we expect a Casimir-Polder type potential modulated with some "egg-crate" function at distances less than $\sim 1\ \mu m$ from the surface. The potential will be stronger directly above a pillar, would be substantially modulated at distances comparable to the pillar spacing and strongly modulated at distances comparable to the pillar size. Because the pillar spacing is 500 nm and we expect reflection to occur near $1\ \mu m$, this structure may be relevant.

To generate the full 3D potential of the structured surface, we first calculated the potential above a single pillar by integrating the atom-atom interaction over the region containing matter. This integrated potential, with the limits taken to infinity, was scaled to match the Casimir-Polder potential. With the potential of a single pillar, the full potential at a point above the surface was "built up" by summing the contributions from all pillars within range of the point. The relevant lines of Mathematica code are included in Appendix D.

The average potential was calculated by spatially averaging the potential. Twenty-one points inside $1/8^{th}$ of a unit cell (the region bounded by 4 neighboring pillars) were chosen and appropriately weighted to give an average potential at atom-surface separations from $0.1 - 7$ μm above the pillared surface, that is, in the relevant region. The potentials calculated by the average potential and the average density approximation are shown in Figure 5-3.

The two potentials are indistinguishable ($< 5\%$ difference) above 5 μm from the surface, but differ by a factor of 2 at 300 nm from the surface. Additionally, the pillar potential appears softer, "turning on" $\sim 10\%$ further away from the surface. This is because at a distance $a > r > r_{\text{pillar}}$, the pillar radius, from the surface with pillars spaced at a, roughly r^2/a^2 of the incident atoms are strongly interacting with the full density silicon in the pillar. Other atoms see the effect of the surface "turning off" gradually. This is why at distances beyond a micron the average potential matches the reduced density potential, but the two potentials diverge at short range. When $r < r_{\text{pillar}}$, the fraction of atoms still interacting strongly with the pillars is roughly r_{pillar}^2/a^2, and we again expect the average potential to be close to the reduced density potential. We could not numerically check this limit due to computing power constraints.

The average potential was fit with a polynomial expression and the reflection probability was calculated from this polynomial fit. The reflection probability for the average potential model is shown in Figure 5-4 with a dashed line. The observed softening of the potential does not significantly affect the predicted reflection from the average potential, which is almost identical to that from the average density surface.

The average reflection approximation

The final technique for calculating the reflection probability from the structured surface uses the numerically calculated line potentials to calculate the reflection probability before spatially averaging. This model relies on an Eikonal approximation, i.e. we assume that the particle travels along a line perpendicular to the surface and ignore any initial parallel velocity or parallel accelerations induced by the modulation of the atom-surface potential. Again, twenty-one points were selected and the potential calculated above these points. A fitting polynomial was generated for each, shown in Figure 5-3.
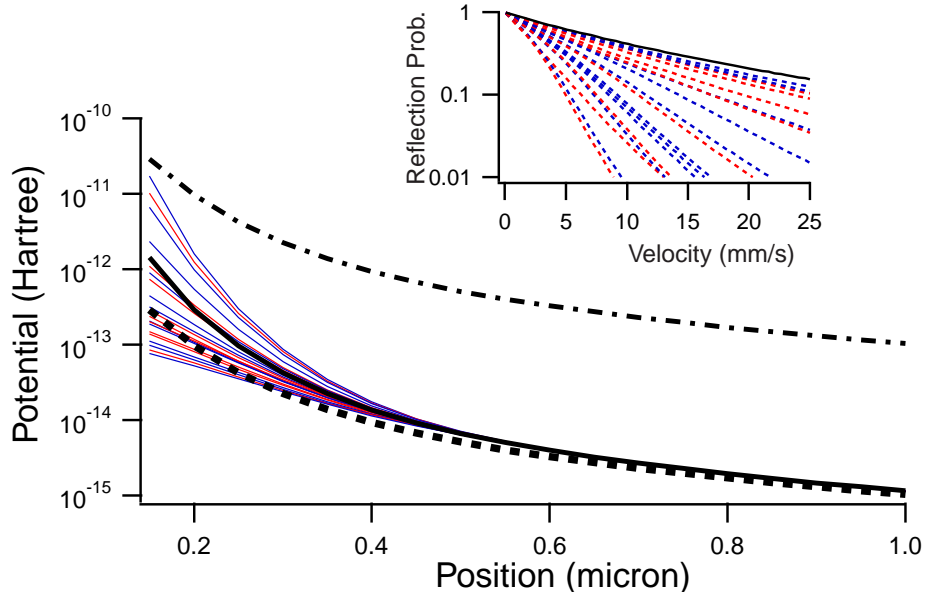
Figure 5-3: Line potentials (multiple red and blue lines), calculated as described in the text, above various points on the pillared surface show strong dependence on the structure of the surface. The reflection probability for each line potential is shown in the inset. The spatial average of these potentials (thick, black line) is used to calculate reflection probability in the "average potential" model. The "average density" model (thick, dotted black line) is indistinguishable from the other models at distances greater than a few microns. Finally, the purely retarded potential of a solid surface is shown (thick dash-dotted black line). Inset: The reflection probability is calculated from each of the line potentials (dotted lines). The solid line is the prediction of the average density model.

The general trend is that stronger potentials are measured above points close to a pillar. While we were unable to accurately calculate the potential closer than ~ 100 nm from the surface, the potential just above the pillar (the uppermost thin line) appears to converge to the purely retarded potential of a *solid* silicon surface, shown as a thick dot-dashed line, as expected.

The reflection calculated from each of these line potentials varied substantially in magnitude and velocity dependence, shown by the dotted lines in the inset of Figure 5-3. The trend is for higher reflection probability to be observed for line potentials close to the pillar, but at no point is the reflection as strong as for the reduced density approximation, shown as the black solid line. At worst, in between the pillars, the reflection probability is worse than for the solid silicon surface above 10 mm/s. The softening of the potential discussed in the previous Section has become crucial in this model; when the potential levels off away from the surface, the breakdown of the WKB approximation is no longer severe and atoms are smoothly accelerated into the surface.

The reflection probabilities for the line potentials were spatially averaged. The reflection
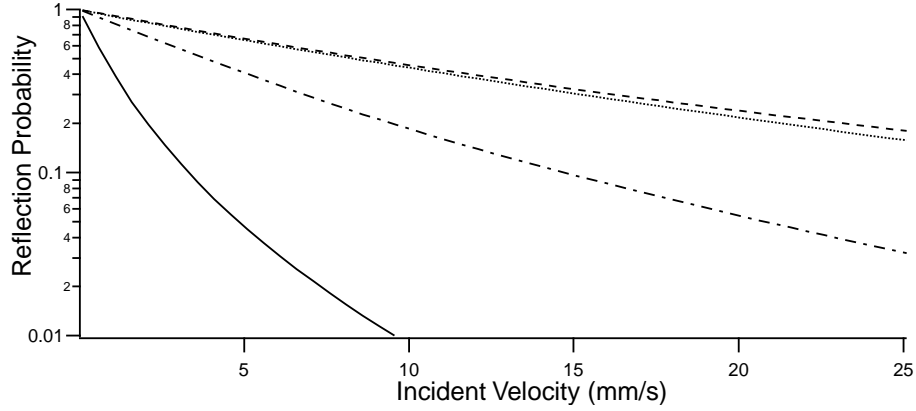
Figure 5-4: The predicted reflection probabilities are shown for four model potentials as described in the text. The solid, dotted, dashed and dot-dashed lines correspond to the (1) the solid silicon surface, (2) the average density model, (3) average potential model, and (4) average reflection model of the pillared surface.

probability for the average reflection model is shown in Figure 5-4 with a dot-dashed line. Unlike the average potential model, the average reflection model predicts a strong effect due to the structure of the surface. This model, however, does not account for the transverse coherence or transverse structure in the wavefunction, and is unlikely to give a good result for ultracold atoms with large λ_{dB}.

Comparison of models

The numerical techniques for calculating the reflection probability were compared for the limiting case of pillars spaces in a square array with spacing roughly equal to the diameter. This corresponds to the case of a solid surface. All three models predict the same behavior for the solid silicon surface as expected.

For the pillared surface, the three approximations predict enhancement of the reflection probability, shown in Figure 5-4. The average density and average potential model predict very similar results Only at higher velocity, around 70 mm/s do they differ by as much as a factor of 2; only when the badlands region pushes further in toward the surface, do the small differences in the two potentials become relevant. As such, we do not expect that our experiment will be able to distinguish between the these two approximations. By increasing the pillar separation, possibly by as little as a factor of 2, a repeated experiment would be able to distinguish between these models.

The average reflection model, however, predicts that the modulated potential will limit the enhancement of the reflection probability for surfaces with structures whose spacing is comparable to the point of reflection as predicted by the badlands region. A comparison

92

between two similar average density surfaces with different spacings, such as a pillared structure and an aerogel, would test the applicability of this model to the reflection of Bose-Einstein condensates.

5.2.2 Spurious interactions

Much ado has been made in recent years about the effect of conducting and insulating surfaces near Bose-Einstein condensates. Concern surrounds two major areas: the effect of stray oscillating fields (primarily rf fields) associated with Johnson noise [71, 100, 83, 69, 104, 145] and stray static fields associated with adsorbed atoms (adatoms) on surfaces [69, 113, 128]. Both effects are deleterious to precision measurements with BEC.

In conducting materials, Johnson noise is present due to the thermal motion of electrons which generates short range stray magnetic fields. Stray oscillating fields limit the lifetime of atoms in magnetic traps by coupling trappable states to un-trappable states, similar to the way forced evaporative cooling proceeds as discussed in Section 2.1.3. In contrast to rf cooling fields, stray rf fields are not spectrally narrow and affect all atoms in the trap, leading to an exponential decay of the trapped population. At distances beyond 100 μm, the losses due to the surface are minor compared to background scattering associated with our standard UHV conditions. Near a conducting surface, however, these effects can dominate, dropping the lifetime by several orders of magnitude [100, 83, 69, 104]. Theoretical treatments of the problem reveal that the skin depth of the material in question sets a length scale on which particularly large interactions can occur [71, 145].

For our quantum reflection experiments, the effect of Johnson noise is negligble; working with dielectric surfaces (which are poor conductors) as opposed to metal surfaces strongly suppress the effect of Johnson noise. In two experiments, background gas limited lifetimes were observed at distances down to 2.5 μm [69, 104]. Lin, et.al. measured an abrupt reduction in the trap lifetime from 3.5 s to $\sim$ 150 ms when a cold thermal cloud of atoms was brought to 1 μm away from a silicon surface, however, the effect was attributed to simple surface evaporation rather than fluctuating fields [104]. The theoretical treatment of a glass surface by Henkel, et.al finds that the spin flip loss rate due to Johnson noise is on the order of 10^{-18}s^{-1} at a distance of 1 μm from the surface, far below the observed background gas loss rate in our trap [71]. We therefore feel confident that Johnson noise plays an insignificant role in our system.

Adatoms exist on all surfaces. The classical interaction between atoms and surfaces leads to incident atoms landing in bound states of the van der Waals potential as discussed in Section 3.2. These adatoms comprise a fractional monolayer on the surface and could safely be ignored were it not for the fact that the electronic structure of atoms is altered in the presence of the surface [156]. The atom can be partially ionized, leading to an electronic

dipole on the surface. The degree of ionization can be approximated by comparing the ionization energy of the surface (work function) to the ionization energy of the atom. Since ionization energies are smallest for alkali atoms, the dominant contribution to the adatom field will be alkali adsorbates on the surface [113].

The static fields associated with these adatoms are more relevant for our quantum reflection work. Rather than affecting the lifetime of trapped atoms, these fields combine with the atom-surface potential to determine the reflection properties of the surface. For a uniform distribution of adatoms, the electric field would be zero above a large surface. In the case where the distribution of adatoms is localized, as might be the case if the adatoms were deposited primarily by slamming BECs against the surface, the electric field falls off with a power law dependence determined by the exact distribution of adatoms. The field of a localized point distribution would fall off as $1/r^3$, whereas a line of dipoles would fall off as $1/r^2$. A careful study of the adatom potential in reference [128] found that the electric field fell off with a power of -2 to -2.3.

The potential of this adatom field and the Casimir-Polder potential, therefore, have the same dependence on the atom surface separation; the electric field associated with adatoms was found to fall off as $1/r^2$ giving a potential $V_{\mathrm{adatom}} = -(\alpha/2)E_{\mathrm{adatom}}(r)^2 \propto C_{\mathrm{adatom}}/r^4$ [113]. This adatom potential would be indistinguishable from the atom-surface potential at large distances, and must be measured using alternative techniques [128]. Empirically, we find an upper bound on $C_{\mathrm{adatom}} \simeq C_4$ for our experiments with silicon surfaces [132].

Finally, we note that static patch charges will exhibit stronger interactions than an identical distribution of electric dipoles due to adatoms. A surface charge will create a uniform electric field, an a linear (point) distribution of patch charges creates an electric field that falls off as $1/r$ ($1/r^2$). The potential for the line distribution $V_{\mathrm{patch}} \propto C_{\mathrm{patch}}/r^2$, which, as discussed in Section 3.2 will not quantum reflect atoms at all. Strongly insulating surfaces which can support large patch charges without dissipation, like silica aerogels, will not display quantum reflection, and this is most likely the reason why we never observe quantum reflection from aerogels[2].

5.3 Experimental results

The published experimental results of our work are included in Appendix C.

---

[2]When we first became aware of this problem, we tried to establish the magnitude of the static charge on our aerogel surfaces. When removed from their mounts, the static charge was sufficient to firmly attach the aerogels worked with in this experiment to a gloved finger. Therefore, in addition to having stronger dependence on r, it seems that the magnitude of the static charge was also quite large.
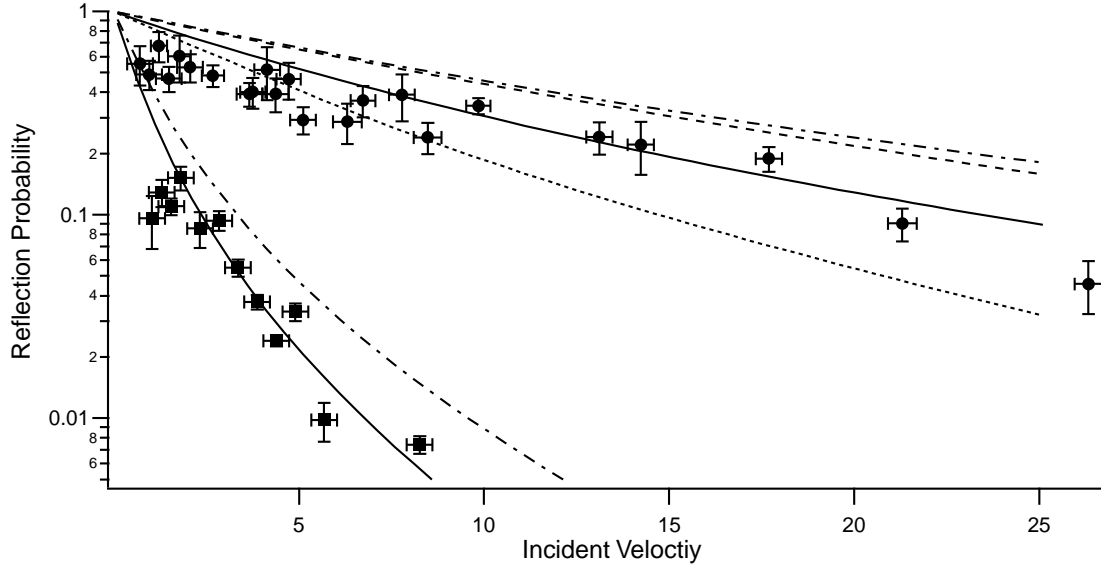
Figure 5-5: The reflection probability vs. incident velocity for atoms reflecting off solid and pillared silicon surfaces. All theory curves are described in the text.

5.3.1 Reflection probability

Figure 5-5 is the major result of Ref. [132], reproduced here to show how the models discussed above apply to our experiment. In addition to the data of Ref. [133] and Figure 4-4, data collected by the same technique but for the pillared surface pictured in Figure 5-2 are shown. To extend the experimental velocity from 0.5 mm/s to 25 mm/s, we used a loose trap with frequencies $2\pi \times (2.0, 2.5, 8.2)$ Hz and a tight trap with trap frequencies $2\pi \times (4.2, 5.0, 8.2)$ Hz. The data clearly show the enhanced reflection probability from the pillared silicon surface.

We present several theory curves generated by the models discussed in Section 5.2. First, the dot-dashed curves are the predictions for solid silicon and for the reduced density model. Both predict significantly higher reflection probability that we observe. The dashed and dotted curves show the predictions of the average potential and average reflection models respectively. The average reflection model predicts lower reflection than we observe at high velocity. Because there are no simple mechanisms for the model to underestimate the reflection probability of the surface, this suggests that the premise of the model, that atoms sample the potential in a very small range about their trajectory, is incorrect.

The solid curves use the same model as the dot-dashed curves, but have C_4 adjusted to fit the data at high velocity. This corresponds to roughly doubling the expected value of C_4. This is justified by the presence of sodium adatoms on the surface as discussed in Section 5.2.2 and corresponds to a stray field of 10 V/cm (70 V/cm) for the pillared (solid)

95

surface.

Still apparent in the enhanced reflection data is the deviation at the lowest velocities from the expected threshold behavior. This discrepancy is the topic of Chapter 6.

Chapter 6

Interaction Effects in Quantum Reflection

This chapter supplements work reported in the following publication, included in Appendix C:

- T. A. Pasquini, M. Saba, G. -B. Jo, Y. Shin, D. E. Pritchard, and W. Ketterle, *"Low-velocity quantum reflection of Bose-Einstein condensates"*, PRL **97**, 093201 (2006).

In our first experiment on quantum reflection, the three lowest velocity data points we collected showed a strong deviation from the anticipated behavior, as shown in Figure 5-5. Rather than rising to $\sim 50\%$ reflection probability as predicted, the data showed saturation near 10%. We initially attributed the effect to "collective excitations", "acceleration due to the harmonic trapping potential during the collision", and "mean-field interactions [via] the local speed of sound" [133]. In the end, all three of these play an important role in the details of reflection, but in a way that was difficult to understand at first. As we collected more data on reduced density surfaces, we also developed a more complete picture of quantum reflection of *condensates* as opposed to the well-developed theory quantum reflection of *atoms*.

This Chapter discusses BEC III's work in identifying and clarifying the role of mean-field interactions on quantum reflection of atoms from surfaces. Mean-field interactions are accounted for as an additional potential seen by atoms during quantum reflection. Explicitly including this potential predicts the saturation velocity and reflection probability accurately.

6.1   The failure of simple models

Excitations alone cannot describe the decreased reflection probability. Numeric simulations of reflecting condensates show that excitations do occur during the reflection process and
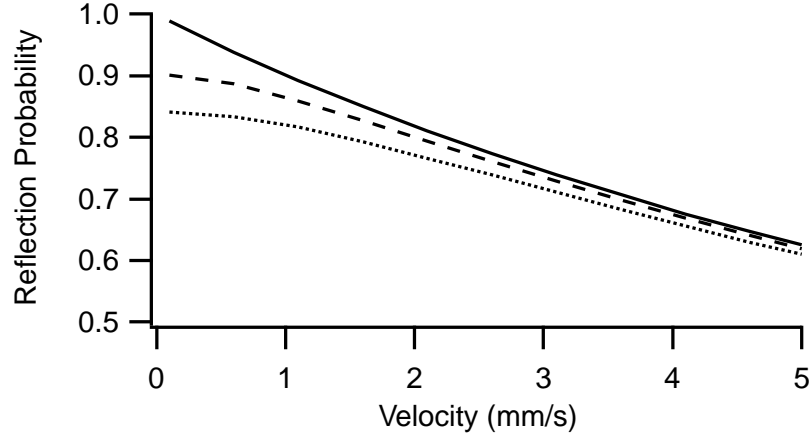
Figure 6-1: Predicted reflection probability when a "speed of sound" velocity is added in quadrature to the center of mass velocity. The solid, dashed and dotted curves are shown for a reduced density surface for the 0, 1.0 mm/s, and 1.7 mm/s speed of sound. These values correspond to a non-interacting BEC and an upper and lower limit on the speed of sound in our condensate.

that these excitations become most prominent when the incident velocity is low [162]. In the ideal case, a reflected BEC would have the same spatial profile as the incident BEC, but would have a reduced density. Excitations, on the other hand, re-distribute the incident BEC wavefunction so that there are large regions of reduced density far from the center of mass of the condensate. It was suggested that these regions of low density may go undetected and could account for the observed saturation at low velocity. Accounting for the severity of the saturation, however, required that the detection threshold be set far below our experimental threshold.

Neither can sum of the center of mass energy and the energy of the local speed of sound account for the observed saturation. In this model, the mean-field potential energy of the condensate, which must fall to zero at the surface (along with the condensate density) could accelerate the atoms into the Casimir-Polder potential, adding the speed of sound to any center of mass velocity. These velocities would, then, add in quadrature giving a non-zero incident velocity even in the absence of a center of mass velocity. This model predicts a less dramatic onset of any saturation effect than we observe. Figure 6-1 shows how this model varies for increasing values of the speed of sound.

6.2   An improved model for mean-field effects

Our improved model for including the effect of mean-field interactions is simple: quantum reflection is well described by a local process comprising single atoms interacting with a
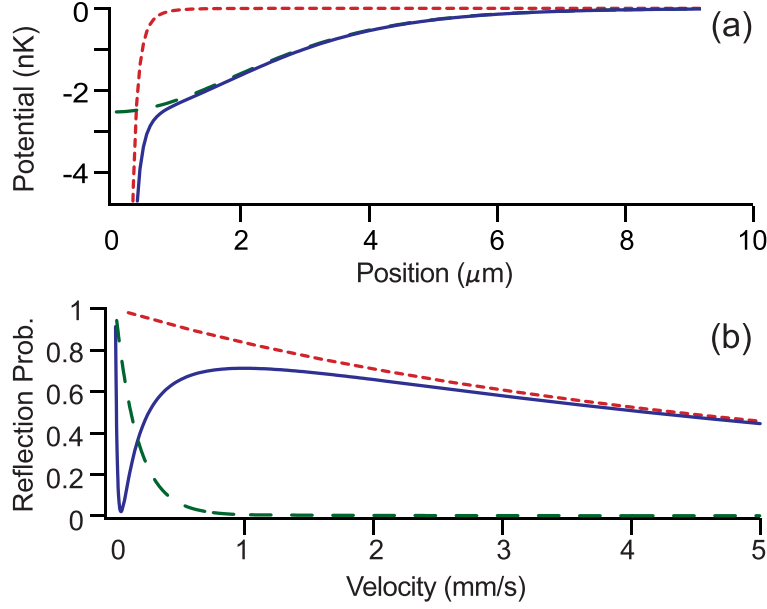
Figure 6-2: The mean field model for quantum reflection of condensates. (a) The condensate and harmonic trap provide a repulsive mean-field energy which is constant far from the surface and, within the healing length, falls to zero (dashed curve). This potential combines with the Casimir-Polder potential (dotted) to create the composite potential (solid curve) used to model quantum reflection of condensates. (b) The reflection probabilities from the same potentials at low velocity.

potential. To account for the effect of the trap and the presence of other atoms, the Gross-Pitaevskii equation is solved for the reflecting condensate, and the combined potential of the trap, the atoms, and the surface are summed to give the reflection potential for the atoms. Constructing such a model is made difficult, however, by the interaction between the reflection probability and the density in the trap at any point in time.

To create a tractable model which maintaining the relevant physics, we assume that the effect of the condensate can be accounted for by including a potential which is constant away from the surface and falls to zero at the surface over the healing length, ξ, as though a hard wall were present at the surface position, as shown in Figure 6-2. The expression used is $n(x) = n_0[\tanh x/\sqrt{2}\xi]^2$, where $n(x)$ and (n_0) the density and peak density of the condensate [136]. The combined potential differs only by an offset from the Casimir-Polder potential for distances $z \ll \xi$ and $z \gg \xi$, but is dominated by the mean field potential for $z \simeq \xi$. In this region, the potential is "softened" the edge of the condensate.

The effect on quantum reflection probabilities of including such a potential is dramatic. Regardless of the density used to determine the healing length, we find that near threshold (zero velocity), the reflection probability saturates and falls sharply before exhibiting the characteristic rise to unity reflection at zero velocity. We can understand this effect by

considering how the point of quantum reflection changes with incident velocity. At high velocity, the badlands is strongly peaked close to the surface, where the effect of the mean-field energy is small. Here, we recover the long healing length limit, and the reflection behaves as though the mean-field energy is just added to the incoming kinetic energy. As the velocity is reduced, the point of reflection moves further away from the surface and enters the region where the potential has been strongly influenced by the edge of the condensate. The gentle acceleration due to the edge of the condensate diminishes the effect of the abrupt acceleration due to the Casimir-Polder, causing the saturation and decline of the reflection probability. The rise to unity reflection at very low velocity is an artifact of the exact shape of the condensate; it corresponds to the badlands function being highly peaked inside the condensate.

If the density of the condensate could be further reduced, there would be two effects: (1) the healing length of the condensate becomes large and (2) the mean-field energy becomes small. The first change would reduce the distortion of the atom-surface potential in the region of reflection in our model. Instead of influencing the atoms during reflection, the condensate would pre-accelerate the atoms toward the surface as discussed in Section 6.1. The second effect would reduce the pre-acceleration to a negligible value, and explains why a similar effect is not observed with thermal beams at grazing incidence, where densities are much lower.

This simple model also recovers threshold behavior in the high density limit when the healing length is shorter than the reflection distance. This, however, is a failure of the model to account for the presence of the atom-surface potential; clearly the condensate density cannot remain unaffected in the presence of a strong absorber. It is expected that higher densities should lead to (1) further suppression of the maximum reflection coefficient and (2) a commensurate increase in the velocity where saturation occurs. This is the likely reason why we were unable to observe quantum reflection of atoms confined in the optical dipole trap, as described in Section 4.2.

6.3 Experimental results

The published experimental results of our work are included in Appendix C.

6.3.1 Reflection probability

Figure 6-3 is the major result of Ref. [132], reproduced here to show how the mean-field interaction model defines quantum reflection of BEC. Using the measured density to calculate the mean-field potential and healing length, and adjusting the value of C_4 to account for adsorbed atoms (see Section 5.2.2) and to match the well-behaved data at high velocity,
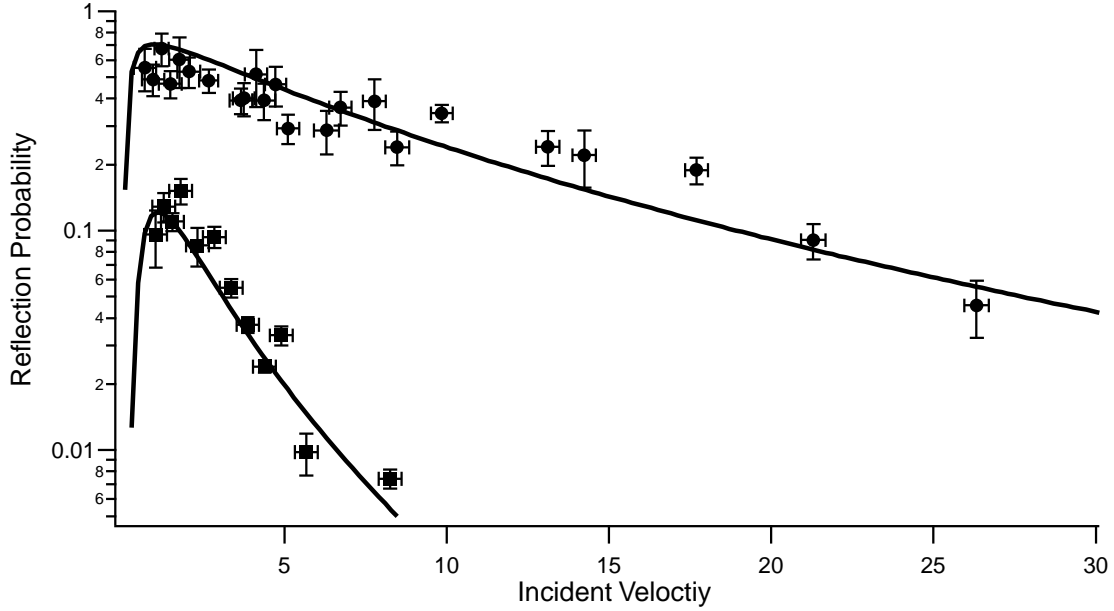
Figure 6-3: The reflection probability vs. incident velocity for atoms reflecting off solid and pillared silicon surfaces. The solid lines are a single parameter (the stray electric field gradient) fit to the data.

our simple model predicts the saturation of the reflection probability at very low velocities, as shown in Figure 6-3.

It is unfortunate that the experiment is limited to the predicted saturation region and does not adequately probe the predicted fall to 10% reflection probability that occurs near 0.1 mm/s.

6.3.2 Excitations during reflection

A condensate in the ground state of a harmonic trap has a well-defined, symmetric profile when imaged. Apart from the fundamental dipole oscillation, excitations to the condensate tend to induce density fluctuations. In collecting images of reflected condensates, as shown in Figure 6-4, it is clear that strong excitations are present in the reflected cloud. Quantum reflection of atoms is an abrupt process, resulting from the breakdown of the semiclassical treatment of the atom wavefunction. At the point of reflection, the reflected component of the atomic wavefunction interferes with the incident component to create strong density oscillations. This alone, however, does not lead to the excitations. Excitations require interactions between atoms to give a density dependent term in the Schrödinger equation, as discussed in Section 1.1.

There are two types of excitations present in our system: single particle excitations evidenced by the appearance of a scattering halo and collective excitations evidenced by a
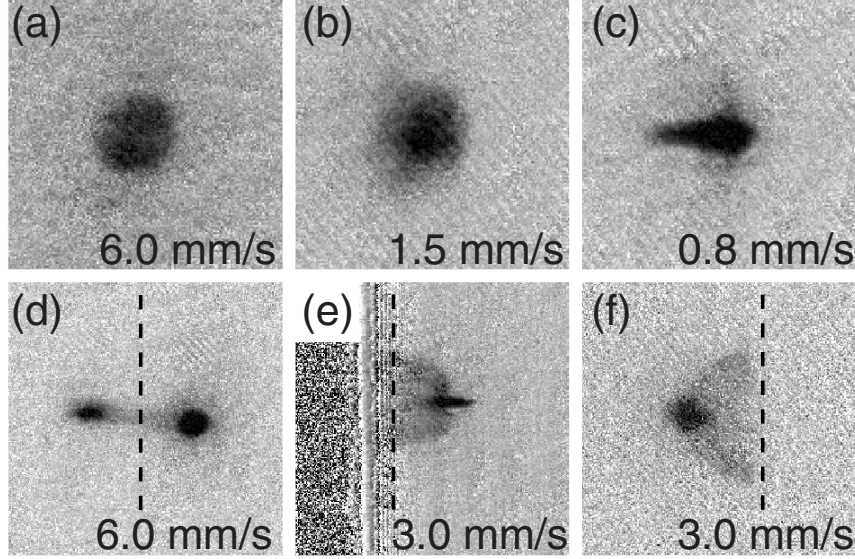
Figure 6-4: As the incident velocity is decreased, the reflected condensate becomes increasingly excited, as seen in panel (a)-(c). Panels (e) and (f) show the presence of the s-wave scattering halo. A movie showing reflection at 3 mm/s is available at http:/cua.mit.edu/ketterle_group/Animation_folder/QRMovie.wmv.

distortion of the reflected cloud. The single particle excitations are the result of individual atoms within the incident and reflecting condensate colliding and re-distributing their momentum [59, 26]. Conservation of energy and momentum in the two body collision require that atoms retain their initial energy and magnitude of momentum in the center of mass frame, but the direction of motion relative to the center of mass may take any direction. In time-of-flight or after an appropriate hold time, the scattered atoms lie on a spherical shell that appears like a halo when imaged, as in Figure 6-4e,f. This halo will be visible whenever the two clouds collide at sufficiently high density, that is, when the reflection probability is high. These excitations are not predicted by the Gross-Pitaevskii equation which describes only macroscopically occupied states. The re-introduction of these interactions can be handled by simulating quantum fluctuations as classical fluctuations on the initial state of the system via the truncated Wigner method [123, 124]. Collisions between atoms are then accounted for as four-wave mixing between the highly occupied modes of the colliding condensates and the quantum fluctuations. The scattering halos that we observe during reflection are well described in this way, as demonstrated in the simulations of Ref. [159].

The collective excitations we observe are more interesting, and have inspired extended numeric simulations. The "interferential disruption" is described in Ref. [162, 159]. When interference between incoming and reflected atoms is established, the density of the cloud is forced far from equilibrium. Halfway through the reflection, during the time of maximum

overlap, the average density is increased by a factor of $1 + R$, where R is the reflection probability. Additionally, interference fringes create regions of constructive and destructive interference, spaced at $1/k$, where k is the incident wavevector, further increasing the density in the regions of constructive interference, creating a series of "pancakes" parallel to the surface. This increased density leads to out of equilibrium mean-field interactions in the directions parallel to the surface. The condensate relaxes by expanding each pancake radially, in a sort of quadrupole oscillation. The interplay between (1) the constructive interference and (2) the resulting quadrupole oscillation leads to the formation of solitons and vortex rings. When the interference is long lived at low velocity, the quadrupole oscillation significantly re-distributes the condensate radially. At high velocity, the collective excitations are doubly suppressed: reduced reflected condensates mean weaker interference and high velocity means shorter time for the quadrupole oscillation to act. The collective excitations due to the density modulation during quantum reflection are similar to the excitations caused by accelerating an optical lattice through a condensate [161, 160, 34].

Chapter 7

Conclusion

7.1 Applications of quantum reflection

In recent years, encouraging work with high probability quantum reflection has led to speculation on useful applications of the effect. This section will review several proposals and explain how our work, including some unpublished results, might apply. The proposals are divided between three categories: trapping atoms, focusing and manipulating atom waves, and fundamental science.

7.1.1 Focusing atomic beams

As a technology driven sub-field, atom optics pursues the tools of optics (lenses, mirrors, beam splitters, etc.) for use with matter waves. While evanescent waves [87, 1] and permanently magnetized materials [74, 147] surpass solid surfaces as atom mirrors and ideal beam splitters are currently realized in both confined [82, 169] and free propagating [186] geometries, there is no equivalent of an ideal lens for atoms or atomic beams. The closest realization is a focusing Fresnel zone plate which works by diffraction [21, 40]. In this experiment, an atomic beam was partially focused from a 400 μm waist to a 25 μm waist and increased in intensity by a factor of 4. Unfortunately, the majority of the beam was unaffected by the zone plate, so the focused beam rested atop a plateau of unfocused atoms. A second approach takes advantage of the weak interaction between He and monolithic Si, which can be flexed by large electric fields, to quantum reflect helium into a partially focused beam [75]. Strong geometrical abberations limit the usefulness of such a system.

Quantum reflection finds a suggested use in two schemes for focusing atoms. In the first, dubbed the "atomic nanoscope", a transmissive, focusing mirror element is constructed from a conical hole in a silicon wafer [96]. A collimated atomic beam incident on the hole is partially reflected (ridges along the sides of the conical hole improve the reflectivity) and focused. While the beam intensity is greatly reduced, the brightness may still be increased

by the substantial focusing. A second scheme uses reflective Fresnel zone plates as a focusing element [84]. Simulations have demonstrated an increase in density of an order of magnitude when an appropriately designed zone plate is used in place of the plain or pillared surface in the normal incidence quantum reflection experiments described above. Both of these proposals are fairly simple extensions of previous work; more attention will probably be paid to the Kouznetsov proposal because it is designed to work with collimated atomic beams rather than with a condensate or atom laser [96].

7.1.2 Trapping of ultracold atoms

One attractive and widely touted use for quantum reflection is as universal confinement for ultracold atoms [86]. Some studies of quantum reflection have actually relied on lifetime measurements in such traps to determine the reflection probability [41, 193, 133]. Such a trap would be useful for precision measurements because, the absence of confining lasers and magnetic fields eliminates the fluctuations in these fields. Additionally, because the effective confining potential is very short range, affecting only atoms within a few microns of the walls, the atoms would behave as in a freely propagating state. Because the reflection probability approaches unity as the velocity of atoms approaches zero, a quantum reflection trap would be well suited to confining only the coldest of atomic samples. This too could be useful, for the predicted lifetime of an atom in the trap is proportional to its velocity; the sample would be effectively cooled by surface evaporation throughout the experiment [107, 69].

The publication of our result on normal incidence quantum reflection has sparked a series of papers by H. Friedrich [85, 108] discussing the physics of such traps. A similar proposal has even been suggested for the confinement of ultracold anti-hydrogen [184]. The primary finding of this work is an effective 100 fold improvement in the surviving atom fraction (to approximately 50%) for times ~ 400 ms when quantum reflection from surfaces provides confinement. This is comparable to what was observed in our "half-harmonic" quantum reflection trap reported in Ref. [133]. Confinement of atoms by quantum reflection against a gravitational field, however, may prove impossible given the strength of gravity [93]; it may be necessary to work in microgravity environments [183].

One final proposal suggests the use of quantum reflection traps to create new geometries for confining condensates [109]. Here, the 1D box potential of Refs. [85, 108] is extended to 2D in a square and circular trap. Both traps behave similarly to the 1D box potential.

Our work with quantum reflection traps (see Section 4.4.2) continued when we began using highly reflective structured surfaces. However, we did not observe a corresponding dramatic increase in the lifetime of atoms held against a structured surface. Rather, lifetimes similar to the plain surface trap were preliminarily observed. It is possible that our results are limited by the experimental technique: i.e. excitations may result due to the method

106

for bringing the atoms in contact with the surface.

7.1.3 Fundamental condensate physics

Condensates in dilute gases, for all of the attention directed toward them in the decade following their first observation, are still being studied for their basic properties. Quantum reflection of condensates has been used as a platform to study excitations [161, 162, 159] and vortices [105]. These works are, at this point, mostly about testing the limits of numerical simulations to explain the "messy" details of quantum reflection with condensates. In this regard, more detailed experimental studies of quantum reflection will encourage further developments in the field of simulations. Furthermore, as quantum reflection develops into useable technology, such simulations may reveal unrealized applications. Finally, as was demonstrated by our work [132], the role of mean-field interactions in quantum reflection are not well understood, and an encompassing theory is still wanting.

7.2 The future of the Science Chamber

Immediately following the achievement of Bose-Einstein condensation in 1995 and again when the Nobel Prize was awarded in 2001, the field of cold atoms drew enormous attention for its promise of controlled interactions and novel physics. In the intervening years, experiments at MIT and around the globe have helped to keep that promise. Quantum reflection is a beautiful effect with the promise of impacting the manipulation and storage of ultracold atoms. As such, interest in quantum reflection has grown in part as a result of the first experimental observations with alkali atoms. As has been shown in this thesis, BEC offers a new way of studying the effect and provides new insight into the line between mean-field physics and single-atom effects. This work has also uncovered some of the limitations of quantum reflection for confining and manipulating ultracold atoms; quantum reflection may be useful for particular applications where the lowest of temperatures and the elimination of all fluctuating fields are necessary, but its usefulness for universal storage is severely limited.

The Science Chamber was designed as a scouting experiment: as new opportunities presented themselves, it served as a quick way to explore possibilities. In the years I've spent at MIT, the machine has undergone many changes and I've had the opportunity to be involved with many subfields of cold atom physics. Over the last year, we've begun a major effort to rebuild the apparatus to join in a new paradigm of cold atom physics, the simulation of condensed matter systems. It is a very exciting time for BEC III as the finishing touches are put on the experiment and work can begin with the optical lattices and Feshbach resonances that have become, in the last 5 years, the new workhorses of atomic

physics.

When I arrived at MIT, there was a well-built experiment that allowed BEC III to contribute to the field unhindered for many years. I hope that as I move forward, the new foundation being laid provides for another era of contributions from the Science Chamber.

Appendix A

Cooling Bose-Einstein condensates below 500 picokelvin

A. E. Leanhardt, T. A. Pasquini, M. Saba, A. Schirotzek, Y. Shin, D. Kielpinski, D. E. Pritchard, and W. Ketterle

17. C. Salomon, talk presented at the Quantum Electronics and Laser Science Conference, Baltimore, MD, 5 June 2003.
18. T. Weber, J. Herbig, M. Mark, H.-C. Nägerl, R. Grimm, *Science* **299**, 232 (2003); published online 5 Dec 2002 (10.1126/science.1079699).
19. The optical trap has a depth of $k_B \times 45$ nK with a radial trap frequency of 18 Hz and an axial trap frequency of 6 Hz. The axial direction of the BEC is oriented in the horizontal plane. At 20 G, the Cs scattering length is $a = 163$ a_0, with a_0 denoting Bohr's radius. The resulting chemical potential for the BEC is $k_B \times 7$ nK.
20. Materials and methods are available as supporting material on *Science* Online.
21. V. Vuletić, C. Chin, A. J. Kerman, S. Chu, *Phys. Rev. Lett.* **83**, 943 (1999).
22. P. S. Julienne, E. Tiesinga, private communication (2003).
23. C. Chin, V. Vuletić, A. J. Kerman, S. Chu, *Phys. Rev. Lett.* **85**, 2717 (2000).
24. P. J. Leo, C. J. Williams, P. S. Julienne, *Phys. Rev. Lett.* **85**, 2721 (2000).
25. The molecular state was identified as a high-lying rovibrational state with internal angular momentum $f = 4$, magnetic quantum number $m_f = 4$, molecular orbital angular momentum $L = 4$, and angular momentum projection $m_L = 2$.
26. T. Weber, J. Herbig, M. Mark, H.-C. Nägerl, R. Grimm, *Phys. Rev. Lett.*, in press (available at http://arXiv.org/abs/physics/0304052).
27. V. A. Yurovsky, A. Ben-Reuven, P. S. Julienne, C. J. Williams, *Phys. Rev. A* **62**, 043605 (2000).
28. This is a reasonable assumption, because no molecules can be created in the absence of atoms.
29. M. R. Andrews *et al.*, *Science* **275**, 637 (1997).
30. D. Jaksch, V. Venturi, J. I. Cirac, C. J. Williams, P. Zoller, *Phys. Rev. Lett.* **89**, 040402 (2002).
31. M. Greiner, O. Mandel, T. Esslinger, T. W. Hänsch, I. Bloch, *Nature* **415**, 39 (2002).
32. We thank P. S. Julienne for very helpful discussions. Supported by the Austrian Science Fund (FWF) within Spezialforschungsbereich 15 (project part 16) and by the European Union through the Cold Molecules Training and Mobility of Researchers Network under contract no. HPRN-CT-2002-00290.

Cooling Bose-Einstein Condensates Below 500 Picokelvin

A. E. Leanhardt,* T. A. Pasquini, M. Saba, A. Schirotzek, Y. Shin, D. Kielpinski, D. E. Pritchard, W. Ketterle

Spin-polarized gaseous Bose-Einstein condensates were confined by a combination of gravitational and magnetic forces. The partially condensed atomic vapors were adiabatically decompressed by weakening the gravito-magnetic trap to a mean frequency of 1 hertz, then evaporatively reduced in size to 2500 atoms. This lowered the peak condensate density to 5×10^{10} atoms per cubic centimeter and cooled the entire cloud in all three dimensions to a kinetic temperature of 450 ± 80 picokelvin. Such spin-polarized, dilute, and ultracold gases are important for spectroscopy, metrology, and atom optics.

The pursuit of lower temperatures is motivated by the quest to observe phenomena that occur on very low energy scales, in particular, phase transitions to new forms of matter. The achievement of temperatures near 1 K in solids and in liquids led to the discoveries of superconductivity (*1*) and superfluidity (*2*), respectively. The advent of laser cooling resulted in microkelvin temperature atomic vapors (*3–5*), subsequently cooled to nanokelvin temperatures by evaporative cooling to form dilute Bose-Einstein condensates (*6*, *7*) and quantum degenerate Fermi gases (*8*). Collectively, these low-temperature systems have a host of applications, including superconducting quantum interference devices (SQUIDs) (*9*), superfluid gyroscopes (*10*, *11*), and atomic clocks (*12*).

Temperature is a quantity that parameterizes how energy is distributed across the available states of a system, and effective temperatures can be defined for decoupled degrees of freedom or subsets of particles. For example, nuclear spins isolated from the kinetic motion of their respective atoms have been cooled by adiabatic demagnetization to an effective temperature of 280 pK (*13*). Spin ensembles have a finite number of available states, such that a spin-polarized sample, as in our work, would be characterized by zero effective temperature. In contrast, the motion of free particles is subject to a continuum of states, and the kinetic temperature of an ensemble can only asymptotically approach absolute zero.

Effective temperatures in atomic vapors are defined by the widths of velocity distributions, which can be much smaller than the mean velocity of the sample. Raman cooling (*14*, *15*) and velocity-selective coherent population trapping (VSCPT) (*16*) have generated velocity distributions with very narrow peaks, corresponding to nanokelvin and picokelvin effective temperatures. However, these temperatures were associated with the motion of only a subset of the atoms in the cloud and/or with atomic motion in only one dimension.

For trapped, partially condensed atomic vapors, the condensate fraction has zero entropy and the kinetic temperature of the sample is determined by the velocity distribution of the thermal (noncondensed) component. When released, the condensate fraction expands more slowly than the thermal compo-

nent and has been characterized by picokelvin effective temperatures for anisotropic (*17*) and noninteracting (*18*) gases.

Cooling the atomic motion of entire ensembles in all three dimensions has proven difficult. To date, kinetic temperatures of a few hundred nanokelvin have been achieved with adiabatic and optical cooling (*19*, *20*), and evaporative cooling techniques have produced condensates with temperatures of 3 nK (*21*). By adiabatic expansion and subsequent evaporation, we have cooled partially condensed atomic vapors to picokelvin kinetic temperatures.

Our thermometry is calibrated by the Bose-Einstein condensation (BEC) phase transition temperature, T_c, which in the thermodynamic limit for a harmonically trapped ideal Bose gas is (*22*)

$$k_B T_e = \hbar\bar{\omega}\left(\frac{N}{\zeta(3)}\right)^{1/3} \approx 0.94\hbar\bar{\omega}N^{1/3} \qquad (1)$$

where k_B is Boltzmann's constant, $\hbar$ is Planck's constant h divided by 2π, $\zeta(n)$ is the Riemann Zeta function, $\bar{\omega} = (\omega_x\omega_y\omega_z)^{1/3}$ is the geometric mean of the harmonic trap frequencies, and N is the total number of atoms, both condensed and noncondensed. Thus, the atom number and the trap frequencies set an upper limit for the temperature of a confined Bose-Einstein condensate. In our work, adiabatically weakening the trapping potential to a mean frequency of $\bar{\omega} = 2\pi \times (1.12 \pm 0.08)$ Hz guaranteed that partially condensed atomic vapors with $N \leq 8000$ atoms had picokelvin temperatures ($T_c \leq 1$ nK).

Bose-Einstein condensates containing more than 10^7 ^{23}Na atoms were created in the weak field seeking $|F = 1, m_F = -1\rangle$ state in a magnetic trap, captured in the focus of an optical tweezers laser beam, and transferred into an auxiliary "science" chamber as described in (*23*). In the science chamber, condensates containing 2×10^6 to 3×10^6 atoms were transferred from the optical tweezers into a gravito-magnetic trap (Fig. 1A). A small coil carrying current I_S generated a vertical bias field B_z and supported the condensates against gravity with a vertical magnetic field gradient, $B_z' = 2\ mg/$

Department of Physics, MIT-Harvard Center for Ultracold Atoms, and Research Laboratory of Electronics, Massachusetts Institute of Technology, Cambridge, MA 02139, USA.

*To whom correspondence should be addressed. E-mail: ael@mit.edu

$\mu_B \approx 8$ G/cm, where m is the atomic mass, g is the gravitational acceleration, and μ_B is the Bohr magneton. Additional control over B_z and B'_z was provided by two external coils carrying independent currents I_U and I_L. Weak curvature, B'_z, to the vertical bias field created stable vertical confinement such that a harmonic restoring force was provided magnetically (gravitationally) for downward (upward) vertical displacements (Fig. 1B). A radial field gradient, $B'_r = \partial B_r / \partial r = -B'_z/2$, was also present and added in quadrature with B_z to provide harmonic radial confinement with a restoring force proportional to $(B'_r)^2/B_z$ (Fig. 1C). The trapping potential does not have fundamental radial asymmetries as do previously demonstrated Ioffe-Pritchard magnetic traps (17, 24, 25). In principle, stable three-dimensional confinement is possible above a single coil in the presence of gravity without the aid of external bias fields or gradients.

For typical loading parameters—$I_S = 340$ mA, $I_U = 5.5$ A, and $I_L = 0$—the gravito-magnetic trap was spherically symmetric, with trap frequencies $\omega_x \approx \omega_y \approx \omega_z \approx 2\pi \times 8$ Hz. Condensates loaded into the gravito-magnetic trap from the optical tweezers were held for 5 s to allow for the damping of excitations. The resulting partially condensed clouds had $\sim 5 \times 10^5$ atoms and a BEC transition temperature $T_c = 30$ nK. Throughout our work, the atomic vapor maintained a temperature T such that $0.5 < T/T_c < 1$.

Further cooling was accomplished by adiabatically decompressing the trapping potential in two 5 s stages, with a 5 s delay in between to allow excitations to damp. In the first stage, the vertical frequency was reduced to $\omega_z = 2\pi \times (1.81 \pm 0.05)$ Hz by simultaneously raising currents I_L and I_U by identical amounts and lowering the current I_S by a factor of 10. This transferred the dominant source of magnetic field gradient from the small coil to the external coils, with the remaining vertical curvature still due to the reduced I_S. In the second stage, the radial frequencies were reduced to $\omega_x = 2\pi \times (0.65 \pm 0.05)$ Hz and $\omega_y = 2\pi \times (1.2 \pm 0.1)$ Hz by raising I_L and lowering I_U by identical amounts. The vertical magnetic field gradient and curvature remained constant, but the vertical bias field, B_z, increased. This reduced the radial confinement due to the scaling $\omega_r \propto B'_r / B_z^{1/2}$ (24, 25).

For currents $I_S = 34$ mA, $I_U = 14$ A, and $I_L = 44$ A, the final gravito-magnetic trap had a measured mean frequency $\bar{\omega} = 2\pi \times (1.12 \pm 0.08)$ Hz and axial bias field $B_z = 17$ G. The residual anharmonicities of the trapping potential were small, with $\Delta\omega/\omega = 0.1$ for 500 μm displacements from the trap center. Further radial decompression was not possible because of a finite trap depth (Fig. 1C) and sensitivity of trap stability to milligauss level radial bias fields.
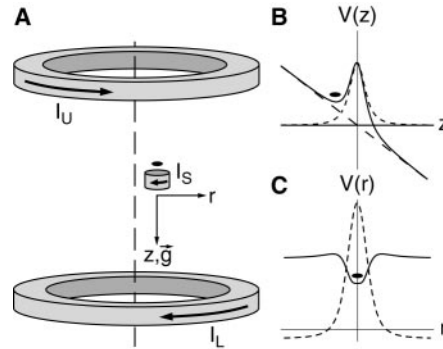

Fig. 1. Gravito-magnetic trap. (**A**) Bose-Einstein condensates were levitated against gravity $\sim$5 mm above a 1-cm diameter, 25-turn coil mounted inside the ultrahigh vacuum chamber running current I_S. Two 10-cm diameter, 20-turn coils were mounted outside the vacuum chamber and were supplied individually with currents I_U and I_L. The vertical separation between the large coils was 10 cm. The 1-cm diameter coil was mounted radially off-axis with respect to the pair of 10-cm diameter coils by $\sim$1 cm. This broke the cylindrical symmetry of the trapping potential. Additional bias fields of $\sim$1 G were applied in the horizontal plane to cancel the radial magnetic fields generated by I_U and I_L on the axis of the small coil and to maintain a stable trapping potential. $\vec{g}$ denotes the direction of gravitational acceleration. (**B**) Magnetic potential due to I_S (short dashed line), gravitation potential (long dashed line), and joint vertical potential of the gravito-magnetic trap (solid line). (**C**) A radially repulsive potential magnetic potential was generated by running I_S alone (dashed line); however, applying a slight antibias field with I_U modified the radial energy profile and created a magnetic field minimum at $r = 0$ (solid line). In (A) to (C), the solid oval denotes the trapped condensate.

After decompression, the partially condensed atomic vapors had $\sim 2 \times 10^5$ atoms and a BEC transition temperature $T_c = 3$ nK. T_c was lowered further by reducing the number of atoms in the cloud (Eq. 1), while maintaining a substantial condensate fraction at all times ($0.5 < T/T_c < 1$). The atom number was reduced by holding the atoms in the gravito-magnetic trap for up to 200 s. Often, microwave radiation near the $|1, -1\rangle \rightarrow |2, 0\rangle$ transition was applied to shorten the hold time required to arrive at lower atom number to 10 s. The atom number reduction was accompanied by cooling, during which the elastic collision rate (between thermal atoms and the condensate) dropped from 0.25 Hz to 0.01 Hz. Therefore, a few collisions were sufficient to cause evaporation out of the finite depth trap. This cooling was not efficient in the sense of providing a gain in phase-space density but still was capable of maintaining thermal equilibrium and lowering the absolute temperature of the vapor.

Using this technique, we cooled partially condensed vapors containing up to 30,000 atoms to temperatures below 1 nK (Figs. 2 and 3). Our lowest measured three-
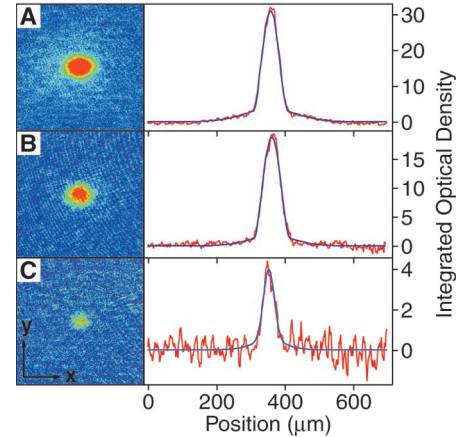

Fig. 2. Picokelvin temperature thermometry. Partially condensed atomic vapors confined in the gravito-magnetic trap with (**A**) 28,000, (**B**) 16,000, and (**C**) 2,500 atoms. The one-dimensional cross sections (red) were obtained by integrating the two-dimensional absorption images of the trapped clouds along the y axis. Bimodal fits to Eq. 2 (blue) yielded temperatures of (A) 1.05 $\pm$ 0.08 nK, (B) 780 $\pm$ 50 pK, and (C) 450 $\pm$ 80 pK, where the uncertainty is due to the fit of an individual image. The absorption imaging light was resonant with the $F = 2 \rightarrow F' = 3$ cycling transition for the trapped atoms and was aligned with the vertical (z) axis. The atoms were optically pumped into the $F = 2$ hyperfine level with a pulse resonant with the $F = 1 \rightarrow F' = 2$ transition. The field of view for the absorption images in (A) to (C) is 460 μm $\times$ 460 μm.

dimensional kinetic temperature was 450 $\pm$ 80 pK for 2500 atoms at a peak condensate density of 5×10^{10} atoms/cm^3. Under these conditions, the peak atom-atom interaction energy was $\mu = k_B \times 33$ pK, while the zero point energy of the harmonic trapping potential was $(1/2)\hbar\bar{\omega} k_B \times 24$ pK. Condensates released from the gravito-magnetic trap would expand with energies of this order and therefore could be characterized by effective temperatures $\sim$30 pK.

Additional cooling would require lowering the trap frequencies further or reducing the atom number more. However, weakly confining traps have proven technically difficult to control such that lowering $\bar{\omega}/2\pi$ substantially below 1 Hz is challenging. Likewise, because $T_c \propto N^{1/3}$, atom number reduction by an order of magnitude only results in temperature reduction by a factor of two. Furthermore, lower temperatures and lower densities are accompanied by collisional equilibrium times approaching 100 s.

Because $\mu \approx \hbar\bar{\omega}$, the condensates in the gravito-magnetic trap were in a density regime intermediate between the Thomas-Fermi ($\mu >> \hbar\bar{\omega}$) and ideal ($\mu << \hbar\bar{\omega}$) gas limits. No simple approximation describes the condensate wave function, but the number of thermal atoms, $N_{th} = \zeta(3) \times (k_B T \hbar\bar{\omega})^3$, and the width of their distribution,
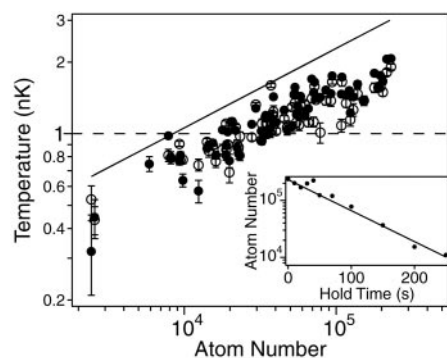
Fig. 3. Bose-Einstein condensates at picokelvin temperatures. The temperature of more than 60 partially condensed atomic vapors is plotted versus total number of condensed and noncondensed atoms. A solid line at the Bose-Einstein condensation phase transition temperature (Eq. 1) and a dashed line at 1 nK are provided as guides. Condensate temperatures were determined from one-dimensional fits to atomic density cross sections integrated along either the x (closed circles) or y (open circles) axis (Fig. 2). Differences in the two measured temperatures for a single condensate reflect the true uncertainty of the measurement. Plotted error bars represent the statistical uncertainty of the fit. The inset shows that the $1/e$ condensate lifetime in the gravito-magnetic trap was limited by one-body processes to 80 ± 5 s.

$w_{th} = (2k_B T / m\omega^2)^{1/2}$, in any spatial direction, can be related to the temperature, provided that the thermal energy is much larger than the trap level spacing, $k_B T \gg \hbar \bar{\omega}$, where ω is the trap frequency for the axis along which w_{th} is measured (22). The ratio of atoms in the condensate, N_0, to the total number of atoms, $N = N_0 + N_{th}$, is also related to the temperature through $N_0/N = 1 - (T/T_c)^3$. N_0, N_{th}, and w_{th} are therefore completely determined by T and N.

The temperature of the atomic vapors was extracted by fitting integrated, one-dimensional atomic density cross sections to a bimodal distribution (Fig. 2)

$$n(x) = N_0 \Psi_0^2 + \frac{N_{th}}{\sqrt{\pi} w_{th}} e^{- x^2/w_{th}^2} \quad (2)$$

where Ψ_0^2 is a bell-shaped function with width w_0 that describes the condensate peak [$\Psi_0^2 = (15 / 16) w_0^{-1} \max(1 - x^2 / w_0^2, 0)^2$ for a Thomas-Fermi gas and $\Psi_0^2 = w_0^{-1}\pi^{-1/2} \exp(- x^2 / w_0^2)$ for an ideal gas]. The fitted parameters were T, N, and w_0. We checked that the fitted temperature did not depend on the exact choice of the condensate wave function (inverted parabola or gaussian) or the application of microwave radiation to reduce atom number.

All atomic vapors represented in Fig. 3 had a clear bimodal density distribution from which a temperature was reproducibly extracted. The temperatures extracted from one-dimensional fits along both radial axes were nominally the same, empirically indicating

that the atomic vapors remained close to thermal equilibrium at all times.

In conclusion, we have created long-lived (80 ± 5 s), low-temperature (450 ± 80 pK), and low-density (5×10^{10} atoms/cm^3) partially condensed atomic vapors using a weakly confining [$\varpi = 2\pi \times (1.12 \pm 0.08)$ Hz] gravito-magnetic trap. These samples are characterized by a thermal velocity ~ 1 mm/s, a speed of sound ~ 100 μm/s, and a healing length limited by the ~ 20-μm harmonic oscillator length of the trapping potential. Low-temperature and low-density ensembles are important for spectroscopy, metrology, and atom optics. In addition, they are predicted to experience quantum reflection from material surfaces (26–28).

References and Notes
1. H. G. Smith, J. O. Wilhelm, *Rev. Mod. Phys.* **7**, 237 (1935).
2. K. Darrow, *Rev. Mod. Phys.* **12**, 257 (1940).
3. S. Chu, *Rev. Mod. Phys.* **70**, 685 (1998).
4. C. N. Cohen-Tannoudji, *Rev. Mod. Phys.* **70**, 707 (1998).
5. W. D. Phillips, *Rev. Mod. Phys.* **70**, 721 (1998).
6. E. A. Cornell, C. E. Wieman, *Rev. Mod. Phys.* **74**, 875 (2002).
7. W. Ketterle, *Rev. Mod. Phys.* **74**, 1131 (2002).
8. B. DeMarco, D. S. Jin, *Science* **285**, 1703 (1999).
9. A. H. Silver, J. E. Zimmerman, *Phys. Rev. Lett.* **15**, 888 (1965).
10. K. Schwab, N. Bruckner, R. E. Packard, *Nature* **386**, 585 (1997).
11. O. Avenel, P. Hakonen, E. Varoquaux, *Phys. Rev. Lett.* **78**, 3602 (1997).
12. T. Udem, R. Holzwarth, T. W. Hänsch, *Nature* **416**, 233 (2002).
13. A. S. Oja, O. V. Lounasmaa, *Rev. Mod. Phys.* **69**, 1 (1997).
14. M. Kasevich, S. Chu, *Phys. Rev. Lett.* **69**, 1741 (1992).
15. J. Reichel *et al.*, *Phys. Rev. Lett.* **75**, 4575 (1995).
16. B. Saubaméa *et al.*, *Phys. Rev. Lett.* **79**, 3146 (1997).
17. M.-O. Mewes *et al.*, *Phys. Rev. Lett.* **77**, 416 (1996).
18. T. Weber, J. Herbig, M. Mark, H.-C. Nägerl, R. Grimm, *Science* **299**, 232 (2003).
19. A. Kastberg, W. D. Phillips, S. L. Rolston, R. J. C. Spreeuw, *Phys. Rev. Lett.* **74**, 1542 (1995).
20. P. Treutlein, K. Y. Chung, S. Chu, *Phys. Rev. A* **63**, 051401(R) (2001).
21. E. A. Donley, N. R. Claussen, S. T. Thompson, C. E. Wieman, *Nature* **417**, 529 (2002).
22. F. Dalfovo, S. Giorgini, L. P. Pitaeskii, S. Stringari, *Rev. Mod. Phys.* **71**, 463 (1999).
23. T. L. Gustavson *et al.*, *Phys. Rev. Lett.* **88**, 020401 (2002).
24. Y. V. Gott, M. S. Ioffe, V. G. Tel'kovskii, *Nuc. Fus. Suppl.* **3**, 1045 (1962).
25. D. E. Pritchard, *Phys. Rev. Lett.* **51**, 1336 (1983).
26. A. Anderson *et al.*, *Phys. Rev. A* **34**, 3513 (1986).
27. J. J. Berkhout *et al.*, *Phys. Rev. Lett.* **63**, 1689 (1989).
28. F. Shimizu, *Phys. Rev. Lett.* **86**, 987 (2001).
29. This work was funded by the Army Research Office, NSF, Office of Naval Research, and NASA. We thank C. V. Nielsen for experimental assistance and J. K. Thompson for critical comments on the manuscript. M.S. acknowledges additional support from the Swiss National Science Foundation.

Observation of Polymer Conformation Hysteresis in Extensional Flow

Charles M. Schroeder,[1] Hazen P. Babcock,[2]* Eric S. G. Shaqfeh,[1,3] Steven Chu[2]†

Highly extensible *Escherichia coli* DNA molecules in planar extensional flow were visualized in dilute solution by fluorescence microscopy. For a narrow range of flow strengths, the molecules were found in either a coiled or highly extended conformation, depending on the deformation history of the polymer. This conformation hysteresis persists for many polymer relaxation times and is due to conformation-dependent hydrodynamic forces. Polymer conformational free-energy landscapes were calculated from computer simulations and show two free-energy minima for flow strengths near the coil-stretch transition. Hysteresis cycles may directly influence bulk-solution stresses and the development of stress-strain relations for dilute polymer flows.

The behavior of long-chain, flexible polymer molecules in extension-dominated flows has been the subject of research discussion for more than 30 years (1). Flows of dilute polymer solutions exhibit several interesting macroscopic effects including flow-dependent viscosity, enhanced normal stresses, and turbulent-drag reduction. Such non-Newtonian fluid properties result from flow-induced changes in the polymer conformations in solution. In short, a flowing fluid will influence polymer configurations in solution, and the forces exerted back on the fluid are directly related to the molecular conformations.

Polymer conformations and the resultant bulk-solution stresses are affected by flow type. In general, flows with a large rotational

[1]Department of Chemical Engineering, [2]Departments of Physics and Applied Physics, [3]Department of Mechanical Engineering, Stanford University, Stanford, CA 94305, USA.

*Present address: Department of Chemistry and Chemical Biology, Harvard University, Cambridge, MA 02138, USA.
†To whom correspondence should be addressed. E-mail: schu@stanford.edu

Appendix B

Quantum reflection from a solid surface at normal incidence

Reprinted article with permission from:

T. A. Pasquini, Y. Shin, C. Sanner, M. Saba, A. Schirotzek, D. E. Pritchard, and W. Ketterle
"Quantum reflection from a solid surface at normal incidence,"
Physical Review Letters 93, 223201 (2004).

Quantum Reflection from a Solid Surface at Normal Incidence

T. A. Pasquini, Y. Shin, C. Sanner, M. Saba, A. Schirotzek, D. E. Pritchard, and W. Ketterle*

*Department of Physics, MIT-Harvard Center for Ultracold Atoms,
and Research Laboratory of Electronics, Massachusetts Institute of Technology, Cambridge, Massachusetts, 02139, USA*
(Received 15 June 2004; published 24 November 2004)

We observed quantum reflection of ultracold atoms from the attractive potential of a solid surface. Extremely dilute Bose-Einstein condensates of ^{23}Na, with peak density 10^{11}–10^{12} atoms/cm^3, confined in a weak gravitomagnetic trap were normally incident on a silicon surface. Reflection probabilities of up to 20% were observed for incident velocities of 1–8 mm/s. The velocity dependence agrees qualitatively with the prediction for quantum reflection from the attractive Casimir-Polder potential. Atoms confined in a harmonic trap divided in half by a solid surface exhibited extended lifetime due to quantum reflection from the surface, implying a reflection probability above 50%.

Quantum reflection is a process in which a particle reflects from a potential without reaching a classical turning point. A solid surface provides a long-range attractive potential for atoms. At separation, r, much larger than the atomic radius the potential follows the Casimir-Polder expression $U = -C_4/[(r + 3\lambda/2\pi^2)r^3]$, where λ is the effective atomic transition wavelength [1]. Classically, an atom incident on such a potential will be accelerated toward the surface, resulting in inelastic scattering or adsorption. A quantum mechanical treatment of an atom-surface collision reveals that the atom is reflected from the purely attractive surface potential if the potential energy changes abruptly on a length scale set by the quantum mechanical wavelength [2–5]. The condition for significant reflection is that the local particle wave number normal to the surface, $k_\perp = \sqrt{k_\infty^2 - 2mU/\hbar^2}$, change by more than $k_\perp$ over a distance $1/k_\perp$. Here, $k_\infty = mv_\perp/\hbar$ is the normal wave number of the atom far from the surface, m is the atomic mass, $v_\perp$ is the normal incident velocity, and $\hbar$ is the Planck constant divided by 2π. The reflection probability, R, tends to unity as the incident velocity tends to zero, $R \approx 1 - 4\beta_4 mv_\perp/\hbar$, where β_4 is the length scale associated with the C_4 coefficient, $C_4 = \beta_4^2\hbar^2/2m$. High probability quantum reflection requires low incident velocity or weak attraction to the surface, conditions previously realized only in exceptional systems.

Studies of quantum reflection were first performed with helium or hydrogen atoms incident on liquid helium surfaces [6–9]. The extremely weak interaction strengths and low mass atoms allowed for quantum reflection at relatively high incident energies of $\sim k_B \times 10$ mK [6,9], where k_B is the Boltzmann constant. Reflection of noble and alkali atoms from a solid surface requires that atoms be incident with a million times less energy, $\sim k_B \times 10$ nK. This has been accomplished only by letting untrapped atoms hit solid surfaces at grazing incidence [10–14], meaning that most of the velocity is directed parallel to the surface and reflection only deflects atoms slightly.

Reflection probabilities in excess of 60% have been observed for incidence angles of a few milliradians [12]. Atom-surface potentials have also been studied in the presence of evanescent light waves generated by total internal reflection at a glass surface [15,16].

Normal-incidence quantum reflection of trapped atoms may be exploited in the construction of novel atom-optical devices. The current generation of atom mirrors for reflecting, confining, and focusing ultracold atoms employs evanescent waves produced by total internal reflection of laser light [17] or magnetized materials [18]. An atom-optical device based on quantum reflection is in a category of its own, as it works using the universal atom-surface interaction and depends on the long wavelength of ultracold atoms. Past experiments with grazing incidence atomic beams have demonstrated a mirror [11], a reflective diffraction grating [12], and a hologram based on quantum reflection [13].

In this Letter, we demonstrate normal-incidence quantum reflection of ultracold sodium atoms. Using the harmonic trapping potential of a gravitomagnetic trap [19,20], we varied the center of mass velocity of dilute Bose-Einstein condensates and induced controlled collisions with a silicon surface at velocities as low as 1 mm/s, corresponding to collision energies of $k_B \times 1.5$ nanokelvin or 1.2×10^{-13} eV. A reflection probability of $\sim 20\%$ was obtained for an incident velocity of 2 mm/s, realizing an atom mirror. Our experimental results are in qualitative agreement with theoretical predictions for single atoms incident on a conducting surface. Additionally, atoms were confined in one dimension by a silicon surface, where lifetime measurements indicate reflection probabilities in excess of 50%.

Bose-Einstein condensates of ^{23}Na atoms were prepared and transferred into a gravitomagnetic trap, comprising a single coil and three external bias fields, as described in Ref. [19]. Mounted 1 cm above the center of the single coil was a $\sim 20~\mu$m thick N-type doped polished Si (100) surface with a resistivity of 1–10 Ω cm. For typical loading parameters, condensates

containing 3×10^5 atoms were confined 200 μm to one side of the surface in a harmonic trap characterized by $(\omega_\perp, \omega_y, \omega_z) = 2\pi \times (10, 10, 6.5)$ Hz, where $\omega_\perp$ is the horizontal trap frequency perpendicular to the surface, ω_y is the horizontal trap frequency parallel to the surface, and ω_z is the vertical trap frequency. At this point, $\omega_\perp$ and ω_y were adjusted between 11 to 2 Hz by changing the vertical bias field as described in Ref. [19]. The position of the trap center relative to the surface was controlled by applying a bias field, $B_\perp$, perpendicular to the surface [21]. Empirically, we find that near the surface the non-condensed fraction of the atomic cloud is reduced by the "surface evaporation" effect, in which adsorption preferentially removes the hottest atoms from the cloud [22,23].

The dipole mode of a harmonically trapped condensate is identical to the behavior of a pendulum; atoms oscillate with amplitude A and trap period $T_\perp = 2\pi/\omega_\perp$. The presence of a surface within the trapping potential dramatically alters the dipole oscillation in the same way a wall would alter the oscillation of a pendulum. Bose-Einstein condensates undergoing dipole oscillation in the gravitomagnetic trap were made to collide with the solid silicon surface as described in Fig. 1(a). Collision with the surface occurred at time $\tau_C \approx T_\perp/4$ with incident velocity $v_\perp = A\omega_\perp \approx 1.5$ mm/s. This phenomenon is observed in Fig. 2. Near τ_C, two distinct velocity classes were visible corresponding to atoms in the initial condensate and atoms reflected from the surface. The simultaneous presence of incident and reflected atoms is explained by the fact that the back of the condensate hits

the surface $\sim$40 ms after the front end due to the $\sim$60 μm condensate diameter and slow (1.5 mm/s) velocity. At collision, the harmonic motion of the atoms was phase shifted by $2(\pi - \omega_\perp \tau_C)$, as seen in Fig. 2(b).

The reflected atom cloud was smaller than the incident one and had a comparable density. In some instances, the cloud appeared to have a bimodal distribution, indicating that coherence might be preserved in the collision. The reflected atoms continued to oscillate in the trap with the original amplitude, suggesting that atoms reflected specularly and that the kinetic energy was conserved during the collision. Eventually, the reflected atom cloud underwent a second collision with the surface at $\sim T_\perp/2$ after the first collision. Additional collisions were not observed as the atom number fell below our detection limit.

We observed reflected fractions that varied from 0–20% over the incident velocity range of 1–8 mm/s, corresponding to a collision energy of $\sim k_B \times (1 - 100)$ nK, for atoms with a peak density of $\sim 2 \times 10^{12}$ cm^{-3} in a $2\pi \times (3.3, 2.5, 6.5)$ Hz trap. Figure 3 shows the measured reflection probability, defined as the
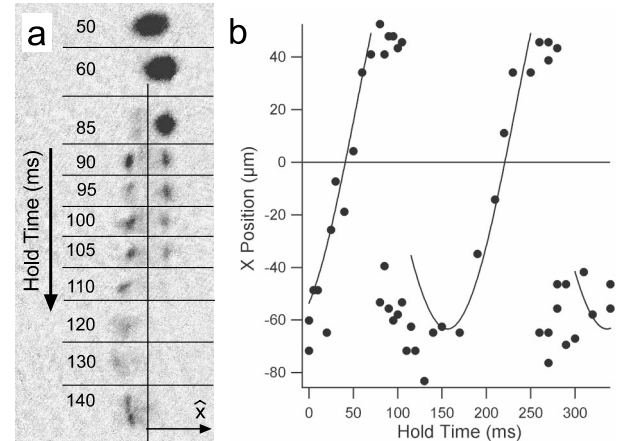
FIG. 2.   Atoms reflecting from a Si surface. Atoms confined $\sim$70 μm from a Si surface were transferred into a harmonic trap centered on the surface with $2\pi \times (3.3, 2.5, 6.5)$ Hz. The dipole oscillation of the condensate was interrupted periodically by collisions with the surface, which reversed the cloud's center of mass velocity. After a variable hold time, atoms were released from the trap, fell below the edge of the surface and were imaged with resonant light after 26 ms time of flight. The position of the atoms in time of flight is the sum of the in-trap position at the time of release and the product of the release velocity and time of flight. (a) Time-of-flight images of atoms after increasing hold times show the partial transfer of atoms from the initial condensate (right) into the reflected cloud (left) as the collision occurs. The separation is due to the reversed velocity. The vertical line shows the horizontal location of the surface. The field of view is 1.4 mm wide. (b) The time-of-flight positions of the incident and reflected atom clouds relative to the surface are well modeled by a single particle undergoing specular reflection in a half harmonic trap (solid line). During collision, the behavior deviates from the single particle model because of the finite cloud diameter of $\sim$60 μm. A second reflection is visible at 270 ms.
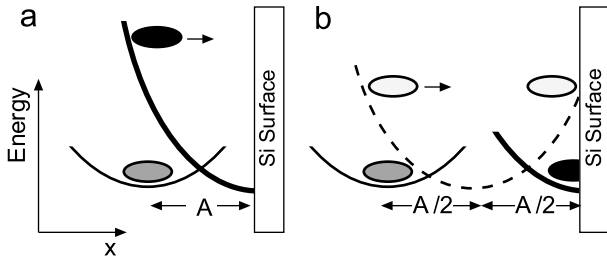

FIG. 1.   Experimental schematic. Atoms were confined in a gravitomagnetic trap [19] with trap frequencies ranging from $2\pi \times (2, 2, 6.5)$ Hz to $2\pi \times (11, 11, 6.5)$ Hz, near a $\sim$20 μm thick Si surface. (a) Quantum reflection was studied by inducing a dipole oscillation of amplitude A perpendicular to the surface and centered on the surface. The incident velocity was varied from 1–8 mm/s by adjusting A. (b) Atoms were loaded into a surface trap with zero incident velocity using an intermediate trap located at $A/2$. Atoms initially confined at a distance A from the surface were made to undergo a dipole oscillation of amplitude $A/2$ by shifting the trap center halfway to the surface. After holding for half a trap period, $T_\perp/2$, the atoms were incident on the surface with near zero velocity. The trap center was again shifted by $A/2$ towards the surface, trapping the atoms against the Si wafer. To ensure contact between atoms and the surface, the center of the final trap was located $\sim$10% of the original condensate size beyond the Si surface.
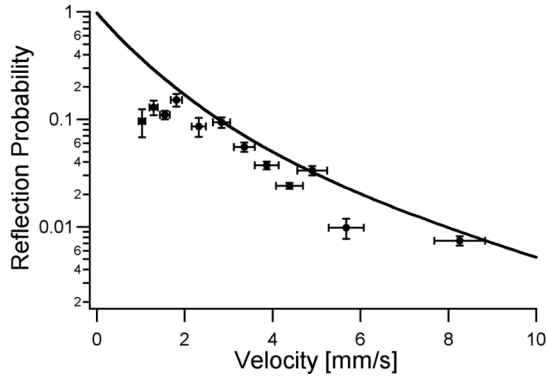
FIG. 3.   Reflection probability vs incident velocity. Data were collected in a magnetic trap with trap frequencies $2\pi \times (3.3, 2.5, 6.5)$ Hz. Incident and reflected atom numbers were averaged over several shots. Vertical error bars show the standard deviation of the mean of six measurements. Horizontal error bars reflect the uncertainty in deducing $v_\perp$ from the applied magnetic field $B_\perp$. The solid curve is a numerical calculation for individual atoms incident on a conducting surface as described in the text.
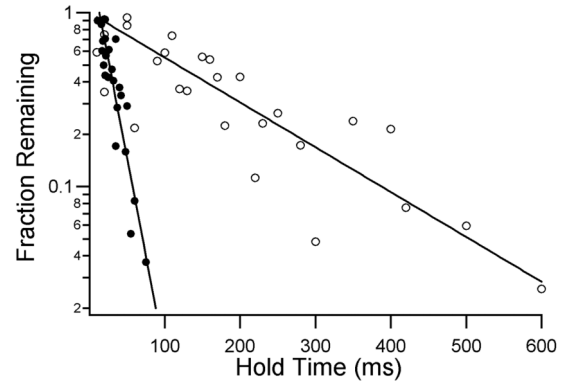

FIG. 4.   Lifetime in the Si surface trap. Solid (open) circles show the remaining atom fraction vs time for a $2\pi \times (9, 9, 6.5)$ [$2\pi \times (3.3, 2.5, 6.5)$] Hz trapping potential with an initial atom number 3×10^4 (9×10^4). The solid line exponential fit gives a lifetime of 23 ms (170 ms) for the high (low) frequency trap geometry. The lifetime for atoms confined far from the surface exceeded 20 s for either geometry.

ratio of reflected atom number to incident atom number, as a function of incident velocity. The reflection probability increases with decreasing velocity, a signature of quantum reflection. Similar behavior was observed for atoms with a peak density of $\sim 7 \times 10^{12}$ cm^{-3} in a $2\pi \times (10.5, 10, 6.5)$ Hz trap. For comparison, we include a line in Fig. 3 showing the calculated reflection probability for a single atom incident on a conducting wall. The reflection probability was obtained by numerically solving the Schrödinger equation with the Casimir-Polder potential using the C_4 coefficient calculated for sodium atoms incident on a conducting surface, $C_4 = 9.1 \times 10^{-56}$ Jm^4 [1] and $\lambda = 590$ nm. This model ignores the harmonic trapping potential, interatomic forces, and electrostatic effects of adsorbed alkali atoms on the surface, which have recently been shown to distort the long-range potential in the case of Rb atoms on insulating surfaces [24,25]. Furthermore, the doped Si surface has a finite conductivity, leading to a reduction in C_4 of order 20%–40% and a slightly higher reflection probability than a perfect conductor [26].

According to the model, reflection of atoms with 2 mm/s velocity occurs at a distance of $\sim 1\ \mu$m from the surface, where the full potential is approximated to within 10% by $U = -C_4/r^4$. The range of velocities we could explore is not large enough to investigate the region closer to the surface where the potential has a $1/r^3$ dependence. It should be noted that without retardation, the reflection probability would be more than a hundred times lower. Ultimately, quantum reflection may be a powerful tool to characterize atom-surface interactions.

We also observe dynamics, not present in single-atom quantum reflection, when a Bose-Einstein condensate is incident on a surface. For incident velocity below 2 mm/s, the measured reflection probability remained

approximately constant between 10% and 15%, in contrast with theoretical predictions and previous observation. This discrepancy may be due to collective excitations of the atoms or acceleration from the harmonic trapping potential during the collision. The shape and density of the reflected atom cloud, as can be seen in Fig. 2(a), were not reproducible from shot to shot. Reflected clouds were excited and sometimes fragmented and higher velocity incident atoms tended to produce more dense reflected clouds, which may imply that an excitation occurred during the collision that was more pronounced at low collision velocities.

Furthermore, the role of the mean-field interaction energy should be considered. When a condensate is released from a trapping potential, the repulsive mean-field energy is converted into kinetic energy, imparting to the atoms an average velocity equal to the local speed of sound, $c = \sqrt{gn/m}$, where $g = 4\pi\hbar^2 a/m$ is the coupling parameter associated with atom-atom interaction, and a is the s-wave scattering length. We expect that the mean-field energy will be released during the collision so that, even for a condensate with zero center of mass velocity, the incident velocity may be characterized by the speed of sound. For Na condensates at a density of 2×10^{12} cm^{-3}, this velocity is ~ 0.6 mm/s.

In the limit of zero incident velocity, a surface acting as an ideal atom mirror could be used to construct a physical container for ultracold atoms and Bose-Einstein condensates. To examine the feasibility of confining atoms with solid surfaces, atoms were held in a magnetic trap divided in half by the Si surface. The transfer procedure is described schematically in Fig. 1(b). Figure 4 shows the remaining fraction of atoms in the trap as a function of hold time for two different magnetic trap parameters, one at high trap frequency, $2\pi \times (9, 9, 6.5)$, and the other at low trap frequency, $2\pi \times (3.3, 2.5, 6.5)$. After an initial

loss due to the nonzero incident velocity (not shown), the atom number was found to decrease exponentially. The lifetime for the high (low) frequency trap was 23 ms (170 ms). We attribute the losses of atoms to scattering with the surface and adsorption. Fluctuating electromagnetic fields in a (semi)conductor can also induce losses of atoms due to thermally induced spin flips (see, e.g., Ref. [25]). However, at the large magnetic bias field of ~ 10 G, atoms can be ejected from the trap only with fields of frequency ~ 7 MHz. At an average distance of ~ 15 μm from surface, the spin flip decay rate should not exceed 0.1 μHz, a negligible effect in the present experiment and not a significant limitation for future ones.

In order to estimate the effect of quantum reflection on the lifetime of atoms in the trap, we assume that the atoms are incident on the surface with a velocity proportional to the speed of sound in the condensate and that the geometry of the trapped atom cloud is independent of the trap frequency. The atom loss rate to the surface may be expressed as $dN/dt \propto -nSc(1 - R)$, where S is the contact area between surface and condensate. From this rate equation, we express the lifetime as $\tau_L = -N/(dN/dt) = \chi T_\perp/(1 - R)$, where χ is an undetermined numerical parameter independent of the trap frequency. An identical equation would describe a thermal cloud of atoms. Comparing the ratio $\tau_L/T_\perp$ for the two different trap frequencies, we cancel out the constant χ. Assuming the reflection probability for the high-frequency trap, $R_h = 0$, gives a value of $R_l = 60\%$ for the low-frequency trap reflection probability. A more reasonable assumption of $R_h = 20\%$ gives a value of $R_l = 70\%$.

The results presented here demonstrate that large quantum reflection probability is not confined to exotic surfaces or extreme angles of incidence: a simple silicon wafer at room temperature can function as an atomic mirror at normal incidence, reflecting ultracold atoms. The construction of practical atom-optical devices based on normal-incidence quantum reflection requires even higher reflection probabilities than demonstrated in this work. Such improvements are predicted for low-density and extremely thin surfaces [4], and have been observed with patterned surfaces, where a reduction in surface density by etching increased the maximum reflection probability by a factor of 2 [11]. Because reflection occurs far from the surface, uniformity of the surface is not a critical factor, as roughness is averaged over the atomic wavelength.

Surfaces are traditionally considered enemies of cold atoms: laser cooling and atom optics have developed thanks to magnetic and optical traps that confine atoms with nonmaterial walls in ultrahigh vacuum environments designed to prevent contact with surfaces. Paradoxically, it turns out that in the extreme quantum limit of nanokelvin matter waves, a surface at room temperature might become a useful device to manipulate atoms.

---

*Electronic address: http://cua.mit.edu/ketterle_group/

[1] H. B. G. Casimir and P. Polder, Phys. Rev. **73**, 360 (1948).
[2] D. P. Clougherty and W. Kohn, Phys. Rev. B **46**, 4921 (1992).
[3] C. Carraro and M. W. Cole, Prog. Surf. Sci. **57**, 61 (1998).
[4] A. Mody, M. Haggerty, J. M. Doyle, and E. J. Heller, Phys. Rev. B **64**, 085418 (2001).
[5] H. Friedrich, G. Jacoby, and C. G. Meister, Phys. Rev. A **65**, 032902 (2002).
[6] V. U. Nayak, D. O. Edwards, and N. Masuhara, Phys. Rev. Lett. **50**, 990 (1983).
[7] J. J. Berkhout *et al.*, Phys. Rev. Lett. **63**, 1689 (1989).
[8] J. M. Doyle *et al.*, Phys. Rev. Lett. **67**, 603 (1991).
[9] I. A. Yu *et al.*, Phys. Rev. Lett. **71**, 1589 (1993).
[10] A. Anderson *et al.*, Phys. Rev. A **34**, 3513(R) (1986).
[11] F. Shimizu, Phys. Rev. Lett. **86**, 987 (2001).
[12] F. Shimizu and J. Fujita, J. Phys. Soc. Jpn. **71**, 5 (2002).
[13] F. Shimizu and J. I. Fujita, Phys. Rev. Lett. **88**, 123201 (2002).
[14] V. Druzhinina and M. DeKieviet, Phys. Rev. Lett. **91**, 193202 (2003).
[15] A. Landragin *et al.*, Phys. Rev. Lett. **77**, 1464 (1996).
[16] B. Segev, R. Cote, and M. G. Raizen, Phys. Rev. A **56**, 3350(R) (1997).
[17] J. P. Dowling and J. Gea-Banacloche, Adv. At. Mol. Opt. Phys. **37**, 1 (1996).
[18] E. A. Hinds and I. G. Hughes, J. Phys. D **32**, R119 (1999).
[19] A. E. Leanhardt *et al.*, Science **301**, 1513 (2003).
[20] C. R. Monroe, Ph.D. thesis, University of Colorado, Boulder, 1992.
[21] The trap center to surface separation exhibited a linear dependence on $B_\perp$. The relative position of the surface was determined by loading a condensate into the trap, slowly moving the trap center toward the surface, holding for several trap periods, and measuring the remaining atom number. As the separation became smaller than the condensate radius, atoms were lost from the trap due to adsorption on the surface. The surface position was the point at which no atoms remained in the trap, and was in good agreement with the visual location of the surface determined by imaging. The position of the surface was determined to within a 10 μm.
[22] O. J. Luiten *et al.*, Phys. Rev. Lett. **70**, 544 (1993).
[23] D. M. Harber, J. M. McGuirk, J. M. Obrecht, and E. A. Cornell, J. Low Temp. Phys. **133**, 229 (2003).
[24] J. M. McGuirk, D. M. Harber, J. M. Obrecht, and E. A. Cornell, Phys. Rev. A **69**, 062905 (2004).
[25] Y. J. Lin, I. Teper, C. Chin, and V. Vuletic, Phys. Rev. Lett. **92**, 050404 (2004).
[26] Z. C. Yan, A. Dalgarno, and J. F. Babb, Phys. Rev. A **55**, 2882 (1997).

Appendix C

Low velocity quantum reflection of Bose-Einstein condensates

P H Y S I C A L   R E V I E W   L E T T E R S

Low Velocity Quantum Reflection of Bose-Einstein Condensates

T. A. Pasquini, M. Saba, G.-B. Jo, Y. Shin, W. Ketterle, and D. E. Pritchard

Department of Physics, MIT-Harvard Center for Ultracold Atoms, and Research Laboratory of Electronics,
*Massachusetts Institute of Technology, Cambridge, Massachusetts 02139, USA**

T. A. Savas

NanoStructures Laboratory and Research Laboratory of Electronics, Massachusetts Institute of Technology,
Cambridge, Massachusetts 02139, USA

N. Mulders

Department of Physics, University of Delaware, Newark, Delaware 19716, USA

We study how interactions affect the quantum reflection of Bose-Einstein condensates. A patterned silicon surface with a square array of pillars resulted in high reflection probabilities. For incident velocities greater than 2.5 mm/s, our observations agreed with single-particle theory. At velocities below 2.5 mm/s, the measured reflection probability saturated near 60% rather than increasing towards unity as predicted by the accepted theoretical model. We extend the theory of quantum reflection to account for the mean-field interactions of a condensate which suppresses quantum reflection at low velocity. The reflected condensates show collective excitations as recently predicted.

Recent years have seen an explosive growth of experiments with cold atoms near surfaces, driven by the desire to miniaturize atomic physics experiments using so-called ''atom chips'' [1], for practical applications in magnetometry [2] and atom interferometry [3]. The Casimir-Polder interaction becomes important close to the surface an atom chip [4–6] and offers both fundamental and technical relevance. Fundamental studies include the use of Bose-Einstein condensates to determine the Casimir-Polder potential [7,8], to observe its modification by thermal radiation [9], and the intriguing question if unity quantum reflection can be achieved at extremely low temperatures. Quantum reflection is the phenomena by which an atom is accelerated so violently by the attractive surface potential that it reflects from the potential rather than being drawn into the surface [10–13]. Current models of quantum reflection treat the atom-surface interaction as a single-atom potential, and predict a monotonic rise to unity reflection at zero velocity. However, in a recent study of quantum reflection of Bose-Einstein condensates (BECs) [14], the reflection probability saturated at ∼12% at low velocity [15]. A Letter simulating quantum reflection of BECs demonstrated excitations during reflection as a result of mean-field interactions but could not explain the low reflectivity [16].

In this work, we address how quantum reflection of BECs differs from the reflection of single atoms and discuss the role of interatomic interactions before, during, and after reflection. Compared to our previous study, where some effects of interactions were already observed but not characterized or explained [14], we are now more sensitive, having improved the reflection probability to 67% by

using a pillared silicon surface, in the spirit of experiments with grazing-incidence neon atoms on ridged silicon [17–19]. In contrast to single-particle theory, we observe a saturation of the reflection probability at low incident velocity, suggesting that the description of quantum reflection is incomplete. We propose a simple theoretical extension incorporating a mean-field potential which is found to dramatically suppress the reflection probability near zero velocity. Further, we observe that interactions between the incident and reflected condensate lead to predicted collective excitations of the reflected condensate [16] and incoherent scattering.

Bose-Einstein condensates of ^{23}Na atoms were prepared and transferred into a loosely confining gravitomagnetic trap, comprising a single coil and three external bias fields, as described in Ref. [20]. For typical loading parameters, condensates with $N \approx 1 \times 10^6$ atoms were confined ∼1 cm above the coil in a harmonic trap characterized by angular frequencies $(\omega_\perp, \omega_y, \omega_z) = 2\pi \times (4.2, 5.0, 8.2)$ Hz, where directions $(\perp, y, z)$ are defined in Fig. 1. At this point, $\omega_\perp$ and ω_y were adjusted by changing the vertical bias field as described in Ref. [20]. Typical densities in the trap were ∼5×10^{12} cm^{-3} and diameters were ∼150 μm. A silicon surface attached to a micrometric, motorized linear actuator was mounted ∼1 cm above the single coil. The position of the surface relative to the center of the coil was adjustable during the experiment as shown in Fig. 1(a).

The surface used in this experiment, provided by the MIT Nanostructures Laboratory, was a pillar structure etched into single-crystal silicon. The structure was created by interference lithography and various subsequent etching
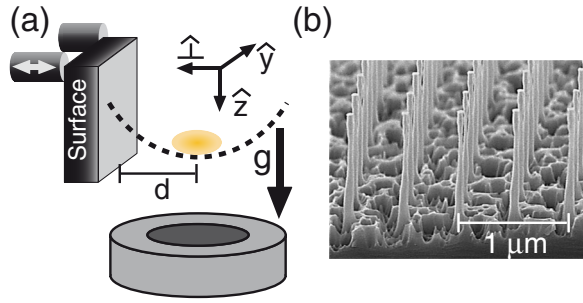
FIG. 1 (color online). Experimental schematic. (a) Atoms were confined in a gravitomagnetic trap near a pillared Si surface. Atoms were accelerated towards the surface by displacing the trapping potential a distance d (greatly exaggerated) so that it was centered on the surface. The surface was mounted on a translation stage and could be removed at any point for imaging. (b) Scanning electron micrograph of the pillared Si surface used in this experiment.

steps [21–23]. Figure 1(b) shows the final surface as an array of 1 μm tall, 50 nm diameter pillars spaced at 500 nm. Such a surface should provide a Casimir potential approximately 1% of the value for a solid Si surface. A dilute surface is expected to exhibit enhanced quantum reflection.

Studying the reflection properties of the surface requires a controlled collision. After loading the condensate into the trap, the surface was moved to a desired distance d from the trap center. By changing the bias field $B_\perp$ appropriately, a dipole oscillation centered on the surface was induced [14]. After waiting $T_\perp/4 = 2\pi/4\omega_\perp$ the atoms hit the surface with velocity $v_\perp = d\omega_\perp$. By varying $\omega_\perp$ between $2\pi \times 2$ and $2\pi \times 4$ Hz and d over 50 μm to 1 mm, velocities in the range of 0.5 to 26 mm/s could be studied. The reflection probability was calculated as the ratio of the average reflected atom number to the average incident atom number [24]. The reflection probability along with data for a solid silicon surface [14] are shown in Fig. 2. The pillared surface shows higher reflectivity over a wider range of incident velocity, as expected. The reflection maximum is 67% for a velocity of 1.2 mm/s, and reflection probabilities above 10% were measured at velocities up to 20 mm/s. Below ~3 mm/s, the reflection probability flattens near 55%, qualitatively similar to the behavior of the solid surface where the reflectivity flattened near 12% in the same velocity range.

Reflection probabilities for a single atom were calculated by numerically solving the Schrödinger equation for a 1D potential [25]. The surface potentials of the Casimir-Polder form C_4/r^4 are obtained using $C_4^{Si} = 6.2 \times 10^{-56}$ J m^4 for bulk silicon [26] and combining contributions from both the pillar layer and the bulk substrate. We average the density of the material before calculating the potential, simulating the surface as a 1 μm thick overlayer of material with $C_4 = 0.01 \times C_4^{Si}$ added to a semi-infinite slab of material with $C_4 = C_4^{Si}$. The resulting reflection probability curve is shown in Fig. 2 as dashed gray lines. A
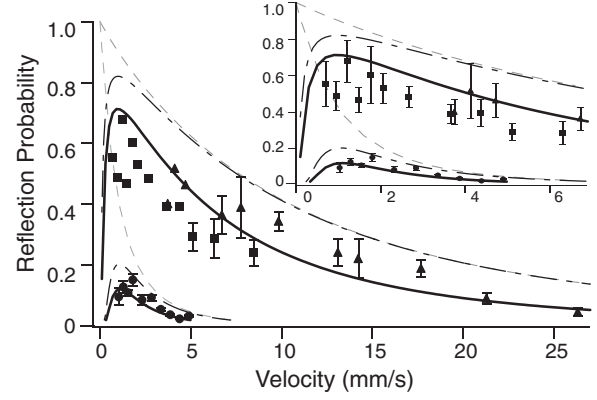

FIG. 2. Reflection probability vs incident velocity. Data were collected in a magnetic trap with trap frequencies $2\pi \times (2.0, 2.5, 8.2)$ Hz (squares) and $2\pi \times (4.2, 5.0, 8.2)$ Hz (triangles). For comparison, data from Ref. [14] for reflection off a solid silicon surface are shown as circles. Incident and reflected atom numbers were averaged over several shots. For clarity error bars for data below 5 mm/s are shown only in the inset plot, which has a different horizontal axis to emphasize the low velocity data. Systematic uncertainty in the velocity due to residual motion is approximately 10%. Theoretical curves are described in the text.

model which averages the 3D potential of the pillars to obtain a 1D potential shows similar results. Further, these simulations show that the reflection probability depends mainly on the diluted pillar layer and only weakly on the bulk material underneath or the height or arrangement of the pillars. Unlike grazing-incidence experiments [17–19], here the de Broglie wavelength, $\lambda_{dB} \simeq 1$ μm, exceeds the spacing of the pillars and we are insensitive to the surface structure.

Calculations predict that the reflection probability approaches unity for low incident velocity. This is in contrast to our observation that the reflection probability saturates below 2.5 mm/s for both the pillared and solid surfaces. It was suggested that this saturation is due to low velocity excitations which smear out the condensate density; although the reflectivity approaches unity, some reflected atoms would appear in a diffuse cloud which may fall below a detection threshold [16]. However, this could explain our previous results [14] only when we assume a density threshold for detection of $0.25 \times n_0 \approx 10^{12}$ cm^{-3}, where n_0 is the central condensate density, which is 20 times higher than the lowest densities we are able to detect [20].

There is a finite-size correction to the standard description of quantum reflection, but it is too small to account for our observations. For an incident atom cloud of size d, the smallest incident velocity is h/md, approximately 0.2 mm/s for our parameters. We conclude that a single-particle description cannot account for our low velocity data and now discuss possible effects due to the condensate's mean-field interaction.

The mean-field potential is taken to be that of a condensate at rest with a fully reflecting wall as a boundary

condition. The condensate's density decays towards zero at the wall over a characteristic length scale given by the healing length, ξ. The atoms at the edge of the condensate thereby acquire a velocity given by $\approx h/m\xi$, which is approximately equal to the speed of sound c. If the healing length is much larger than the relevant range of the Casimir-Polder potential, approximately 1 μm as defined by the so-called badlands region [13], one would assume that the mean-field potential simply accelerates the atoms. Atoms leaving the condensate enter the region of quantum reflection with an incident velocity obtained from $mv^2/2 = U = mc^2$. This model would shift the single-atom quantum reflection curves by the velocity $v = \sqrt{2}c$, which is ≈ 1.5 mm/s for our parameters. This shift is too small to explain the low reflectivity at our lowest velocities. Additionally, the assumption that the healing length be much larger than the distance at which quantum reflection occurs is not valid for our data.

In order to fully account for interaction effects, we calculate the quantum reflection probability using a composite potential which includes both the Casimir-Polder potential and the mean-field potential [Fig. 3(a)]. The predicted reflection probability is shown in Fig. 3(b). At high velocities (>3 mm/s), quantum reflection occurs close to the surface where the mean-field potential plays no role. As the velocity is reduced, the point of reflection moves outward, into the region where the mean-field potential "softens" the Casimir-Polder potential, dramatically reducing the reflectivity. At very low velocities (<0.1 mm/s), when the badlands region is far from the surface, the predicted reflection resembles the reflection
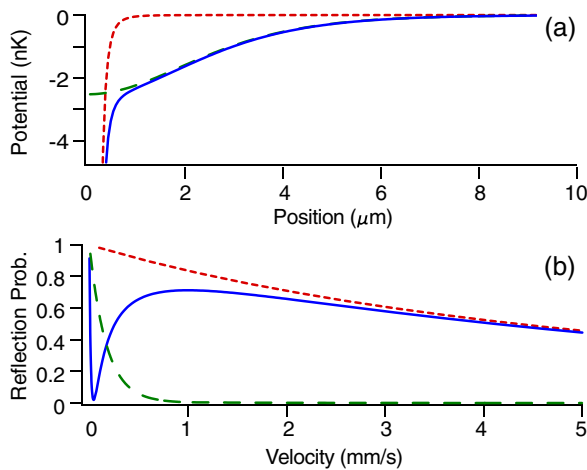

FIG. 3 (color online).   Mean-field model for quantum reflection of condensates. (a) The trapped condensate provides a repulsive mean-field energy which is a constant away from the surface and, within the healing length ξ, drops to zero. The dashed curve shows this mean-field potential set to zero at infinity. This potential combined with the Casimir potential (dotted curve) creates the composite potential (solid curve) which we use to model reflection in the presence of a condensate. (b) The reflection probabilities from the same potentials for low velocities.

probability from the mean-field potential of the condensate rather than from the Casimir-Polder potential and becomes unity at zero velocity [15]. This model predicts well, without any free parameter, the velocities below which we have observed saturation of the reflectivity for both the solid and pillared surface as shown by the dot-dashed lines in Fig. 2. The data do not extend far enough into the very low velocity regime to confirm the model's prediction of a sharp drop.

The model does not include the effects of the moving condensate, its observed collective excitations, or the distortion of the condensate wave function by surface attraction or the loss of atoms to the surface.

The calculated curves are not in quantitative agreement with the experimental data; the observed reflection probabilities are lower, even at high velocity. A possible explanation is the modification of the potential by stray electric fields, caused by sodium atoms deposited on the surface (adatoms). Recently, the partial ionization of rubidium adatoms by bulk silicon has been shown empirically to produce an electric field of several V/cm at 10 μm from the surface [5]. This electric field, which falls off as $1/r^2$, will produce an additional potential, $V_A(r) = -A/r^4$, which will reduce the reflection probability. To account for stray electric fields, we fit the high velocity data for the pillared (solid) surface using a potential $V_{tot} = -0.01 \times C_4^{Si}/r^4 - A/r^4$ ($V_{tot} = -C_4^{Si}/r^4 - A/r^4$). We find for the pillared (solid) surface a value of A of $0.02 \times C_4^{Si}$ (C_4^{Si}) corresponding to a stray field ~ 10 V/cm (~ 70 V/cm) at 1 μm, which scales to 0.1 V/cm (0.7 V/cm) at 10 μm, smaller than measured for rubidium. We may expect a greater factor between the fields measured for a solid and dilute surface owing to the factor of 100 difference in surface area. However, the strength of the fields depends on the specific geometry, surface material, and contamination level, which may vary between the two experiments. Because of experimental limitations, we were not able to confirm the magnitude of these stray fields or their sole responsibility for the observed discrepancy, and include their effect as a phenomenological fitting parameter for the high velocity data.

If we combine the stronger surface potential with the mean-field potential, we have a phenomenological model which is consistent with all our data, shown in Fig. 2 as solid lines. It would be very interesting to test this model by varying the density over a large range and try to observe the predicted decrease of the saturation velocity for lower density. We could not study reflection at lower density due to a rapid decrease of the signal-to-noise ratio.

Another aspect of interactions are collisions between incident and reflected parts of the condensate. This leads to a standing wave during the collision, for a time inversely proportional to the incident velocity. As this time becomes comparable to the transverse and vertical trap periods, vortex rings, solitons, and other excitations may form, distorting the cloud [16]. In our experiment, this veloc-
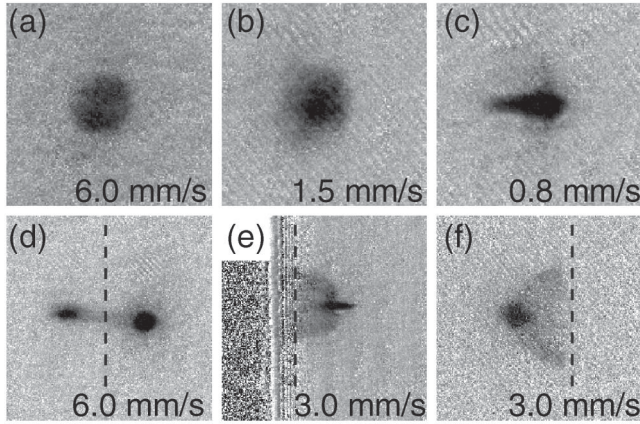
FIG. 4.   Menagerie of reflection effects. (a)–(c) As the incident velocity is reduced, the reflected condensate becomes increasingly excited. (d) By removing the surface at the moment of reflection, we can see both the incident (left) and reflected (right) condensates. The reflection probability is 30%. (e) The collision of the incident and reflected condensates produces a strong *s*-wave scattering halo at low velocity, visible here $T_\perp/4$ after reflection. The surface is still present on the left in this image. Half of the halo is missing due to surface reflection or absorption. (f) With the surface removed, the scattered atoms remain in the trap after an additional half trap period and appear reversed in position and velocity. Field of view for images (a)–(c) is 540 μm and for (d)–(f) is 800 μm; the dashed line is the position of the surface (moved for imaging) at the moment of reflection.

ity is approximately 2 mm/s. The higher reflection efficiency of the pillared surface in excess of 50% allowed us to observe these collective effects. At high velocities (>4 mm/s), we observe that the reflected cloud appears, apart from diminished size and number, similar to the bimodal distribution of the incident cloud, shown in Fig. 4(a). As the incident velocity is reduced, as in Figs. 4(b) and 4(c), the cloud develops a complex surface mode excitation [27].

Further, we observe elastic *s*-wave scattering between atoms in the incident and reflected condensates leading to halos [28,29], which we observe after a hold time $T_\perp/4$ [Figs. 4(e) and 4(f)].

We also performed the experiment using an aerogel surface. Aerogels are electrically insulating, randomly structured, silica foams with a density of $\sim$2% of bulk silica [30] and should display reflection properties similar to the pillared surface. We were unable to observe quantum reflection above our detection threshold of $\sim$2%, an effect we attribute to uncontrolled patch charges which strongly distort the Casimir-Polder potential.

We conclude with an outlook on how to further increase the reflection probability for condensates. Our model predicts improvements for longer healing lengths. Improvements to the reflectivity could also be made by further

reducing the density of the surface and would require further advances in fabrication techniques.

*Electronic address: http://cua.mit.edu/ketterle_group/
 [1] R. Folman *et al.*, Adv. At. Mol. Opt. Phys. **48**, 263 (2002).
 [2] S. Wildermuth *et al.*, Nature (London) **435**, 440 (2005).
 [3] Y. Shin *et al.*, Phys. Rev. A **72**, 021604(R) (2005).
 [4] D. M. Harber *et al.*, J. Low Temp. Phys. **133**, 229 (2003).
 [5] J. M. McGuirk *et al.*, Phys. Rev. A **69**, 062905 (2004).
 [6] Y. J. Lin *et al.*, Phys. Rev. Lett. **92**, 050404 (2004).
 [7] D. M. Harber *et al.*, Phys. Rev. A **72**, 033610 (2005).
 [8] H. Oberst *et al.*, Phys. Rev. A **71**, 052901 (2005).
 [9] M. Antezza, L. P. Pitaevskii, and S. Stringari, Phys. Rev. Lett. **95**, 113202 (2005).
[10] D. P. Clougherty and W. Kohn, Phys. Rev. B **46**, 4921 (1992).
[11] C. Carraro and M. W. Cole, Prog. Surf. Sci. **57**, 61 (1998).
[12] A. Mody *et al.*, Phys. Rev. B **64**, 085418 (2001).
[13] H. Friedrich, G. Jacoby, and C. G. Meister, Phys. Rev. A **65**, 032902 (2002).
[14] T. A. Pasquini *et al.*, Phys. Rev. Lett. **93**, 223201 (2004).
[15] The reflection probability $\sim$50%, inferred by measuring the lifetime of atoms confined against a silicon surface [14], may be a result of reflection from the mean-field potential at the edge of the condensate rather than from the Casimir-Polder potential of the surface.
[16] R. G. Scott *et al.*, Phys. Rev. Lett. **95**, 073201 (2005).
[17] F. Shimizu and J. Fujita, J. Phys. Soc. Jpn. **71**, 5 (2002).
[18] H. Oberst *et al.*, Phys. Rev. Lett. **94**, 013203 (2005).
[19] D. Kouznetsov and H. Oberst, Phys. Rev. A **72**, 013617 (2005).
[20] A. E. Leanhardt *et al.*, Science **301**, 1513 (2003).
[21] H. I. Smith *et al.*, J. Vac. Sci. Technol. B **9**, 2992 (1991).
[22] M. L. Schattenburg, R. J. Aucoin, and R. C. Fleming, J. Vac. Sci. Technol. B **13**, 3007 (1995).
[23] T. A. Savas *et al.*, J. Vac. Sci. Technol. B **14**, 4167 (1996).
[24] Atom numbers were obtained by optically pumping the atoms from the state $|F = 1\rangle$ to $|F = 2\rangle$. After a wait time of $\sim$2 ms to allow optically dense regions of the cloud to expand, the distributions were imaged using the $|F = 2\rangle$ to $|F = 3\rangle$ cycling transition.
[25] F. Shimizu, Phys. Rev. Lett. **86**, 987 (2001).
[26] Z. C. Yan, A. Dalgarno, and J. F. Babb, Phys. Rev. A **55**, 2882 (1997).
[27] A movie of reflection is available at http://cua.mit.edu/ketterle_group/Animation_folder/QRMovie.wmv.
[28] K. Gibble, S. Chang, and R. Legere, Phys. Rev. Lett. **75**, 2666 (1995).
[29] A. P. Chikkatur *et al.*, Phys. Rev. Lett. **85**, 483 (2000).
[30] J. Fricke and A. Emmerling, J. Am. Ceram. Soc. **75**, 2027 (1992).

Appendix D

Pillared surface Mathematica code

The following Mathematica code was used to generate the various models of the pillared surface.

The potential of a pillar

Evaluation of a 3D pillar at a point

Define the size of the pillar in nanometers. Zero is defined at the bottom center of the pillar. Integrate over the regions that have material; assume cylindrical symmetry. The expression to integrate is the atom-atom interaction potential.

```
widx=50;  widy=50; widz=1000;
ToIntegrate[x,y,z]=(x*x+y*y+z*z)^(-7/2);
OneIntegral[y,z]=Integrate[2*ToIntegrate[x,y,z],{x,0,widx/2}];
TwoIntegral[y_,zpos_]=Integrate[OneIntegral[y,z],{z,zpos-widz,zpos}];
OnePillar[ypos_,zpos_]:=
          Integrate[TwoIntegral[y,zpos],{y,ypos-widy/2,ypos+widy/2}]
```

Calculation of the pillar potential on a grid

The potential should not be calculated inside of the pillar. The potential will only be calculated in a quarter plane (with the pillar defining the space). Data are stored in an array for later retrieval. This section is repeated for the medium grid size where GridSizeNano=50, GridMaxY=5000, and GridMaxZ=12000. The arrays must be padded for use later; the space left by the pillar must be filled.

```
GridSizeNano=5;  GapSize=25;
GridMaxY=500;  GridMaxZ=2000;  k=1;
PillarPotentialArray=Table[0,{y,NEvalPts},{x,3}];
```

```
CalculatePotentialAtThePoint:={
     PillarPotentialArray[[k,1]]=yposeval;
     PillarPotentialArray[[k,2]]=zposeval;
     PillarPotentialArray[[k,3]]=N[OnePillar[yposeval,zposeval]];
     k++};
For[ny=0,ny<=GridMaxY,
     For[nz=0,nz<=GridMaxZ,
          yposeval=ny;
          zposeval=nz;
          If[((yposeval>(widy+GapSize))||(zposeval>(widz+GapSize)))
               CalculatePotentialAtThePoint,dummy=0];
     nz=nz+GridSizeNano];
ny=ny+GridSizeNano];
Export["C:\PillarPotentialSmall.dat", PillarPotentialArray];
```

Conversion factors and constants

The original integrals were done with C4=1 and the grid in nm.

```
C4=4.48*10^(-33);
ConvertToKelvin=(10/pi)*C4*10^(36);
ConvertToNm=.00529;
ConvertToAu=1/ConvertToNm;
ConvertDegKToHartree=3.16681*10^(-6);
ConvertToHartree=ConvertToKelvin*ConvertDegKToHartree;
m=22.99*1.66 10^-27/(9.11*10^-31);
v0=2.9979*10^8/137;
rref=2.3 10^-9/(5.29*10^-11);
lengthscale=945.18;
Maxval=80/lengthscale;
```

Interpolation of numerical data to give potential at any point

Numeric results for the single pillar are only good to around 5 μm. For a given position, the correct array must be interpolated.

```
PotentialSmall=Interpolation[PillarPotentialSmall];
PotentialMedium=Interpolation[PillarPotentialMedium];
GetPotential[yeval_,zeval_]:= If[((yeval>500)||(zeval>1500)),
     ConvertToHartree*PotentialMedium[yeval,zeval],
```

```
            ConvertToHartree*PotentialSmall[yeval,zeval]]
PillarPotential[xpos_,ypos_,zpos_]:=
        If[((((Sqrt[xpos*xpos+ypos*ypos]*ConvertToNm)<5000)
            &&(zpos*ConvertToNm<10000)
            &&(((Sqrt[xpos*xpos+ypos*ypos]*ConvertToNm)>100)
            ||(zpos*ConvertToNm>1050))),
            GetPotential[(Sqrt[xpos*xpos+ypos*ypos]*ConvertToNm),
            zpos*ConvertToNm],0];
```

PlusFullPotentialLg gives the potential of a pillar array plus the background surface

```
PillarArray=Table[x,{x,1,441},{y,0,1}];
kk=1;
For[ii=-10,ii<=10,
    For[jj=-10,jj<=10,
        PillarArray[[kk, 1]]=ii;
        PillarArray[[kk, 2]]=jj;
        kk++;
        jj++];
    ii++];
PillarArray=PillarArray*500*ConvertToAu;
PlusFullPotentialLg[xfull_,yfull_,zfull_]:={
    PointArray=PillarArray+Table[{xfull,yfull},
        {dummy,1,Dimensions[PillarArray][[1]]}];
    CurrentValue=ConvertDegKToHartree*C4*ConvertToAu^(4)
        /mToNmConv^(4)*zfull^(4);
    For[n=1,n<=Dimensions[PillarArray][[1]],
    CurrentValue=CurrentValue+
        PillarPotential[PointArray[[n,1]],PointArray[[n,2]],zfull];
        n++];
    CurrentValue}[[1]]
```

Calculation of the line potentials

For the reflection calculations, we cannot use an interpolating function, so a fitting routine must be constructed to accurately mimic the potential. This is the most critical part of the full calculation.

Potential for solid silicon and reduced density

```
potold[r_]=-ConvertDegKToHartree*C4*ConvertToAu^(4)
          /(mToNmConv)^(4)r^(4);
potoldsmall[r_]=-0.01*ConvertDegKToHartree*C4
               *ConvertToAu^(4)/(mToNmConv)^(4)r^(4);
```

Fitting the potential

The selection of line potentials and fitting routine. Calculating reflection probabilities for each of these line potentials gives the average reflection model. Point values are weighting factor, xposition, yposition. The average potential is made by creating a running tally in the loop; the result is given below.

```
PointValues = {{1/8,0,0},{1/2,50,0},{1/2,50,50},{1/2,100,0},
   {1,100,50},{1/2,100,100},{1/2,150,0},{1,150,50},{1,150,100},
   {1/2,150,150},{1/2,200,0},{1,200,50},{1,200,100},{1,200,150},
   {1/2,200,200},{1/4,250,0},{1/2,250,50},{1/2,250,100},
   {1/2,250,150},{1/2,250,200},{1/8,250,250}};
<< Statistics`NonlinearFit`
For[nnnn=1,nnnn<=21,
   xvalue=PointValues[[nnnn,2]]*ConvertToAu;
   yvalue=PointValues[[nnnn,3]]*ConvertToAu;
   LinePot=
    Table[PlusFullPotentialLg[xvalue,yvalue,z],
         {z,1100*ConvertToAu,8000*ConvertToAu,50*ConvertToAu}];
   TrialFit=NonlinearFit[Log[LinePot],
      theta0+theta1*x+theta2*(x + theta12)^2+theta3*(x+theta13)^3+
        theta4*(x+theta14)^4+theta5*(x+theta15)^5+
        theta6*(x+theta16)^(-1)+theta7*(x+theta17)^(-2),
      x,{theta0,theta1,theta2,theta12,theta3,theta13,theta4,
      theta14,theta5,theta15,theta6,theta16,theta7,theta17},
      MaxIterations -> 8000];
  nnnn++;]
averagepot[x_]=-Exp[-75.65-6865/(-1628+x)-0.1143x+0.0003988x^2
                   -9.113*^-7 x^3+207.9(4.705+x)^(-2)];
```

Calculate reflection probability (C. Sanner)

```
reflprob[velocity_]:={k=m*velocity/(1000 v0);
```

```
p[r_]=Sqrt[k^2-2m*pot[r*lengthscale]];
psiwkb[r_]:=1/Sqrt[p[r]]*Exp[-I*NIntegrate[p[rr],{rr,rref,r}]];
solution =NDSolve[{k^2/(2m)psi[r]+psi''[r]/(2 m)-
                pot[r*lengthscale] psi[r] == 0,
            psi[rref+1]==psiwkb[rref+1],
            psi[rref+3]==psiwkb[rref+3]},psi,{r,rref,75000},
          MaxSteps->8000];
approx = Fit[Table[{r,Evaluate[psi[r]/. solution]},
            {r,45000,75000,1000}], {Exp[-I*k*r],Exp[I*k*r]},r];
Abs[approx[[1,2,1]]/approx[[1,1,1]]]^2}[[1]]
```

Appendix E

Technical drawings

A custom flange for the science chamber provides optical access along all three chamber axes and ports for (1) a linear actuator and (2) various electrical feedthroughs. MDC Vacuum adapted part number MAF600-6-133T (409006) according to the following design.
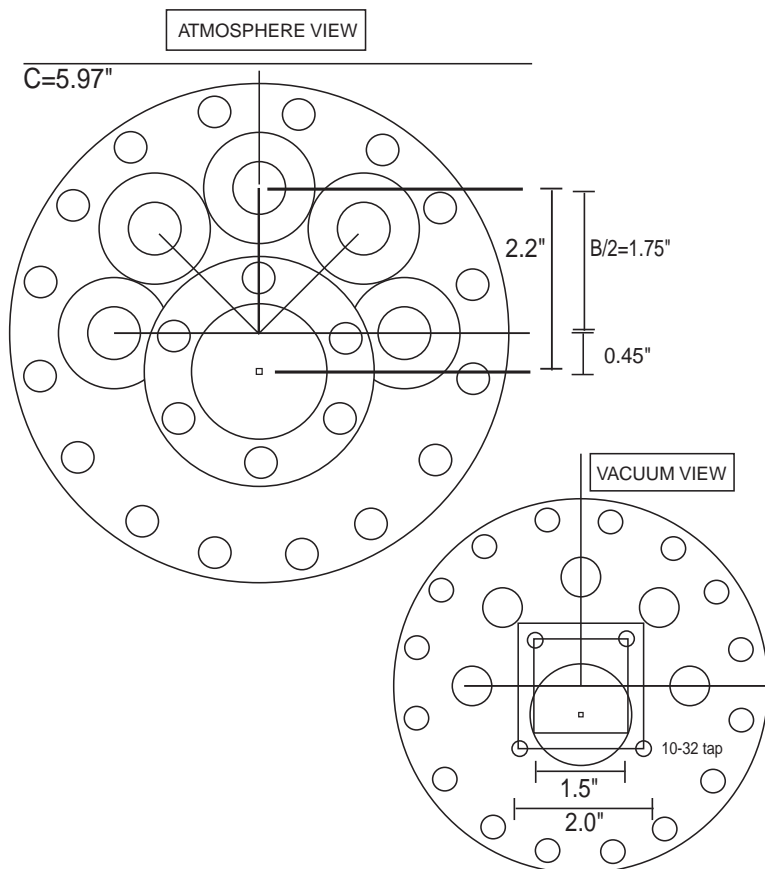
Bibliography

[1] C. G. Aminoff, A. M. Steane, P. Bouyer, P. Desbiolles, J. Dalibard, and C. Cohen-Tannoudji. Cesium atoms bouncing in a stable gravitational cavity. *Physical Review Letters*, 71:3083, 1993.

[2] A. Anderson, S. Haroche, E. A. Hinds, W. Jhe, D. Meschede, and L. Moi. Reflection of thermal Cs atoms grazing a polished glass surface. *Physical Review A*, 34:3513–3516, 1986.

[3] M. R. Andrews, C. G. Townsend, H. G Miesner, D. S. Durfee, D. M. Kurn, and W. Ketterle. Observation of interference between two bose condensates. *Science*, 301:1513–1515, 2003.

[4] J. R. Anglin and W. Ketterle. Bose-Einstein condensation of atomic gasses. *Nature*, 416:211, 2002.

[5] M. Antezza. Surface-atom force out of thermal equilibrium and its effect on ultra-cold atoms. *Journal of Physics A*, 39:6117, 2006.

[6] M. Antezza, L. P. Pitaevskii, and S. Stringari. Effect of the Casimir-Polder force on the collective oscillations of a trapped Bose-Einstein condensate. *Physical Review A*, 70:053619, 2004.

[7] M. Antezza, L. P. Pitaevskii, and S. Stringari. New asymptotic behavior of the surface-atom force out of thermal equilibrium. *Physical Review Letters*, 95:113202, September 2005.

[8] M. Ashby, T. Evans, N. A. Fleck, L. J. Gibson, J. W. Hutchinson, and H. N. G. Wadley. *Metal Foams: A design guide*. Butterworth-Heinemann, 2000.

[9] N. W. Ashcroft and N. D. Mermin. *Solid State Physics*. Brooks/Cole, 1976.

[10] J. F. Babb. Private communication. 2005.

[11] J. F. Babb, G.L. Klimchitskaya, and V. M. Mostepanenko. Casimir-Polder interaction between an atom and a cavity wall under the influence of real conditions. *Physical Review A*, 70:042901, 2004.

[12] T. Bergeman, G. Erez, and H. J. Metcalf. Manetostatic trapping fields for neutral atoms. *Physical Review A*, 35:1535, 1987.

[13] J. J. Berkhout, O. J. Luiten, I. D. Setija, T. W. Hijmans, T. Mizusaki, and J. T. M. Walraven. Quantum reflection: focusing of hydrogen atoms with a concave mirror. *Physical Review Letters*, 63:1689, 1989.

[14] J. J. Berkhout, E. J. Wolters, R. van Roijen, and J. T. M. Walraven. Vanishing sticking probabilities and enhanced capillary flow of spin-polarized hydrogen. *Physical Review Letters*, 57:2387, 1986.

[15] M. V. Berry and K. E. Mount. Semiclassical approximations in wave mechanics. *Reports on Progress in Physics*, 35:315, 1972.

[16] M. Boyd. *Novel trapping techniques for shaping Bose-Einstein condensates.* PhD thesis, MIT, 2006.

[17] G. Brassard, I. Chuang, S. Lloyds, and C. Monroe. Quantum computing. *Proceeding of the National Academy of Sciences*, 95:11032, 1998.

[18] C. E. Campbell, E. Krotscheck, and M. Saarela. Quantum sticking, scattering, and transmission of ^{4}He atoms from superfluid ^{4}He surfaces. *Physical Review Letters*, 80:2169, 1998.

[19] G. K. Campbell, J. Mun, M. Boyd, P. Medley, A. E. Leanhardt, L. Marcassa, D. E. Pritchard, and W. Ketterle. Imaging the Mott insulator shells by using atomic clock shifts. *Science*, 313:649, 2006.

[20] A. O. Caride, G. L. Klimchitskaya, V. M. Mostepanenko, and S. I. Zanette. Dependences of the van der Waals atom-wall interaction on atomic and material properties. *Physical Review A*, 71:042901, 2005.

[21] O. Carnal, M. Sigel, T. Sleator, H. Takuma, and J. Mlynek. Imaging and focusing atoims by a Fresnel zone plate. *Physical Review Letters*, 67:3231, 1991.

[22] C. Carraro and M. W. Cole. Sticking coefficient at ultralow energy: quantum reflection. *Progress in Surface Science*, 57:61–93, 1998.

[23] H. B. G. Casimir and P. Polder. The influence of retardation on the London-van der Waals force. *Physical Review*, 73:360, 1948.

[24] J. K. Chen. *All of your base.* PhD thesis, MIT, 2007.

[25] A. P. Chikkatur. *Colliding and moving Bose-Einstein condensates: Studies of superfluidity and optical tweezers for condensate transport.* PhD thesis, MIT, 2002.

[26] A. P. Chikkatur, A. Görlitz, D. M. Stamper-Kurn, S. Inouye, S. Gupta, and W. Ketterle. Suppression and enhancement of impurity scattering in a Bose-Einstein condensate. *Physical Review Letters*, 85:483, 2000.

[27] A. P. Chikkatur, Y. Shin, A. E. Leanhardt, D. Kielpinski, E. Tsikata, T. L. Gustavson, D. E. Pritchard, and W. Ketterle. A continuous source of Bose-Einstein condensed atoms. *Science*, 296:2193, 2002.

[28] J. K. Chin, D. E. Miller, Y. Liu, C. Stan, W. Setiawan, C. Sanner, K. Xu, and W. Ketterle. Evidence for superfluidity of ultracold fermions in an optical lattice. *Nature*, 443:961, 2006.

[29] D. P. Clougherty. Anomalous threshold laws in quantum sticking. *Physical Review Letters*, 91:226105, 2003.

[30] D. P. Clougherty and W. Kohn. Quantum theory of sticking. *Physical Review B*, 46(8):4921, August 1992.

[31] C. Cohen-Tannoudji, J. Dupont-Roc, and G. Grynberg. *Atom-Photon Interactions.* John Wiley & Sons, 1992.

[32] E. A. Cornell and C. E. Wieman. Bose-Einstein condensation in a dilute gas, the first 70 years and some recent experiments. *Reviews of Modern Physics*, 74:875, 2002.

[33] R. Cote, B. Segev, and M. G. Raizen. Retardation effects on quantum reflection from an evanescent-wave atomic mirror. *Physical Review A*, 58:3999, 1998.

[34] M. Cristiani, O. Morsch, N Malossi, M. Jona-Lasinio, M. Anderlini, E. Courtade, and E. Arimondo. Instabilities of a Bose-Einstein condensate in a periodic potential: an experimental investigation. *Physical Review A*, 69:033605, 2004.

[35] F. Dalfovo, S. Giorgini, L. P. Pitaevskii, and S. Stringari. Theory of Bose-Einstein condensation in trapped gasses. *Reviews of Modern Physics*, 71:463, 1999.

[36] P. C. W. Davies and D. S. Betts. *Quantum Mechanics.* Chapman & Hall, 2 edition, 1984.

[37] B. DeMarco. *Quantum degenerate Fermi gas.* PhD thesis, University of Colorado, Boulder, 2001.

[38] A. Derevianko, W. R. Johnson, M. S. Safronova, and J. F. Babb. High-precision calculations of dispresion coefficients, static dipole polarizabilities and atom-wall interaction constants for alkali-metal atoms. *Physical Review Letters*, 82:3589, 1999.

[39] K. Dieckmann, C. A. Stan, S. Gupta, Z. Hadzibabic, C. H. Schunck, and W. Ketterle. Decay of an ultracold fermionic lithium gas near a feshbach resonance. *Physical Review Letters*, 89:203201, 2002.

[40] R. B. Doak, R. E. Grisenti, S. Rehbein, G. Schmahl, J. P. Toennies, and Ch. Woll. Towards realization of an atomic de Broglie microscope: Helium atom focusing using Fresnel zone plates. *Physical Review Letters*, 83:4229, 1999.

[41] J. M. Doyle, J. C. Sandberg, I. A. Yu, C. L. Cesar, D. Kleppner, and T. J. Greytak. Hydrogen in the submillikelvin regime: sticking probability on superfluid 4He. *Physical Review Letters*, 67(5):603, July 1991.

[42] V. Druzhinina and M. DeKieviet. Experimental observation of quantum reflection far from threshold. *Physical Review Letters*, 91:193202, 2003.

[43] D. S. Durfee. *Dynamic properties of dilute Bose-Einstein condnesates.* PhD thesis, MIT, 1999.

[44] P. M. Echenique and J. B. Pendry. Reflectivity of liquid ^{4}He surface to ^{4}He atoms. *Physical Review Letters*, 37:561, 1976.

[45] D. O. Edwards and P. P. Fatouros. Theory of atomic scattering at the free surface of liquid ^{4}He. *Physical Review B*, 17:2147, 1978.

[46] D. O. Edwards, P. Faturos, G. G. Ihas, P. Mrozinski, S. Y. Shen, F. M. Gasparini, and C. P. Tam. Specular reflection of ^{4}He atoms fom the surface of liquid ^{4}He. *Physical Review Letters*, 34:1153, 1975.

[47] S. Eriksson, F. Ramirez-Martinez, E. A. Curtis, B. E. Sauer, P. W. Nutter, E. W. Hill, and E. A. Hinds. Micron-sized atom traps made from magneto-optical thin films. *Applied Physics B*, 79:811, 2004.

[48] Wm. R. Even, R. W. Crocker, M. C. Hunter, N. C. Yang, and T. J. Headley. Surface and near-surface structure in carbon microcellular materials produced from organic aerogels and xerogels. *Journal of Non-Crystalline Solids*, 186:191, 1995.

[49] C. Folkard, editor. *Guinness World Records 2005.* Guiness World Records, 2005.

[50] R. Folman, P. Krueger, J. Schmiedmayer, J. Denschlag, and C. Henkel. Microscopic atom optics: from wires to an atom chip. *Advances in Atomic, Molecular, and Optical Physics*, 48:263, 2002.

[51] J. Fortagh, S. Kraft, A. Gunther, C. Truck, P. Wicke, and C. Zimmermann. Perspectives of ultracold atoms trapped in magnetic micro potentials. *Optics Communications*, 243:45, 2004.

[52] J. Fortagh and C. Zimmermann. Magnetic microtraps for ultracold atoms. *Reviews of Modern Physics*, 79:235, 2007.

[53] J. Fricke and A. Emmerling. Aerogels. *Journal of the American Ceramic Society*, 75:2027, 1992.

[54] N. Friedman, R. Ozeri, and N. Davidson. Quantum reflection of atoms from a periodic dipole potential. *Journal of the Optical Society of America B*, 15:1749, 1998.

[55] H. Friedrich, G. Jacoby, and C. G. Meister. Quantum reflection by Casimir-van der Waals potential tails. *Physical Review A*, 65:032902, February 2002.

[56] H. Friedrich and A. Jurisch. Quantum reflection times for attractive tail potentials. *Physical Review Letters*, 92:103202, 2004.

[57] M. E. Gehm. Properties of ^{6}Li. The current version of the document is available at http://www.phy.duke.edu/research/photon/qoptics/techdocs/., 2003.

[58] M. Gehrtz, G. C. Bjorklund, and E. A. Whittaker. Quantum-limited laser frequency-modulation spectroscopy. *Journal of the Optical Society of America B*, 2:1510, 1985.

[59] K. Gibble, S. Chang, and R. Legere. Direct observation of s-wave atomic collisions. *Physical Review Letters*, 75:2666, 1995.

[60] Y. V. Gott, M. S. Ioffe, and V. G. Tel'kovskii. Some new results on confinement in magnetic traps. *Nuclear Fusion Supplement*, 3:1045, 1962.

[61] M. Grenier, C. A. Regal, and D. S. Jin. Probing the excitation spectrum of a fermi gas in the bcs-bec crossover regime. *Physical Review Letters*, 94:070403, 2005.

[62] D. J. Griffiths. *Introduction to Electrodynamics*. Prentice Hall, 2 edition, 1981.

[63] E. P. Gross. Structure of a quantized vortex in a boson system. *Nuovo Cimento*, 20:454, 1961.

[64] T. L. Gustavson, A. P. Chikkatur, A. E. Leanhardt, A. Gorlitz, S. Gupta, D. E. Pritchard, and W. Ketterle. Transport of Bose-Einstein condensates with optical tweezers. *Physical Review Letters*, 88:020401, 2002.

[65] M. H. Hablanian. *High-Vacuum Technology, A Practical Guide*. Marcel Dekker, Inc., 2 edition, 1997.

[66] Z. Hadzibabic. *Studies of quantum degenerate Fermionic lithium gases*. PhD thesis, MIT, 2003.

[67] X. W. Halliwell, H. Friedrich, S. T. Gibson, and K. G. H. Baldwin. Quantum reflection of metastable helium 2^3S atoms in hollow optical fibres. *Optics Communications*, 224:89, 2003.

[68] W. P. Halperin and J. A. Sauls. Helium-three in aerogel. *pre-print*, arXiv:cond-mat/0408593, 2004.

[69] D. M. Harber, J. M. McGuirk, J. M. Obrecht, and E. A. Cornell. Thermally induced losses in ultra-cold atoms magnetically trapped near room-temperature surfaces. *Journal of Low Temperature Physics*, 133:229–238, 2003.

[70] D. M. Harber, J. M. Obrecht, J. M. McGuirk, and E. A. Cornell. Measurement of the Casimir-Polder force through center of mass oscillations of a Bose-Einstein condensate. *Physical Review A*, 72:033610, 2005.

[71] C. Henkel, S. Potting, and M. Wilkens. Loss and heating of particles in small and noisy traps. *Applied Physics B*, 69:379, 1999.

[72] C. Henkel, C. I. Westbrook, and A. Aspect. Quantum reflection: atomic matter-wave optics in an attractive exponential potential. *Journal of the Optical Society of America B*, 13:233, 1996.

[73] T. W. Hijmans, J. T. M. Walraven, and G. V. Shlyapnikov. Influence of the substrate on the low-temperature limit of the sticking probability of hydrogen atoms on He films. *Physical Review B*, 45(5):2561, 1992.

[74] E. A. Hinds and I. G. Hughes. Magnetic atom optics: mirrors, guides, traps, and chips for atoms. *Journal of Physics D*, 32:R119–R146, 1999.

[75] B. Holst and W. Allison. An atom-focusing mirror. *Nature*, 390:244, 1997.

[76] M. Horikoshi and K. Nakagawa. Dephasing due to atom-atom interaction in a waveguide interferometer using a Bose-Einstein condensate. *Physical Reveiw A*, 74:031602(R), 2006.

[77] D. W. Hua, J. Anderson, J. DiGregorio, D. M. Smith, and G. Beaucage. Structural analysis of silica aerogels. *Journal of Non-Crystalline Solids*, 186:142, 1995.

[78] S. Inouye, M. R. Andrews, J. Stenger, H.-J. Miesner, D. M. Stamper-Kurn, and W. Ketterle. Observation of feshbach resonances in a boseeinstein condensate. *Nature*, 392:151, 1998.

[79] J. D. Jackson. *Classical Electrodynamics*. Wiley, 2 edition, 1975.

[80] G. B. Jo, J.-H. Choi, C. A. Christensen, Y. R. Lee, T. A. Pasquini, W. Ketterle, and D. E. Pritchard. Matter-wave interferometry with phase fluctuating Bose-Einstein condensates. *arXiv*, 0706:4041v2, 2007.

[81] G. B. Jo, J.-H. Choi, C. A. Christensen, T. A. Pasquini, Y. R. Lee, W. Ketterle, and D. E. Pritchard. Phase-sensitive recombination of two Bose-Einstein condensates on an atom chip. *Physical Review Letters*, 98:180401, 2007.

[82] G. B. Jo, Y. Shin, S. Will, T. A. Pasquini, M. Saba, W. Ketterle, D. E. Pritchard, M. Vengalattore, and M. Prentiss. Long phase coherence time and number squeezing of two Bose-Einstein condensates on an atom chip. *Physical Review Letters*, 98:030407, 2007.

[83] M. P. A. Jones, C. J. Vale, D. Sahagun, B. V. Hall, and E. A. Hinds. Spin coupling between cold atoms and the thermal fluctuations of a metal surface. *Physical Review Letters*, 91:080401, 2003.

[84] T. E. Judd, R. G. Scott, A. M. Martin, and T. M. Fromhold. Private communication. 2005.

[85] A. Jurisch and H. Friedrich. Realistic model for a quantum reflection trap. *Physics Letters A*, 349:230, 2006.

[86] M. Kasevich, K. Moler, E. Riis, E. Sunderman, D. Weiss, and S. Chu. Applications of laser cooling and trapping. *AIP Conference Proceedings*, 233:47–57, 1991.

[87] M. A. Kasevich, D. S. Weiss, and S. Chu. Normal-incidence reflection of slow atoms from an optical evanescent wave. *Optics Letters*, 15:607, 1990.

[88] W. Ketterle. When atoms behave as waves: Bose-Einstein condensation and the atom laser. *International Journal of Modern Physics B*, 16:4537, 2002.

[89] W. Ketterle, K. B. Davis, M. A. Joffe, A. Martin, and D. E. Pritchard. High densities of cold atoms in a dark spontaneous-force optical trap. *Physical Review Letters*, 70:2253, 1991.

[90] W. Ketterle and N. J. van Druten. Evaporative cooling of trapped atoms. *Advances in Atomic, Molecular and Optical Physics*, 37:181, 1996.

[91] P. Kharchenko, J. F. Babb, and A. Dalgarno. Long-range interactions of sodium atoms. *Physical Review A*, 55:3566, 1997.

[92] P. T. Konkola, C. G. Chen, R. K. Heilmann, C. Joo, J. C. Montoya, C.-H. Chang, and M. L. Schattenburg. Nanometer-level repeatable metrology using the nanoruler. *Journal of Vacuum Science and Technology B*, 21:3097, 2003.

[93] D. Kouznetsov. Private communication. 2004.

[94] D. Kouznetsov and H. Oberst. Reflection of waves from a ridged surface and the Zeno effect. *Optical Review*, 12:363, 2005.

[95] D. Kouznetsov and H. Oberst. Scattering of atomic matter waves from ridged surfaces. *Physical Review A*, 72:013617, 2005.

[96] D. Kouznetsov, H. Oberst, A. Neumann, Y. Kuznetsova, K. Shimizu, J. F. Bisson, K. Ueda, and S. R. J. Brueck. Ridged atomic mirrors and atomic nanoscope. *Journal of Physics B*, 39:1605, 2006.

[97] A. Landragin, J. Y. Courtois, G. Labeyrie, N. Vansteenkiste, C. I. Westbrook, and A. Aspect. Measurement of the van der waals force in an atomic mirror. *Physical Review Letters*, 77:1464, 1996.

[98] A. E. Leanhardt. *Microtraps and waveguides for Bose-Einstein condensates.* PhD thesis, MIT, 2003.

[99] A. E. Leanhardt, T. A. Pasquini, M. Saba, A. Schirotzek, Y. Shin, D. Kielpinski, D. E. Pritchard, and W. Ketterle. Cooling Bose-Einstein condensates below 500 picokelvin. *Science*, 301:1513–1515, September 2003.

[100] A. E. Leanhardt, Y. Shin, A. P. Chikkatur, D. Kielpinski, W. Ketterle, and D. E. Pritchard. Bose-Einstein condensates near a microfabricated surface. *Physical Review Letters*, 90:100404, 2003.

[101] J. E. Lennard-Jones and A. F. Devonshire. The interaction of atoms and molecules with solid surfaces III. the condensation and evaporation of atoms and molecules. *Proceedings of the Royal Society of London. Series A*, 156:6, 1936.

[102] C. Lhuillier and G. Misguich. *High Magnetic Fields: Lecture notes in physics Vol 589*, chapter Frustrated quantum magnets. Springer, 2002.

[103] E. M. Lifshitz. Title unknown. *Soviet Physics- Journal of Experimental and Theoretical Physics*, 3:977, 1957.

[104] Y. Lin, I. Teper, C. Chin, and V. Vuletic. Impact of the Casimir-Polder potential and Johnson noise on Bose-Einstein condensate stability near surfaces. *Physical Review Letters*, 92:050404, 2004.

[105] M. Liu, L. She, H. W. Xiong, and M. S. Zhan. Quantum reflection of vortices in Bose-Einstein condnesates. *Physical Review A*, 74:043619, 2006.

[106] F. London. title unknown. *Z. Phys*, 60:491, 1930.

[107] O. J. Luiten, H. G. C. Werij, I. D. Setija, M. W. Reynolds, T. W. Hijmans, and J. T. M. Walraven. Lyman-alpha spectroscopy of magnetically trapped atomic hydrogen. *Physical Review Letters*, 70:544, 1993.

[108] J. Madronero and H. Friedrich. Influence of realistic atom wall potentials in quantum reflection traps. *Physical Review A*, 75:022902, 2007.

[109] J. Madronero and H. Friedrich. Two-dimensional quantum-reflection traps. *Physical Review A*, 75:062902, 2007.

[110] N. T. Maitra and E. J. Heller. Semiclassical perturbation approach to quantum reflection. *Physical Review A*, 54:4763, 1996.

[111] R. Marani, L. Cognet, V. Savalli, N. Westbrook, C. I. Westbrook, and A. Aspect. Using atomic interference to probe atom-surface interactions. *Physical Review A*, 61:053402, 2000.

[112] M. Marinescu, A. Dalgarno, and J. F. Babb. Retarded long-range potentials for the alkali-metal atoms and a perfectly conducting wall. *Physical Review A*, 55:1530, 1997.

[113] J. M. McGuirk, D. M. Harber, J. M. Obrecht, and E. A. Cornell. Alkali-metal adsorbate polarization on conducting and insulating surfaces probed with Bose-Einstein condensates. *Physical Review A*, 69:062905, 2004.

[114] C. G. Meister and H. Friedrich. Quantum reflection by coupled-channel potentials. *Physical Review A*, 66:042718, 2002.

[115] H. J. Metcalf and P. van der Straten. *Laser cooling and trapping.* Springer, 1999.

[116] M. O. Mewes, M. R.. Andrew, N. J. van Deuten, D. M. Kurn, D. S. Durfee, and W. Ketterle. Bose-Einstein condensation in a tightly confining dc magnetic trap. *Physical Review Letters*, 77:416, 1996.

[117] P. Milloni. *The Quantum Vacuum: An introduction to quantum electrodynamics.* Academic Press, 1994.

[118] P. W. Milonni and M.-L. Shih. Source theory of the Casimir force. *Physical Review A*, 45:4241, 1992.

[119] K. A. Milton. The Casimir effect: recent controversies and progress. *Journal of Physics A*, 37:R209, 2004.

[120] A. Mody, M. Haggerty, J. M. Doyle, and E. J. Heller. No-sticking effect and quantum reflection in ultracold atoms. *Physical Review B*, 64:805418, August 2001.

[121] C. R. Monroe. *Experiments with optically and magnetically trapped cesium atoms.* PhD thesis, University of Colorado, Boulder, 1992.

[122] V. U. Nayak, D. O. Edwards, and N. Masuhara. Scattering of ^{4}He atoms grazing the liquid-^{4}He surface. *Physical Review Letters*, 50:990, 1983.

[123] A. A. Norrie, R. J. Ballagh, and C. W. Gardiner. Quantum turbulence in condensate collisions: An application of the classical field method. *Physical Review Letters*, 94:040401, 2005.

[124] A. A. Norrie, R. J. Ballagh, and C. W. Gardiner. Quantum turbulence and correlations in Bose-Einstein condensate collisions. *Physical Review A*, 73:043617, 2006.

[125] H. Oberst, D. Kouznetsov, K. Shimizu, J. Fujita, and F. Shimizu. Fresnel diffraction mirror for an atomic wave. *Physical Review Letters*, 94:013203, 2005.

[126] H. Oberst, Y. Tashiro, K. Shimizu, and F. Shimizu. Quantum reflection of He* on silicon. *Physical Review A*, 71:052901, 2005.

[127] J. M. Obrecht, R. J. Wild, M. Antezza, L. P. Pitaevskii, S. Stringari, and E. A. Cornell. Measurement of the temperature dependence of the Casimir-Polder force. *Physical Review Letters*, 98:063201, 2007.

[128] J. M. Obrecht, R. J. Wild, and E. A. Cornell. Measuring electric fields from surface contaminants with neutral atoms. *Physical Review A*, 75:062903, 2007.

[129] J. F. O'Hanlon. *A Users Guide to Vacuum Technology.* John Wiley & Sons, 1937.

[130] Y. B. Ovchinnikov, I. Manek, and R. Grimm. Surface trap for Cs atoms based on evanescent wave cooling. *Physical Review Letters*, 79:2225, 1997.

[131] E. D. Palik, editor. *Handbook of Optical Constants of Solids*, volume I,II,III. Academic Press, 1985.

[132] T. A. Pasquini, M. Saba, G. B. Jo, Y. Shin, W. Ketterle, D. E. Pritchard, T. A. Savas, and N. Mulders. Low velocity quantum reflection of Bose-Einstein condensates. *Physical Review Letters*, 97:093201, 2006.

[133] T. A. Pasquini, Y. Shin, C. Sanner, M. Saba, A. Schirotzek, D. E. Pritchard, and W. Ketterle. Quantum reflection from a solid surface at normal incidence. *Physical Review Letters*, 93:223201, 2004.

[134] J. D. Perreault and A. D. Cronin. Observation of atom wave phase shifts induced by van der waals atom-surface interactions. *Physical Review Letters*, 95:133201, 2005.

[135] J. D. Perreault, A. D. Cronin, and T. A. Savas. Using atomic diffraction of na from material gratings to measure atom-surface interactions. *Physical Review A*, 71:053612, 2005.

[136] C. J. Pethick and H. Smith. *Bose-Einstein Condensation in Dilute Gases*. Cambridge Press, 2002.

[137] W. Petrich, M. H. Anderson, J. R. Ensher, and E. A. Cornell. Stable, tightly confining magnetic trap for evaporative cooling of neutral atoms. *Physical Review Letters*, 74:3352, 1995.

[138] L. P. Pitaevskii. Vortex lines in an imperfect bose gas. *Soviet Physics- Journal of Experimental and Theoretical Physics*, 13:451, 1961.

[139] L. P. Pitaevskii. Long-distance behavior of the surface-atom Casimir-Polder forces out of thermal equilibrium. *Journal of Physics A*, 39:6665, 2006.

[140] J. V. Porto and J. M. Parpia. Correlated disorder in a p-wave superfluid. *Physical Review B*, 59:14583, 1999.

[141] D. E. Pritchard. Cooling neutral atoms in a magnetic trap for precision spectroscopy. *Physical Review Letters*, 51:1336, 1983.

[142] E. L. Raab, M. Prentiss, A. Cable, S. Chu, and D. E. Pritchard. Trapping of neutral sodium atoms with radiation pressure. *Physical Review Letters*, 59:2631, 1987.

[143] J. Reichel. Microchip traps and Bose-Einstein condensation. *Applied Physics B*, 75:469, 2002.

[144] J. Reichel, W. Hansel, P. Hommelhoff, and T. W. Hansch. Applications of integrated magnetic microtraps. *Applied Physics B*, 72:81, 2001.

[145] P. K. Rekdal, S. Scheel, P. L. Knight, and E. A. Hinds. Thermal spin flips in atom chips. *Physical Review A*, 70:013811, 2004.

[146] D. Rychtarik, B. Engeser, H. C. Nagerl, and R. Grimm. Two-dimensional Bose-Einstein condensate in an optical surface trap. *Physical Review Letters*, 92:173003, 2004.

[147] C. V. Saba, P. A. Barton, M. G. Boshier, I. G. Hughes, P. Rosenbusch, B. E. Sauer, and E. A. Hinds. Reconstruction of a cold atom cloud by magnetic focusing. *Physical Review Letters*, 82:468, 1999.

[148] M. Saba, T. A. Pasquini, C. Sanner, Y. Shin, W. Ketterle, and D. E. Pritchard. Continuous measurement of the relative phase of two Bose-Einstein condensates using light scattering. *Science*, 307:1945, 2005.

[149] C. A. Sackett. Limits on weak magnetic confinement of neutral atoms. *Physical Review A*, 73:013626, 2006.

[150] J. J. Sakurai. *Modern Quantum Mechanics*. Addison Wesley, revised edition, 1994.

[151] C. Sanner. Momentum interferometry and quantum reflection with Bose-Einstein condensates. Master's thesis, University of Heidelberg, 2004.

[152] T. Savas. *Achromatic interference lithography*. PhD thesis, MIT, 2003.

[153] T. A. Savas, M. L. Schattenburg, J. M. Carter, and H. I. Smith. Large-area achromatic interferometric lithography for 100 nm period gratings and grids. *Journal of Vacuum Science and Technology B*, 14:4167, 1996.

[154] D. W. Schaefer and K. D. Keefer. Structure of random porous materials: Silica aerogel. *Physical Review Letters*, 56:2199, 1986.

[155] M. L. Schattenburg, R. J. Aucoin, and R. C. Fleming. Optically matched trilevel resist process for nanostructure fabrication. *Journal of Vacuum Science and Technology B*, 13:3007, 1995.

[156] M. Scheffler and C. Stampfl. *Handbook of surface science Vol. 2*, chapter Theory of adsorption on metal substrates. North-Holland, 2000.

[157] A. Schirotzek. Fundamental dynamics of Bose-Einstein condensates: Photon recoil and distillation. Master's thesis, University of Hamburg, 2004.

[158] T. Schumm, S. Hofferberth, L. M. Anderson, S. Wildermuth, S. Groth, I. Bar-Joeseph, J. Schmiedmayer, and P. Kruger. Matter-wave interferometry in a double well on a atom chip. *Nature Physics*, 1:57, 2005.

[159] R. G. Scott, D. A. W. Hutchinson, and C. W. Gardiner. Disruption of reflection Bose-Einstein condensates due to interatomic interactions and quantum noise. *Physical Review A*, 74:053605, 2006.

[160] R. G. Scott, A. M. Martin, S. Bujkiewicz, T. M. Fromhold, N Malossi, O. Morsch, M. Cristiani, and E. Arimondo. Transport and disruption of Bose-Einstein condensates in optical lattices. *Physical Review A*, 69:033605, 2004.

[161] R. G. Scott, A. M. Martin, T. M. Fromhold, S. Bujkiewicz, F. W. Sheard, and M. Leadbeater. Creation of solitons and vortices by Bragg reflection of Bose-Einstein condensates in an optical lattice. *Physical Review Letters*, 90(11):110404, 2003.

[162] R. G. Scott, A. M. Martin, T. M. Fromhold, and F. W. Sheard. Anomolous quantum reflection of Bose-Einstein condensates from a silicon surface: The role of dynamical excitations. *Physical Review Letters*, 95:073201, 2005.

[163] B. Segev, R. Cote, and M. G. Raizen. Quantum reflection from an atomic mirror. *Physical Review A*, 56:R3350, 1997.

[164] M. Y. Shen, C. H. Crouch, J. E. Carey, and E. Mazur. Femtosecond laser-laser induced formation of submicrometer spikes on silicon in water. *Applied Physics Letters*, 85:5694, 2004.

[165] F. Shimizu. Specular reflection of very slow metastable neon atoms from a solid surface. *Physical Review Letters*, 86:987–990, 2001.

[166] F. Shimizu and J. Fujita. Giant quantum reflection of neon atms from a ridged silicon surface. *Journal of the Physical Society of Japan*, 71:5, 2002.

[167] F. Shimizu and J. Fujita. Reflection-type hologram for atoms. *Physical Review Letters*, 88:123201, 2002.

[168] Y. Shin, G.-B. Jo, M. Saba, T. A. Pasquini, W. Ketterle, and D. E. Pritchard. Optical weak link between two spatially separated Bose-Einstein condensates. *Physical Review Letters*, 95:170402, 2005.

[169] Y. Shin, M. Saba, T. A. Pasquini, W. Ketterle, D. E. Pritchard, and A. E. Leanhardt. Atom interferometry with Bose-Einstein condensates in a double-well potential. *Physical Review Letters*, 92:050405, 2004.

[170] Y. Shin, M. Saba, A. Schirotzek, T. A. Pasquini, A. E. Leanhardt, D. E. Pritchard, and W. Ketterle. Distillation of Bose-Einstein condensates in a double-well potential. *Physical Review Letters*, 92:150401, 2004.

[171] Y. Shin, C. Sanner, G.-B. Jo, T. A. Pasquini, M. Saba, W. Ketterle, D. E. Pritchard, M. Vengalattore, and M. Prentiss. Interference of Bose-Einstein condensates on an atom chip. *Physical Review A*, 72:021604(R), 2005.

[172] Y. I. Shin. *Experiments with Bose-Einstein condensates in a double-well potential.* PhD thesis, MIT, 2006.

[173] H. I. Smith, S. D. Hector, M. L. Schattenburg, and E. H. Anderson. A new approach to high fidelity e-beam and ion-beam lithography based on an in situ global-fiducial grid. *Journal of Vacuum Science and Technology B*, 9:2992, 1991.

[174] L. Spruch. Retarded, or Casimir, long-range potentials. *Physics Today*, page 37, November 1986.

[175] L. Spruch and Y. Tikochinsky. Elementary approximate derivations of some retarded Casimir interactions involving one or two dielectric walls. *Physical Review A*, 48:4213, 1993.

[176] D. M. Stamper-Kurn. *Peeking and poking at a new quantum fluid: Studies of gaseous Bose-Einstein condensates in magnetic and optical traps.* PhD thesis, MIT, 2000.

[177] C. A. Stan. *Experiments wtih interacting Bose and Fermi gases.* PhD thesis, MIT, 2005.

[178] C. A. Stan and W. Ketterle. Multiple species atom source for laser-cooling experiments. *Review of Scientific Instruments*, 76:063113, 2005.

[179] C. A. Stan, M. W. Zwierlein, C. H. Schunck, S. M. F. Raupach, and W. Ketterle. Observation of feshbach resonances between two different atomic species. *Physical Review Letters*, 93:143001, 2004.

[180] D. A. Steck. Sodium d line data. The current version of the document is available at `http://steck.us/alkalidata.`, 2003.

[181] E. W. Streed. *Rubidium Bose-Einstein condensates: Machine construction and quantum Zeno experiments.* PhD thesis, MIT, 2005.

[182] E. W. Streed, A. P. Chikkatur, T. L. Gustavson, M. Boyd, Y. Torii, D. Schneble, G. K. Campbell, D. E. Pritchard, and W. Ketterle. Large atom number Bose-Einstein condensate machines. *Review of Scientific Instruments*, 77:023106, 2006.

[183] A. Vogel, M. Schmidt, K. Sengstock, K. Bongs, W. Lewoczko, T. Schuldt, A. Peters, T. Van Zoest, W. Ertmer, E. Rasel, T. Steinmetz, J. Reichel, T. Konemann,

W. Brinkmann, E. Goklu, C. Lammerzahl, H. J. Dittus, G. Nandi, W. P. Schleich, and R. Walser. Bose-Einstein condensates in microgravity. *Applied Physics B*, 84:663, 2006.

[184] A. Yu. Voronin, P. Froelich, and B. Zygelman. Interaction of ultracold hydrogen with a conducting wall. *Physical Review A*, 72:062903, 2005.

[185] M. Walsh. *On the design of lithographic interferometers and thier application*. PhD thesis, MIT, 2004.

[186] Y. J. Wang, D. Z. Anderson, V. M. Bright, E. A. Cornell, Q. Diot, T. Kishimoto, M. Prentiss, R. A. Saravanan, S. R. Segal, and S. Wu. Atom Michelson interferometer on a chip using a Bose-Einstein condensate. *Physical Review Letters*, 94:090405, 2005.

[187] NGDC Website. Compute earth's magnetic field values, 2007. http://www.ngdc.noaa.gov/seg/geomag/magfield.shtml.

[188] G. Weightman. *The Frozen-Water Trade: A True Story*. Hyperion, 2003.

[189] S. Will. Atom optical experiments with ultracold sodium atoms. Master's thesis, University of Mainz, Germany, 2006.

[190] W. H. Wing. On neutral particle trapping in quasistatic electromagnetic fields. *Progress in Quantum Electronics*, 8:181, 1984.

[191] A. F. G. Wyatt, M. A. H. Tucker, and R. F. Cregan. Reflectivity of ^{4}He atoms from liquid ^{4}He: Direct observation of the effect of phonons and rotons. *Physical Review Letters*, 74:5236, 1995.

[192] ZongChao Yan, A. Dalgarno, and J. F. Babb. Long-range interactions of lithium atoms. *Physical Review A*, 55:2882, 1997.

[193] I. A. Yu, J. M. Doyle, J. C. Sandberg, C. L. Cesar, D. Kleppner, and T. J. Greytak. Evidence for universal quantum reflection of hydrogen from liquid ^{4}He. *Physical Review Letters*, 71:1589, 1993.

[194] P. Zarth. *Magneto optical trapping of potassium 40*. PhD thesis, Universitat Karlsruhe (TH), 2006.

[195] M. W. Zwierlein. *High-temperature superfluidity in an ultracold Fermi gas*. PhD thesis, MIT, 2006.

[196] M. W. Zwierlein, C. H. Schunck, A. Schirotzek, and W. Ketterle. Direct observation of the superfluid phase transition in ultracold Fermi gases. *Nature*, 54:442, 2006.